A Domain Decomposition Technique for Generation and Scattering of Acoustic Waves

Lim Wei Xian

School of Mechanical & Aerospace Engineering

A thesis submitted to the Nanyang Technological University
in partial fulfillment of the requirements for the degree of
Doctor of Philosophy

2023

Statement of Originality

I hereby certify that the work embodied in this thesis is the result of original research, is free of plagiarised materials, and has not been submitted for a higher degree to any other University or Institution.

24 Jan 2023

Date

Lim Wei Xian

Supervisor Declaration Statement

I have reviewed the content and presentation style of this thesis and declare it is free of plagiarism and of sufficient grammatical clarity to be examined. To the best of my knowledge, the research and writing are those of the candidate except as acknowledged in the Author Attribution Statement. I confirm that the investigations were conducted in accord with the ethics policies and integrity standards of Nanyang Technological University and that the research data are presented honestly and without prejudice.

24 Jan 2023

.....

Date

.....

Asst. Prof. Chan Wai Lee

Authorship Attribution Statement

This thesis does not contain any materials from papers published in peer-reviewed journals or from papers accepted at conferences in which I am listed as an author.

24 Jan 2023

.....

Date

.....

Lim Wei Xian

Acknowledgements

The computational work for this dissertation was performed on resources of the High-Performance Computing Center, NTU, Singapore, and National Supercomputing Centre, Singapore (https://www.nscc.sg).

The Rijke tube experiments in this thesis were supported by the National Research Foundation, Prime Minister's Office, Singapore under its NRF-NSFC joint grant (NRF2016NRF-NSFC001-102). Any opinions, findings, and conclusions or recommendations expressed in this materials are those of the authors and do not reflect the views of National Research Foundation, Singapore.

I wish to express my greatest gratitude to Nanyang Technological University, Singapore in providing me NTU Research Scholarship throughout my Ph.D study. Also, I would especially like to thank my advisor and co-advisor, Asst. Prof. Wai Lee Chan, and Assoc. Prof. Basman Elhadidi, respectively, for their guidance, for inspiriting me in way of critical thinking, science and life values. Also, I appreciate my thesis advisory committee members, Assoc. Prof. Fei Duan and Prof. Ephraim Gutmark for giving insightful comments throughout my research path.

This dissertation cannot be done without the helps from my colleagues and friends, they are Dr. Vevek, Hanlin, Dhana, Chong, and Jia Min. Last but not least, I want to express my love to my family especially my parents who keep supporting, encouraging and counseling me when I faced challenges and felt dispirited.

Abstract

In this dissertation, a 2D domain decomposition technique (DDT) is developed based on an overset method coupling a nonlinear solver with a linearized Euler solver. The nonlinear solver can account for complex physics such as turbulence, combustion, and thermoacoustics, whereas the linear domain is based on a low dispersion and dissipation scheme to convect waves accurately. Multiple problems are investigated in this thesis, namely acoustic wave generation and scattering in internal and external flows, convection driven thermal plume, isothermal turbulent jet flow, and thermoacoustic instabilities induced by heater and chemical reacting flow. First, extension of DDT to 2D was validated with 1D published results and theoretical solutions. For 2D inviscid flow cases, the internal and external flow simulations, converging-diverging nozzle in subsonic and supersonic flow regimes and transonic flow over supercritical airfoil were conducted, respectively. Simulation results have demonstrated that higher overlap ratio between linear and nonlinear regions is encouraged to propagate the acoustic waves with less dissipation and dispersion errors. Moreover, substantial cost-savings of 84% and 51% were observed when DDT was used for converging-diverging nozzle simulations in subsonic and supersonic flow regimes, respectively. Additionally, implementation of DDT in external flow simulation has eliminated the unsteady perturbation observed in fully nonlinear far-field region and allows proper wave scattering, interference, and Doppler effect to be observed. For 2D viscous flow, a thermal plume under convective flow condition was simulated as a canonical study of thermoacoustic problem. Results demonstrate the feasibility of DDT in capturing not only the frequency of vortex shedding, but also the heat release rate fluctuation, while reducing approximately 13% of computational hours as compared to fully nonlinear simulations. Hence, more complex thermoacoustic DDT simulations are possible. DDT was then extended into 3D to get high-fidelity acoustic generation results for an isothermal turbulent jet case. Preliminary results for the 3D case demonstrate cost-saving of 16% however technical challenges remain unsolved.

Extension of complex nonlinear simulation to include thermoacoustic for chemically reaching flows was performed for a Rijke tube test case. The thermoacoustic instability was assessed by evaluating the standard and extended Rayleigh criteria. In this thesis, only the nonlinear domain was considered as extension to DDT will be addressed in future work. Numerical results show that both chemically non-reacting and reacting simulations compare well with theoretical models and qualitatively with experimental measurements, respectively. Both assessment criteria are correctly indicating the state of thermoacoustic instability in all Rijke tube simulations. The nonlinear solver, therefore, is capable for high-fidelity acoustic generation via thermoacoustic means.

Contents

List of Figures

List of Tables

Nomenclature

Symbols

ϵ	Small amplitude or strength
ρ	Density [kgm^{-3}]
γ	Heat capacity ratio
ϕ	Field values or equivalence ratio
κ	Thermal conductivity of fluid [W(mK)$^{-1}$]
λ	Wavelength
μ	Dynamic viscosity
A	Total surface area of cell [m^2]
C	Progress variable
C_L	Lift coefficient
C_p	Pressure coefficient
c	Speed of sound [ms^{-1}]
D	Diameter [m]
e	Acoustic energy per unit volume [Jm^{-3}]
E	Acoustic energy [J]
F	Acoustic flux/loss [W]
f	Frequency [Hz]
J	Vector of viscous diffusion terms
k	Wave number
L	Characteristic length [m]
Ma	Mach number
m	Mass [kg]
p	Pressure [Pa]
$\mathbf{Q}$	Vector of conserved variables
$\dot{Q}$	Total heat release rate [W]

$\dot{q}$	Specific heat release rate [Wm^{-3}]
R	Overlap ratio
Re	Reynolds number
S	Acoustic source/sink [W]
$\mathbf{S}$	Surface area vector [m^2]
Sc	Schmidt number
t	Time [s]
T	Temperature [K]
$\mathbf{U}$	Velocity vector [ms^{-1}]
w	Weightage
Y	Mass fraction of a species
Z	Mixture fraction
Z''^2	Mixture fraction variance

Superscripts and Subscripts

$()'$	Fluctuation
$\overline{()}$	Time average
$\hat{()}$	Modal complex decomposition
$\widetilde{()}$	Filtered
$()_z$	Axial component
$()_{etd}$	Extended Rayleigh criterion
$()_{std}$	Standard Rayleigh criterion
$()_{\mathrm{L}}$	With respect to linear region/cell
$()_{\mathrm{NL}}$	With respect to nonlinear region/cell
$()_\infty$	Freestream

Chapter 1

Introduction

1.1 Background

The study of acoustic scattering and interaction of waves with solid boundaries remains of great interests to the research community, largely because of the multitude of relevant problems. The scattering of acoustic waves is an important consideration in the design of new generation aircrafts, which are subject to stringently low noise limits. For instance, inside an aircraft, the acoustic waves are primarily generated by jet engine via various means [1], as shown in Figure 1.1. These acoustic waves will be scattered by the engine geometry and components such as rotor and stator blades. When the acoustic waves propagate downstream and interact inside the engine hot section, it may couple with combustion and induce instabilities with high amplitude resonance frequency [2], which may damage the engine structure in the worst case [3]. Near the exhaust section, the existence of shock will further amplify the acoustic waves [4]. Radiated acoustic wave from jet engine will scatter over the wing, alluding the airframe noise due to the interaction between wing and acoustic waves.

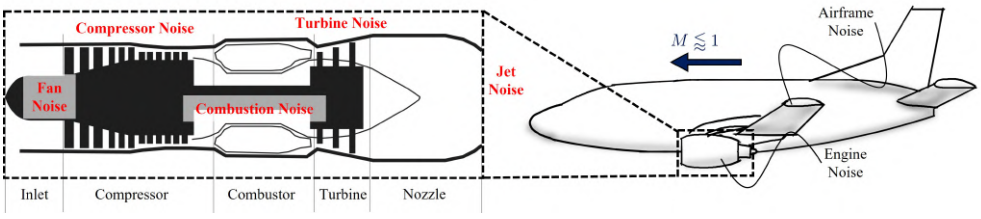

FIGURE 1.1: Types of jet engine noise

It is vital to identify and understand the outcomes of the acoustic scattering and interaction with environment to prevent any failure to the engine/aircraft. Thus, the evaluation of acoustic source and accurately propagating the sound to the far-field requires accurate and efficient numerical models that can handle the large difference in length scales and high frequency of wave propagations, which will lead to spatial and temporal scale separation from the flow dynamics. These scale disparities will generally require high grid and temporal resolutions that will deem any practical simulations intractable.

In addition, the non-linearity phenomena, such as the unsteady combustion, shock wave, and jet vortices found in jet engines, require nonlinear equations to be solved, for which there is always numerical diffusion. In computational aeroacoustics, an inviscid linear solver is usually considered since the acoustic propagation can be modelled as small perturbations over a mean state and the viscous effects are negligible. However, by design, the linear solver is unable to capture the nonlinear phenomena that generate the waves. Hence, to obtain the best features of both linear and nonlinear solvers, domain decomposition technique (DDT) [5, 6] was applied in this work to couple the nonlinear and linear solvers.

To conduct DDT simulation, the computational domain is segregated into two regions, linear and nonlinear domains. The nonlinear domain can contain complex geometry, unstructured mesh, and nonlinear flow features, which can be solved by nonlinear equations, such as Euler or Navier Stokes equations. Inside the linear domain, linearized versions of nonlinear equations are solved on uniform grids to transport any small perturbations, which include pressure, velocity and density perturbations. These small perturbations can either be generated from the nonlinear domain or artificially introduced into the linear domain. For instance, to simulate combustion noise generation from a combustion chamber using DDT, the geometry of the combustor must be constructed in the nonlinear domain so that non-linearity features such as combustion, turbulence, and instability can be described with nonlinear governing equations. Thereafter, the interface between linear and nonlinear domains must be far enough from aerodynamically active area where the background mean fields are steady or quasi-steady. The linear domain then transports the small perturbations coming from the combustion chamber into the far-field with minimum dissipation and dispersion. With that, DDT is able to bypass the excessive resources required for nonlinear solver in long distance wave

propagation and capture nonlinear wave generation and scattering events for which the linear solver is incapable.

In this thesis, the focus is given to extend the usage of DDT into higher spatial dimensions to incorporate high-fidelity nonlinear solver for the prediction of acoustic generation, propagation and scattering. Validation was done to ensure proper extension into two-dimensional space and higher. 2D applications were simulated to systematically study the acoustic interactions: (i) with different flow regimes, (ii) with solid body, such as scattering over an airfoil (or turbine blade), and (iii) with non-isothermal viscous flow by thermal plume. DDT in 3D application was attempted by solving an isothermal turbulent jet problem using high-fidelity large-eddy simulation (LES) to investigate the jet noise generation and propagation. To confirm LES can accurately predict the acoustic generation and interactions, the Rijke tube, a canonical thermoacoustic configuration, was chosen with different types of heat sources. This configuration is known to be able to induce thermoacoustic instability by design and generate acoustic wave at a specific resonance tone characterized by the tube length. To emulate the combustor scenario, where the instability and noise stem from combustion, one of the heating source is a chemically reacting flow simulated by integrating combustion models into LES solver. Furthermore, to evaluate and confirm the existence of instabilities in numerical results, Rayleigh criteria [7, 8] were assessed.

Overall, the developed solver in this work is based on the OpenFOAM-v1912 framework, an open-source CFD package [9], which has good extensibility quality. OpenFOAM users are able to develop their own boundary conditions, turbulence models, and even build their own solvers. Besides, there are a wide range of applications and models that are readily accessible. For post-processing, a set of algorithms to provide quantitative results from both experimental and simulation data were developed in this work. These algorithms are general and will facilitate any future studies that are relevant to acoustics.

1.2 Objective and Scopes

The main objective of this research is to contribute to the fundamental understanding of aeroacoustic and facilitate the knowledge transfer to practical applications,

especially for the development of next generation quiet aircrafts. To achieve this, a high-fidelity numerical method is developed for the prediction of acoustic and noise generations as well as the far-field wave propagation and scattering. The scopes of this work are listed below:

- Developing domain decomposition technique (DDT) for wave scattering and propagation under finite volume framework.
- Validating DDT for 2D extension.
- Applying DDT for 2D and 3D applications
- Coupling the combustion models with the nonlinear large-eddy simulation flow solver.
- Evaluating the thermoacoustic instabilities with Rayleigh's criteria.

1.3 List of Accomplishments

Important contributions and insights are compiled in following list:

- Developed a domain decomposition technique for 2D and 3D simulations, identifying limitations and their possible rectifications in future work.
- Validated applicability of large-eddy simulation technique to capture acoustic generation through several canonical 3D configurations, such as turbulent jet and Rijke tube.
- Extended non-reacting OpenFOAM solver capabilities to capture compressible turbulent reacting flows by coupling the solver with combustion models.
- Developed post-processing algorithms to analyze numerical acoustic results and calculate the aerodynamic/thermodynamic characteristics of flows.
- Prepared and submitted two manuscripts.
- Presented at 72^{nd} Annual Meeting of the APS Division of Fluid Dynamics.
- Contributed to the successful completion of two funded research projects on combustion noise and instability.

1.4 Thesis Outline

The thesis is organized as follows:

- Chapter 1 describes the background and objective of the research and the scopes to achieve the aim. Highlights of the work are presented as well.
- Chapter 2 reviews the past relevant studies.
- Chapter 3 presents the DDT in terms of the coupling method, governing equation, setup, and a briefly discussion about the thermoacoustic nonlinear solver.
- Chapter 4 demonstrates the 2D DDT applications in terms of inviscid internal and external flows and non-isothermal viscous flow cases.
- Chapter 5 discusses the preliminary study of 3D DDT extension for an isothermal turbulent jet simulation and thermoacoustic instability simulations of different heat sources.
- Chapter 6 draws a conclusion for the research works and provides suggestions for the future work.

Chapter 2

Literature Reviews

2.1 Aeroacoustics

Acoustics studies the generation, propagation, and interaction of small perturbations, which are mechanical waves due to the oscillation of the particles of a medium. Many analogies have been proposed in the early days to study acoustic wave behaviors, especially those associated with aerodynamics, also known as aeroacoustics. For example, Lighthill's analogy [10] on flow-generated sound has introduced the most influential concept of representing acoustics as perturbations to a reference flow, typically the mean and/or quasi-steady state of the flow field. Small perturbation is always assumed as unsteady velocity and pressure fields, which are usually several order less than their corresponding reference states. With that, Lighthill applied his work on aerodynamic noise generated by a turbulent flow in both subsonic and supersonic regimes [11]. Powell's analogy [12] explains the creation of aerodynamic noise due to the vortex movement of a turbulent jet, which was used to predict the vortex-pairing sound [13]. Besides, Ffowcs Williams-Hawkings analogy [14, 15] extends Lightill's acoustic analogy by taking into account of moving surfaces immersed in the flow field. Other theoretical analyses [16–20] have been done in studying wide ranges of aero-system related noise generations, such as propeller noise, turbomachinery noise, jet noise, and combustion noise.

In the experimental front, various methods [21] have been adopted to study the jet noise generation, such as two-point statistics [22, 23], and near-field pressure

measurements [24–26]. Effort was given for the experimental work on the collection of acoustic data originating from high-lift wing configuration [27] and landing gear system [28] to provide an extensive database for numerical validation. Measurement was also done on three-element high-lift airfoil [29] and the region between slot cove and main element has been found to be the main aerodynamic noise source. Moreover, the acoustic experimental study has been extended to moving objects scenario such as unmanned aerial vehicle [30, 31] for investigating the aeroacoustic characteristics of small propellers.

2.2 Thermoacoustics

Thermoacoustics generally studies the relationship between acoustics and thermodynamics property of a fluid. The interactions of acoustic with reacting flow can be one-way, where noise is produced but does not affect the flow [32] or two-way, where the acoustic feedback can lead to flow instabilities [33]. The first recorded observation of combustion driven sound was in 1802 by Higgins [34], who found that by placing a hydrogen diffusion flame inside a tub would lead to a "singing flame" phenomenon. Half a century later, Rijke found that sound can be generated by using a heater as well [7, 34]. In his experiments, Rijke observed acoustic oscillations when a heated wire gauze is placed in the lower half of an open-ended tube, but not when the gauze is placed in the upper half of the same tube.

Rayleigh proposed a criterion for these observations of the heat-driven oscillations [7], which assorts that acoustic oscillations are generated when heat is added during the maximum pressure cycle and extracted during the minimum pressure cycle, regardless of the types of heat source. This is akin to the phenomenon of resonance, which will result in the amplification of the acoustic oscillations. Similarly, oscillations can be amplified by heat extraction at the rarefaction or low temperature phase. Recently, a more comprehensive and extended version of Rayleigh's criterion was proposed [8] to account the acoustic energy loss. Another theoretically study was done by Kirchhoff [35] on sound propagation inside an isothermal duct, for which he had constructed a mathematical model to calculate acoustic attenuation due to oscillation of heat transfer inside the duct. The model was then utilized by Karmers [36] to study the gas vibration inside a duct. Thereafter, Rott [37]

proposed a linear thermoacoustic theory based on Kirchhoff and Karmers works [35, 36] to study the thermoacoustic instability that built up inside a tube.

Apart from the theoretical studies on thermoacoustic engines [38, 39] and refrigerators [40, 41], the research on thermoacoustic instabilities inside the jet engines is gaining attention from the acoustic community. This is because the combustion process can generates noises and instabilities [42], which occurs when coupling between heat release rate fluctuations and pressure perturbations takes place. If this instability creates discrete tones at the resonant frequencies of the combustor, along with the high-level broadband combustion noises, structural damages to engine components [43–45] become possible. Hence, the experimental measurement on gas turbine combustor [2] was done to investigate the mechanism of instabilities, which was found to relate to the periodic fluctuation of equivalence ratio and delay of fuel transport to flame zone. Furthermore, the experiment work by Zhu [46] found that the combustion dynamics in a partially premixed swirl combustor is made up of three regimes, namely small scale of combustion noise, intermittent oscillation with multiple frequencies and limit cycle oscillation at strong distinct frequency.

2.3 Computational Acoustics

The numerical approach has become more reliable and feasible due to the remarkable advancement in computational power. Study of thermoacoustics is therefore no longer limited to theoretical or experimental approaches. A 2D Rijke tube configuration was modelled numerically using computational fluid dynamics (CFD) method [47] and illustrates the coupling between the heat addition into fluid with velocity and pressure oscillations. Similar Rijke tube configuration was used in reference [48] to investigate not only the self-exited thermoacoustic instability, but also the non-linearity when heat is transferred from the heater into the ambient fluid, which defines the resonance amplitude. Other numerical works [46, 49, 50] also have been done to predict the frequency of onset instability inside either a Rijke tube or combustion chamber. Numerical prediction of the combustion instability needs to consider the detailed chemistry mechanisms, the combustor geometry, unsteady and compressible flow, which require with high-fidelity numerical methods [51].

In acoustics, its numerical approach is known as computational aeroacoustics (CAA), which solves acoustic problem associated with aerodynamics phenomena numerically. In general, aerodynamic sound can be created by two mechanisms [52]: (i) turbulence and (ii) moving surfaces or surface immersed in a nonuniform flow. For the latter mechanism, the noise radiates predominantly from the moving part of a rotating system, which causes a displacement effect that introduces pressure fluctuation. Propeller and wind turbine are typical example for such systems [53–57], and their noise is impulsive and has deterministic tones. Aerodynamic noise generated by turbulence, however, has a broad frequency spectrum due to its randomness. The common example is the jet noise, where sound is radiated from the jet shear layer with high rate of change of momentum flux [11]. Numerical requirements are high for resolving the turbulent features by direct numerical simulation (DNS) or LES with proper turbulent models.

Moreover, the multiscale nature in aeroacoustic field also makes the numerical approach difficult. Because of the spatial and temporal scale disparities [58] between the aerodynamic and acoustic fluctuations, different requirements are necessary, which neither CFD nor CAA schemes are able to satisfy all of them, especially for low Mach number flow. For instance, away from the effective aerodynamic area, a linear solver, such as linearized Euler Equation (LEE) is sufficient to describe the acoustic perturbations. Dispersion-relation preserving (DRP) scheme [59] is one of the popular CAA schemes which works outstandingly on uniform Cartesian grids with smooth and continuous mean flows. However, DRP fails when the mean flow comprises of high gradient and discontinuities [60], which are often observed in the aerodynamic active area. This highly nonlinear region requires a nonlinear formulation, such as Navier-Stokes (NS) equation, which can be provided by the CFD. Due to the inherent dispersion and dissipation errors in CFD [61, 62], enormous computational resources are needed to simulate acoustic propagation over a long distance. A hybrid method [63] to couple CFD and CAA numerical techniques has then been developed to conquer this scale disparity.

The coupling method proposed by Manoha et al. [63] in general consists of three steps: (i) In the near field, a compressible 2D LES simulation is employed to solve for the local unsteady aerodynamic. (ii) At the boundary of LES simulation domain, the perturbations are transferred to the intermediate domain (one-way trip), where LEE is computed. (iii) In the far field, Kirchhoff integration is utilized to

solve noise radiation with the perturbation data from the intermediate domain. The data injection from LES to LEE was reported to require a high-order interpolation [64] and overlapping grid [65] to obtain correct acoustic propagation. Other studies [66–68] have similarly coupled the flow and acoustic physics in one way by coupling surface between non-overlapping domains that solves Navier-Stokes and nonlinear Euler equations. Similar non-overlapping domain with two-way CFD-CAA coupling method by Langenais et al. [69, 70] has utilized discontinuous Galerkin method [71] for realistic space application.

The domain decomposition technique [5], another type of coupling method, is used to couple the nonlinear and linear solvers in a finite volume framework with the overset mesh technique. Previous related work [6] has shown the feasibility to couple Euler equation and its linear counterpart in an one-dimensional study of the interaction between shock wave and acoustic wave. The work also concluded that the total computational time required by domain decomposition solver was reduced by factor of three compared with a fully nonlinear solver while maintaining the accuracy.

2.4 Research Gap and Summary

Excessive numerical diffusion always happens in nonlinear solvers while the linear solvers are unable to compute nonlinear phenomena correctly. Thus, several hybrid methods were introduced to couple both nonlinear and linear solvers. Table 2.1 shows the pros and cons of various types of hybrid methods, including the DDT method. The advantage of the hybrid methods by [63, 64, 66–68] is the extra coupling with the integral method, which allows for homogeneous far-field wave propagation. However, these hybrid methods are merely coupled in one-way and so are limited to weakly couple problems, where the acoustic pertubations in CAA and integral method have negligible effects on the CFD solution, for instance jet noise. These hybrid methods also reported on the necessity of having sufficient overlaps of the two domains to obtain the correct acoustic propagation.

The two-way non-overlapping CFD-CAA coupling method by Langenais et al. [69, 70] has its biggest advantage in using irregular grids in CAA scheme, but

TABLE 2.1: Comparison of various hybrid methods with DDT.

Hybrid method	Pros	Cons
[63, 64, 66–68]	• Extra integral method	• One-way coupling • Non-overlapping grid
[69, 70]	• Two-way coupling • Unstructured grid is allowed in CAA	• Overestimated noise • Non-overlapping grid
DDT [5]	• Two-way coupling • Overset method • Cost-saving [6]	• Uniform grid is required in CAA

the simulation tends to overpredict the noise generation. DDT [5] is also a two-way coupling method between CFD and CAA, but achieves the coupling through overset grids. Its ability to reduce computational cost has been demonstrated in 1D simulations [6] currently restricted to steady mean problems, similar to other hybrid methods.

In this thesis, DDT is extended from the basis of Reference [5, 6] into higher dimensional spaces for studying acoustic/noise generation, propagation and scattering to the far-field region. Moreover, to obtain high-fidelity acoustic generation solution by thermoacoustic means, the capability of LES solver integrated with combustion models was examined with a comprehensive study of the Rayleigh criterion.

Chapter 3

Domain Decomposition Setup

In this thesis, OpenFOAM-v1912 [9] is primarily used due to the flexibility of accessing its source codes and extensive range of functionalities to solve many complex fluid problems, including heat transfer, turbulence, and chemical reaction, using finite volume method (FVM) [72].

3.1 Domain Decomposition Technique

Domain decomposition technique (DDT) couples two different solvers that can account for dissimilar physical characteristics. For example, the inner domain can model turbulent combustion, whereas the outer domain is a linearized Euler that is used primarily to propagate acoustic waves. In this work, the technique is implemented in a finite volume framework with an overset method to two-way couple a linear outer solver for acoustic wave propagation and a nonlinear inner solver to account for complex multiphysics. Figure 3.1 illustrates the general setup with the computational domain divided into the linear and nonlinear regions together with a sponge zone to absorb the outgoing wave. The nonlinear region can contain complex geometry, along with nonlinear flow features such as shock waves. In the far-field region where the flow has a steady mean state, linear solver can be applied with uniform Cartesian mesh. The source of the acoustics either comes from the linear region (periodic or point source input) or nonlinear region (jet noise or thermoacoustic source).

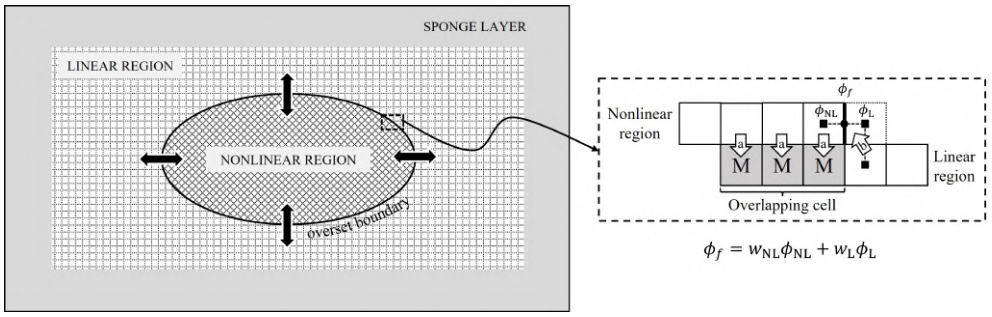

FIGURE 3.1: Schematic drawing of the computational domain with domain decomposition technique. Information are shared at overset boundary between the two regions via (a) mapping from nonlinear to linear and (b) interpolation of the interface values.

The acoustic wave propagation is governed by linearized Euler or NS equations (LEE or LNS). The dispersion relation preserving (DRP) scheme [59, 73] and low-dissipation and low-dispersion Runge-Kutta (LDDRK) scheme [74] are applied for spatial and temporal discretization, separately, to maintain accurate wave propagation over long domains. The transfer of information between the regions is operated within the overset framework, as illustrated in a close-up view of the schematic. In the inset, the arrows (a) delineate the mapping from nonlinear cells to linear cells, whereas the arrow (b) represents the overset interface interpolation. The number of mapped cells, labeled as 'M', is determined by the DRP scheme order implemented in linear region. For instance, a symmetric six-cell stencil of DRP scheme needs at least three cells from linear region at the overset boundary in each coordinate direction to be mapped. Note that, the mapped cells from the linear region lie completely inside the nonlinear region. To account for higher dimension simulations and complex geometry, a generic mapping method that employs cell volume as the weights for mapping process is utilized. For interpolation process (arrow (b)), the overset interface value, ϕ_f, is either interpolated linearly or using higher order interpolation from both regions, depending on the need. In this work, only linear interpolation is considered.

There are two methods in constructing DDT simulation from fully nonlinear results, as presented in Figure 3.2. Procedure (**a**) is a generic way of constructing DDT simulation that can account for unsteady means, in the fully nonlinear results like turbulent flow feature or generation of acoustic waves. It requires the fully nonlinear simulation to collect the statistical mean fields before interpolating into the DDT simulation domain. Procedure (**b**), on the other hand, is considered when

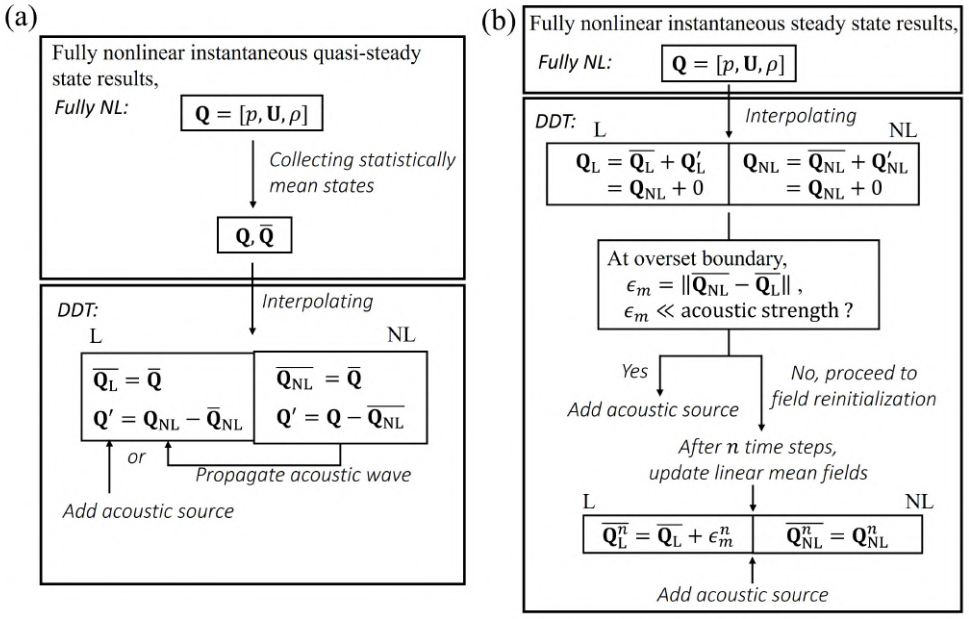

FIGURE 3.2: Two types of procedures of the DDT simulation were used for different cases. 'L', 'NL', '*DDT*' and '*Fully NL*' denote the linear and nonlinear regions, DDT and fully nonlinear simulations, respectively.

the instantaneous fields are approximately equal to their steady mean fields or the order of the mapping error is comparable to the order of acoustic magnitude. Instantaneous fully-nonlinear simulation results from a (quasi-)steady state are used to initialize mean fields, $\overline{\mathbf{Q}}$, of both regions. An interpolation error, ϵ_m, due to the interpolation and injection of variables will be generated at the overset boundary where the linear and nonlinear fields overlap. If the error is comparable to the acoustic wave amplitude, a field reinitialization step is preferred to ensure that the fields of both regions at the overset boundary are similar. The reinitialization advances a few time steps and then updates the linear mean fields, $\overline{\mathbf{Q}_L}$, with the new error, ϵ_m^n, caused by the mismatch of the mean fields at the overset boundary. Thereafter, the perturbation fields, $\overline{\mathbf{Q}'_\mathrm{L}}$, are reinitialized before the acoustic source is introduced. In this work, procedure (**b**) was used in the 2D DDT simulations in Chapter 4. For 3D DDT simulation in Chapter 5, procedure (**a**) was chosen.

3.1.1 Governing Equations and Coupling

For the nonlinear inner domain, where complex flow features are expected, nonlinear flow equations are essentially required to be solved. Hence, Navier Stokes equations (NS), the partial differential equations that govern viscous fluid motions,

are considered. For compressible flows, the conservative form of NS can be defined as follows,

$$\partial_t \mathbf{Q} + \nabla \cdot \mathrm{F}(\mathbf{Q}) - \mathrm{G}(\mathbf{Q}) = 0 \,, \tag{3.1}$$

where $\mathbf{Q} = (\rho, \rho\mathbf{U}, \rho e_t)^{\mathrm{T}}$ represents the vector of conserved variables of continuity, momentum and energy equations. e_t is the specific total energy term consisting of specific internal energy, e and kinetic energy, $k = 0.5\rho||\mathbf{U}||^2$. With ideal gas assumption, the flux vector $\mathrm{F}(\mathbf{Q})$ is described as,

$$\mathrm{F}(\mathbf{Q}) = \begin{pmatrix} \rho\mathbf{U} \\ \rho\mathbf{U}\mathbf{U} + p\mathbf{I} \\ \frac{\gamma p\mathbf{U}}{\gamma - 1} + \frac{1}{2}\rho||\mathbf{U}||^2\mathbf{U} \end{pmatrix} \,, \tag{3.2}$$

where γ is the specific heat ratio, $\gamma = 1.4$ for air, and $\mathbf{I}$ is Kronecker delta tensor. The viscous and external source function $\mathrm{G}(\mathbf{Q})$ is defined as follows,

$$\mathrm{G}(\mathbf{Q}) = \begin{pmatrix} 0 \\ \nabla \cdot \sigma \\ -\nabla(p\mathbf{U}) + \nabla \cdot (\sigma \cdot \mathbf{U}) + \nabla \cdot (\kappa \nabla T) \end{pmatrix} \,, \tag{3.3}$$

where σ and κ represent the viscous stress tensor and thermal conductivity of air, respectively. For simulations involving chemical reacting flows, energy equation in (3.1) is replaced by the combustion models as described in Appendix B.3. If inviscid flow is considered, Equation (3.1) will be reduced to the Euler equations by dropping viscous terms (function G), and its conservative form becomes,

$$\partial_t \mathbf{Q} + \nabla \cdot \mathrm{F}(\mathbf{Q}) = 0 \,. \tag{3.4}$$

The linearized conservative form of the nonlinear NS equations is defined as follows,

$$\partial_t \mathbf{Q}' + \nabla \cdot \mathrm{F}'(\overline{\mathbf{Q}}, \mathbf{Q}') - \mathrm{G}'(\overline{\mathbf{Q}}, \mathbf{Q}') = 0 \,, \tag{3.5}$$

where, the perturbation flux function, $\mathrm{F}'(\overline{\mathbf{Q}}, \mathbf{Q}')$, is given by [6],

$$\mathrm{F}'(\overline{\mathbf{Q}}, \mathbf{Q}') = \mathrm{F}(\overline{\mathbf{Q}} + \mathbf{Q}') - \mathrm{F}(\overline{\mathbf{Q}}) \,. \tag{3.6}$$

The perturbation viscous diffusion terms, $\mathrm{G}'(\overline{\mathbf{Q}}, \mathbf{Q}')$ in both momentum and energy equations are defined in (3.7),

$$\mathrm{G}'(\overline{\mathbf{Q}}, \mathbf{Q}') = \begin{pmatrix} 0 \\ \nabla \cdot \sigma' \\ \overline{\mathbf{U}} \cdot \nabla \sigma' + \mathbf{U}' \cdot \nabla \overline{\sigma} + \kappa \nabla^2 T' \end{pmatrix} , \tag{3.7}$$

where,

$$\sigma' = \mu \big[\nabla \mathbf{U}' + (\nabla \mathbf{U}')^{\mathrm{T}} - \frac{2}{3} (\nabla \cdot \mathbf{U}') \mathbf{I} \big] , \tag{3.8}$$

$$\overline{\sigma} = \mu \big[\nabla \overline{\mathbf{U}} + (\nabla \overline{\mathbf{U}})^{\mathrm{T}} - \frac{2}{3} (\nabla \cdot \overline{\mathbf{U}}) \mathbf{I} \big] . \tag{3.9}$$

If inviscid flow is considered, (3.5) can also be further reduced to linearized Euler equations (LEE), the linear counterpart of (3.4), by removing $\mathrm{G}'(\overline{\mathbf{Q}}, \mathbf{Q}')$ term,

$$\partial_t \mathbf{Q}' + \nabla \cdot \mathrm{F}'(\overline{\mathbf{Q}}, \mathbf{Q}') = 0 . \tag{3.10}$$

To couple with the nonlinear region, the perturbed primitive variables can be computed as,

$$\mathbf{U}' = \frac{\overline{\rho \mathbf{U}} + (\rho \mathbf{U})'}{\overline{\rho} + \rho'} - \overline{\mathbf{U}} , \tag{3.11}$$

$$p' = (\gamma - 1) \left[\overline{\rho e_t} + (\rho e_t)' - 0.5 (\bar{\rho} + \rho') || \overline{\mathbf{U}} + \mathbf{U}' ||^2 \right] - \bar{p} , \tag{3.12}$$

$$T' = \overline{T} \left(\frac{p'}{\bar{p}} + \frac{\rho'}{\bar{\rho}} \right) . \tag{3.13}$$

The coupling process between both solvers is presented in Figure 3.3. Inner schematic drawing of Figure 3.3 illustrates a one-dimensional DDT domain. Meanwhile, the outer plot in Figure 3.3 explains the iterative cycle of DDT. Taking inviscid flow problem as an example, the LEE, as defined in (3.10), will be solved in linear region in term of perturbation components of conserved variables, $\mathbf{Q}'$. At the i^{th} iteration, $\mathbf{Q}'_i$ is solved by (3.10) using DRP [73] and LDDRK [74] schemes for spatial and temporal discretizations, respectively. The perturbed primitive variable, ϕ'_i, is then computed based on (3.11), (3.12), and (3.13). The linear primitive variable, ϕ^i_{L}, is obtained by adding up mean ($\overline{\phi}$) and perturbed primitive variables (ϕ'_i) for nonlinear boundary face, ϕ^i_f, interpolation. The nonlinear overset boundary face is linearly interpolated from adjacent linear and nonlinear cell centriods,

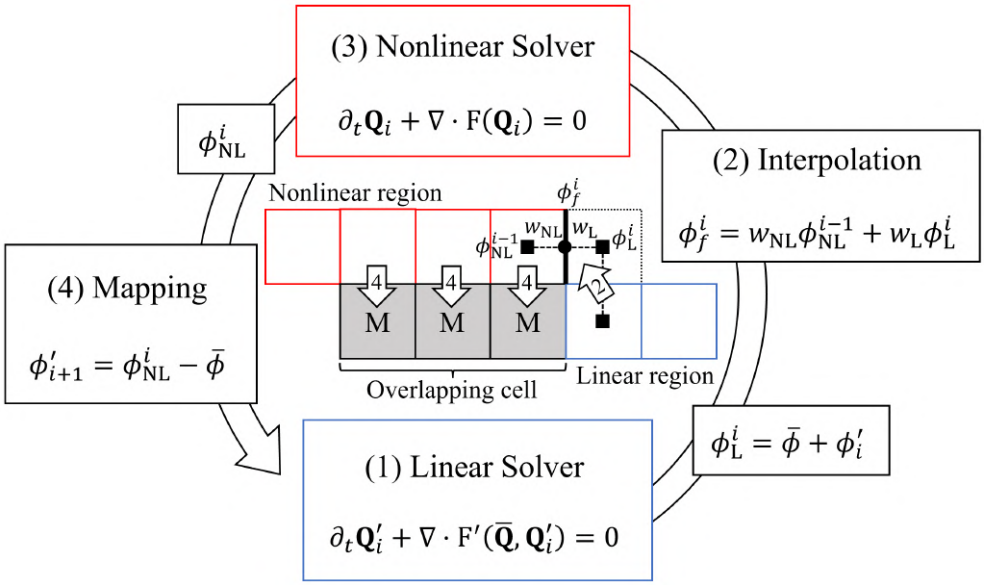

FIGURE 3.3: The coupling between two solvers and regions at the overset boundary, where ϕ is primitive variable and ϕ' is the perturbation.

as follows,

$$\phi^i_f = w_{\mathrm{NL}}\phi^{i-1}_{\mathrm{NL}} + w_{\mathrm{L}}\phi^i_{\mathrm{L}} \,, \tag{3.14}$$

where ϕ^{i-1}_{NL} is the nonlinear variable value at boundary cell centriod from one iteration before i^{th}. w_{NL} and w_{L} are the distance weights of nonlinear boundary face centroid with nonlinear and linear cell centroids, respectively. With the updated nonlinear boundary value, ϕ^i_f, Euler equations are solved in nonlinear region, as defined in (3.4), and obtains up-to-date i^{th} variables, ϕ^i_{NL}, before mapping into nonlinear region. The new perturbed primitive variables, ϕ'_{i+1}, are obtained by,

$$\phi'_{i+1} = \phi^i_{\mathrm{NL}} - \overline{\phi} \,, \tag{3.15}$$

and mapped into the linear region as shown in Figure 3.3. For the next iteration, $(i+1)^{th}$, the new conserved variables, $\mathbf{Q}'_{i+1}$, can be reconstructed from new primitive variables, ϕ'_{i+1}, by (3.11), (3.12), and (3.13) before repeating the cycle again.

3.1.2 Sponge Layer Treatment

A sponge layer [75] is applied at the near-boundary region of the linear zone to absorb any outgoing waves and prevent reflection. Inside the sponge zone, an

artificial damping function, Ω', as shown in (3.16), is added to the right-hand side of (3.5) or (3.10) for viscous or inviscid flow conditions, respectively,

$$\Omega' = \nabla \cdot (\omega(\boldsymbol{x}) \nabla \mathbf{Q}') \ . \tag{3.16}$$

$\omega(\boldsymbol{x})$ is artificial viscosity in terms of the position vector, $\boldsymbol{x}$, that is defined as,

$$\omega(\boldsymbol{x}) = \epsilon_\omega \left(\frac{\boldsymbol{x} - \boldsymbol{x}_s}{L_{\boldsymbol{x}}} \right)^2 \frac{(\Delta x_\mathrm{L})^2}{\Delta t} \ . \tag{3.17}$$

ϵ_ω, $\boldsymbol{x}_s$ and $L_{\boldsymbol{x}}$ represent maximum viscosity strength, sponge layer starting position and length, respectively. Δx_L is the cell size inside the sponge layer whereas Δt refers to the time step. These parameters are defined by users to control the maximum viscosity at the sponge layer boundary.

3.1.3 Explicit Filter Scheme

The short waves are generated once the waves passed interfaces, contaminating the numerical solution. To remove them, an artificial selective damping [76] is implemented in this work as an explicit filtering approach. The damping term is added to right-hand side of governing equations, taking (3.10) as example,

$$\partial_t \mathbf{Q}' + \nabla \cdot \mathrm{F}'(\overline{\mathbf{Q}}, \mathbf{Q}') = \epsilon \sum d_m \mathbf{Q} \ , \tag{3.18}$$

where ϵ and d_m are the filter strength and damping coefficients, respectively. In the finite difference context, a symmetric $(2n+1)$-point filter over a variable, ϕ, is characterized by the weights d_m as follows [77],

$$\phi_i^f = d_0 \phi_i + \sum_{m=1}^{n} d_m (\phi_{i+m} + \phi_{i-m}) \ . \tag{3.19}$$

To convert the coefficients to finite volume context, the coefficients α_j are obtained such that the filter can be written as such,

$$\phi_i^f = \sum_{j=0}^{n} \alpha_j \phi_i^j \ , \tag{3.20}$$

where n represents the order of interpolation of ϕ_i. In general, the n-order of interpolation for field flux variable, ϕ, at i^{th} stencil of uniform grid can be calculated as follows,

$$\phi_i^n = \frac{1}{4^n} \sum_{k=0}^{2n} \binom{2n}{k} \phi_{i-n+k} \ . \tag{3.21}$$

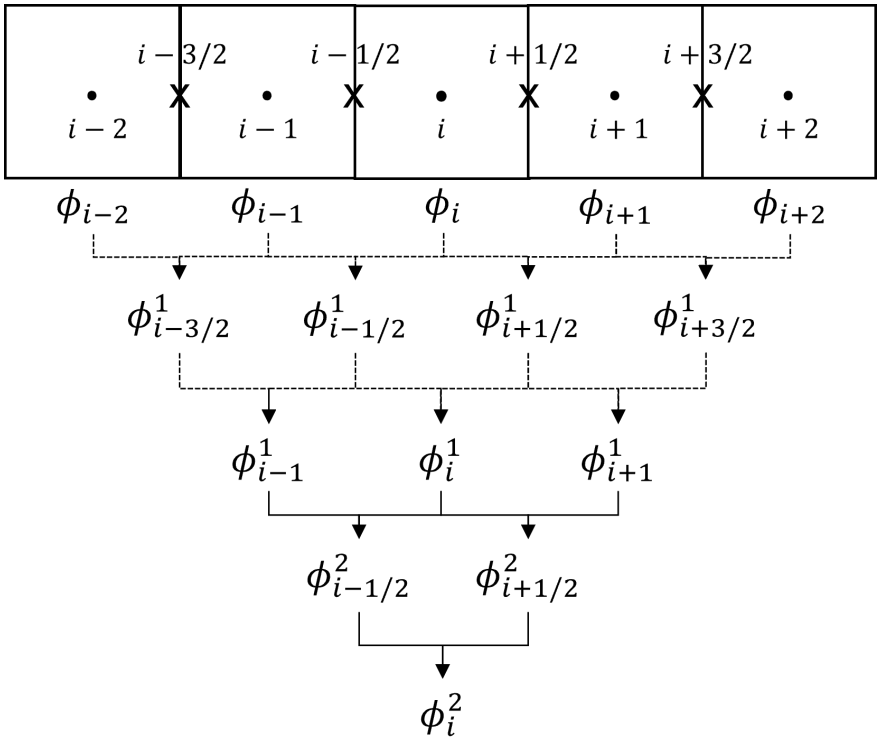

FIGURE 3.4: Second order of interpolation on a uniform grid for 1D mesh.

Assuming a 1D grid as shown in Figure 3.4, a second-order interpolation of i^{th} stencil on uniform grid can be computed based on (3.21) as,

$$\phi_i^2 = \frac{1}{16}(\phi_{i-2} + 4\phi_{i-1} + 6\phi_i + 4\phi_{i+1} + \phi_{i+2}) \ . \tag{3.22}$$

Hence, a coefficient correction for $n = 2$, i.e., 5-point stencil filter in finite volume framework (α_j) can form a linear system with its finite difference formulation (d_i) as follows,

$$\begin{pmatrix} 1 & \frac{1}{2} & \frac{3}{8} \\ \frac{1}{2} & \frac{1}{4} & \frac{1}{4} \\ \frac{3}{8} & \frac{1}{4} & \frac{1}{16} \end{pmatrix} \begin{pmatrix} \alpha_0 \\ \alpha_1 \\ \alpha_2 \end{pmatrix} = \begin{pmatrix} d_0 \\ d_1 \\ d_2 \end{pmatrix} \ . \tag{3.23}$$

The $(2n+1)$-point stencil filter in finite volume framework ($\boldsymbol{\alpha}$) can then be related with $\boldsymbol{d}$ as,

$$U\boldsymbol{\alpha} = \boldsymbol{d}\ , \tag{3.24}$$

where the $\boldsymbol{\alpha}$ coefficients can be solved easily with the elements of the upper triangular matrix U given by,

$$U_{i,j} = \frac{1}{4^j}\binom{2j}{i+j}\ . \tag{3.25}$$

From reference [76], the coefficients of the optimized selective filters using $7-$, $9-$, and $11-$point stencils ($d_j = d_{-j}$) are shown in Table 3.1. The corresponding α coefficients can be computed based on (3.24) and (3.25), as listed in Table 3.2. Thereafter, the $(2n+1)$-point stencil filter is applied to variable of i^{th} stencil, ϕ_i, as:

$$\phi_i^{\text{filtered}} = \phi_i - \epsilon \sum_{j=0}^{n} \alpha_j \phi_i^j\ , \tag{3.26}$$

where ϵ is the filter strength.

TABLE 3.1: Lists of d coefficients

	SFo7p	SFo9p	SFo11p
d_0	0.2873928425	0.243527493120	0.215044884112
d_1	−0.2261469518	−0.204788880640	−0.187772883589
d_2	0.1063035788	0.120007591680	0.123755948787
d_3	−0.0238530482	−0.045211119360	−0.059227575576
d_4	N.A.	0.008228661760	0.018721609157
d_5	N.A.	N.A.	−0.002999540835

TABLE 3.2: Lists of α coefficients

	$n=3$	$n=4$	$n=5$
α_0	1.0000000001	1.00000000000	1.00000000000
α_1	−0.8660387008	−1.22337790976	−1.59037912631
α_2	0.249421868	0.55584754304	1.00353062713
α_3	−0.0238530482	−0.11104041344	−0.313984378057
α_4	N.A.	0.00822866176	0.048717017507
α_5	N.A.	N.A.	−0.002999540835

3.2 Development of Thermoacoustic Nonlinear Solvers

To obtain high-fidelity thermoacoustic solutions, involving the transient and turbulent compressible flow, the implicit large-eddy simulation (LES) [72] is considered. Instead of time-filtering like in Reynolds-averaged Navier Stokes (RANS), LES applies spatial filtering technique by dividing the flow scales into large and small eddies. The large-scale eddies, containing most of the flow characteristics, driving mechanisms, and large portion of kinetic energy, are resolved directly to maintain the flow features. The small (sub-grid scale) eddies, responsible for viscous dissipation, are modeled by appropriate eddy dissipation model to ensure the turbulence closure. For LES, the unsteady filtered version of continuity and Navier Stokes' equations are considered,

$$\frac{\partial \overline{\rho}}{\partial t} + \frac{\partial (\overline{\rho}\widetilde{U_j})}{\partial x_j} = 0 \ , \tag{3.27}$$

$$\frac{\partial (\overline{\rho}\widetilde{U_i})}{\partial t} + \frac{\partial}{\partial x_j}(\widetilde{\overline{\rho}U_i U_j}) = -\frac{\partial \widetilde{p}}{\partial x_i} + \frac{\partial}{\partial x_j}(\widetilde{\tau_{ij}} + \widetilde{\tau_{sgs}}) \ . \tag{3.28}$$

Since the spatial filtering method is not the focus of this work, it will not be discussed here. The viscous stress term consists of molecular stress, $\widetilde{\tau_{ij}}$, and unsolved sub-grid stress, $\widetilde{\tau_{sgs}}$. In brief, $\widetilde{\tau_{ij}}$ is resolved directly and responsible for the breakdown of eddy larger than grid size into smaller eddy, whereas $\widetilde{\tau_{sgs}}$ is modelled to enhance the dissipation of the eddy with size smaller than grid. There are several available sub-grid scale (SGS) models in OpenFOAM, including *Smagorinsky* [78], *WALE* [79] and *kEqn* [80]. The *kEqn* SGS model is considered in this work due to its suitability for compressible jet flows under buoyancy effect.

For the simulations involving chemical reactions, either direct solving of the chemical kinetics or combustion modelling for turbulence-chemistry closure is needed. The former requires tremendous costs due to the typical large amount of species, whereas the latter can reduce the resources by having just two to three additional passive scalar transport equations. For example, the diffusion flame can be modeled by incorporating the flamelet/progress-variable (FPV) model [81, 82], whereas the flame prolongation of intrinsic low-dimensional manifolds (FPI) model [83, 84] can

be used to simulate the premixed flames. Both models utilize tabulation method described by additional passive scalars, such as mixture fraction, Z, its variance, Z''^2, and progress variable, C, for thermo-chemical data. They are coupled with flow solver by transporting the scalars as in (B.15) to (B.17). The developments of solvers and models are described in Appendix B.3.

Chapter 4

DDT in 2D Applications

This chapter presents results for the DDT in 2D. The scheme is first validated with theoretical solution available for wave propagation. One-dimensional study of an acoustic/entropy wave interaction with standing shock wave in [6] was reproduced using the 2D extension for validation study. After validations, DDT is applied to internal and external inviscid flows, as well as non-isothermal viscous flow problems. Numerical sensitivity studies such as domain and cell size of nonlinear and linear regions were examined. The initial perturbation function for plane source, point source, and periodic wave are, respectively, given by,

$$\forall y \in \Re\,, \quad G(x; x_0, \sigma) = \exp\left[-\ln 2 \left(\frac{x - x_0}{\sigma} \right)^2 \right], \tag{4.1}$$

$$H(\boldsymbol{x}; \boldsymbol{x}_0, \sigma) = \exp\left[-\ln 2 \left(\frac{|\boldsymbol{x} - \boldsymbol{x}_0|}{\sigma} \right)^2 \right], \tag{4.2}$$

$$F(\boldsymbol{x}, t; \boldsymbol{x}_0, \sigma, f) = \exp\left[-\ln 2 \left(\frac{|\boldsymbol{x} - \boldsymbol{x}_0|}{\sigma} \right)^2 \right] \cos(2\pi f t)\,, \tag{4.3}$$

where the x_0, σ and f are the wave center location, half-width of the Gaussian profile, and frequency of the periodic wave, respectively.

4.1 Validation

An acoustic wave in a stationary flow in a duct was used to validate the 1D/2D DDT code. The computational domain of a rectangular duct comprises of linear

($x_{\mathrm{L}} \in \{[-15,-5],[5,15]\}$) and nonlinear ($x_{\mathrm{NL}} \in [-5,5]$) regions with height $y \in [-1,1]$, as shown in Figure 4.1. In all cases, both regions were discretized into uniform cells with $\Delta x = \Delta y = 0.05$. Hence, the overlap ratio $R = \Delta x_{\mathrm{L}}/\Delta x_{\mathrm{NL}} = 1$.

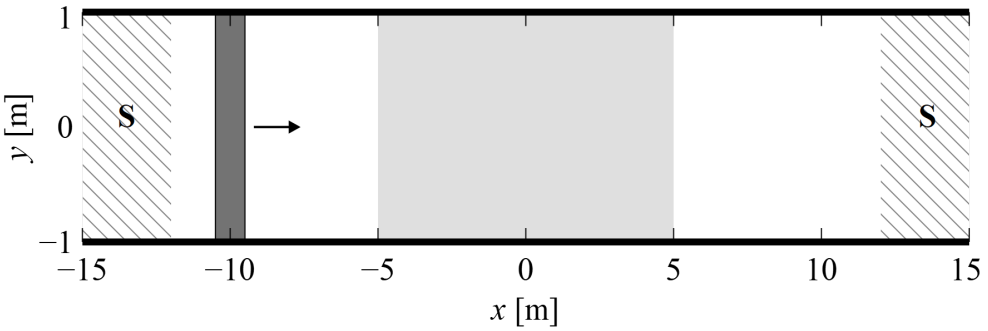

FIGURE 4.1: Schematic illustration of 2D DDT domain with a plane acoustic wave propagates to the right. Nonlinear region and sponge zone (**S**) are shaded in grey and lines, respectively.

Sponge zones were applied in linear region $x_{\mathrm{L}} \in [-15,-12]$ and $[12,15]$ with maximum strength of 0.05. No filtering was implemented in this simulation. A right-travelling plane acoustic wave was initialized at $x = -10$ as follows,

$$p'(x,y,0) = 0.01G(x;-10,0.5)\ , \tag{4.4a}$$

$$\mathbf{U}'(x,y,0) = \frac{0.01}{1.4}G(x;-10,0.5)\ , \tag{4.4b}$$

$$\rho'(x,y,0) = 0.01G(x;-10,0.5)\ . \tag{4.4c}$$

The mean states in the linear region were set as follows,

$$\overline{p}(x,y,t) = 1, \quad \overline{\mathbf{U}}(x,y,t) = 0, \quad \overline{\rho} = 1.4\ . \tag{4.5}$$

The initial states of nonlinear region were

$$p(x,y,0) = 1, \quad \mathbf{U}(x,y,0) = 0, \quad \rho(x,y,0) = 1.4\ . \tag{4.6}$$

Both 1D and 2D DDT cases were simulated with a timestep of $\Delta t = 0.01$ s and up to $t = 30$ s. The normalized wave (along $y = 0$ for 2D case) moves from the left linear to the right linear region through the nonlinear region at selective instants, $t = \{2,8,17,25\}$ s, are presented in Figure 4.2 and compared with the exact solution. The 1D and 2D DDT simulations yield exactly the same results. At $t = 8$ s, the

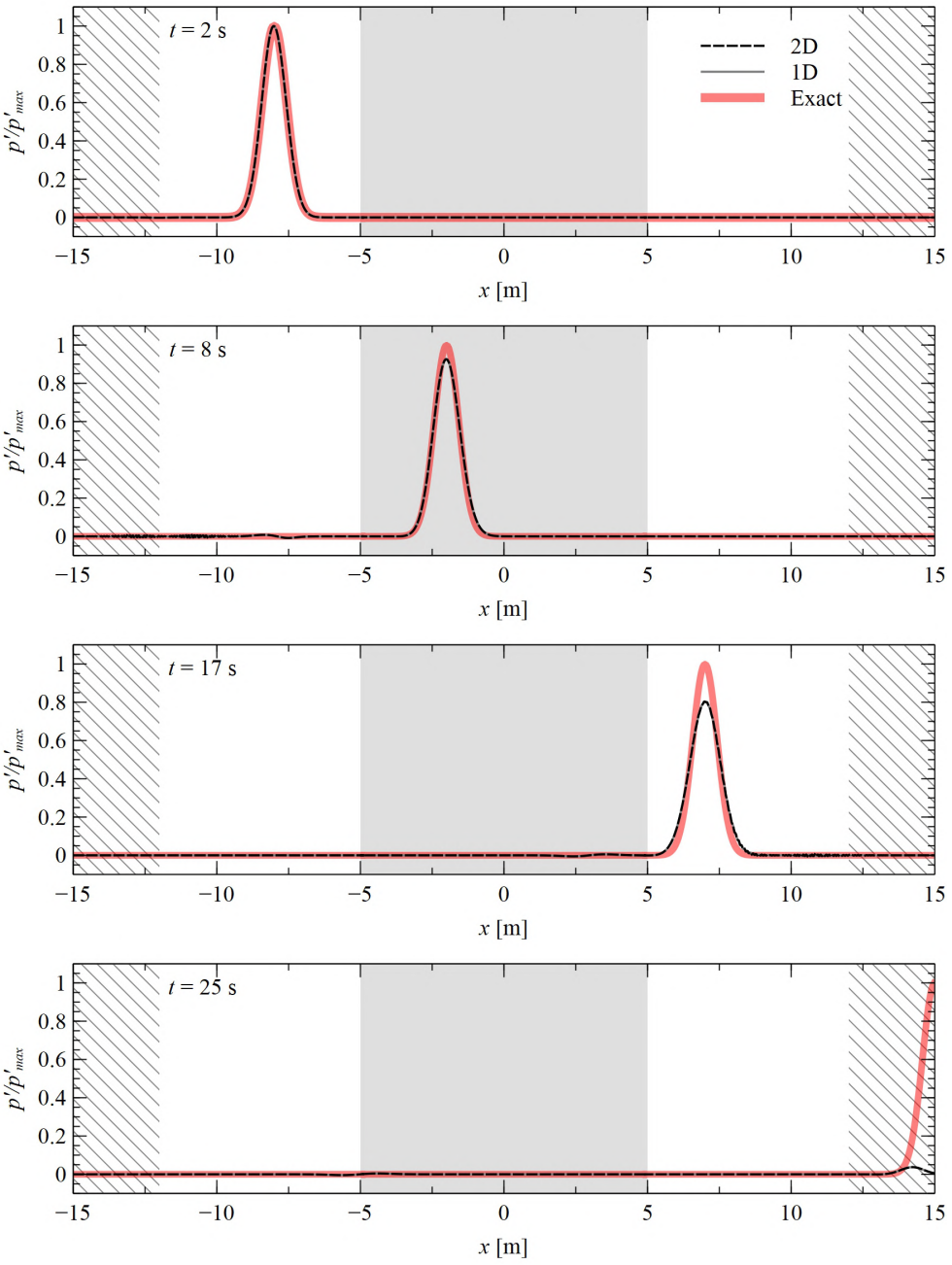

FIGURE 4.2: Comparison of 1D and 2D domain decomposition results with exact solution. Nonlinear region is shaded grey. Sponge zone is shaded with lines.

wave fully propagates into nonlinear region. At $t = 17$ s, the wave flattens, has wider width and lower peak compared with the exact solution. This is expected as the nonlinear region incurs additional dispersion and dissipation. Last row in Figure 4.2 shows the wave absorption in the sponge zone, which effectively prevents wave reflection. Hence, the same settings of sponge zone layers and strength will be used for the remaining simulations in this case study.

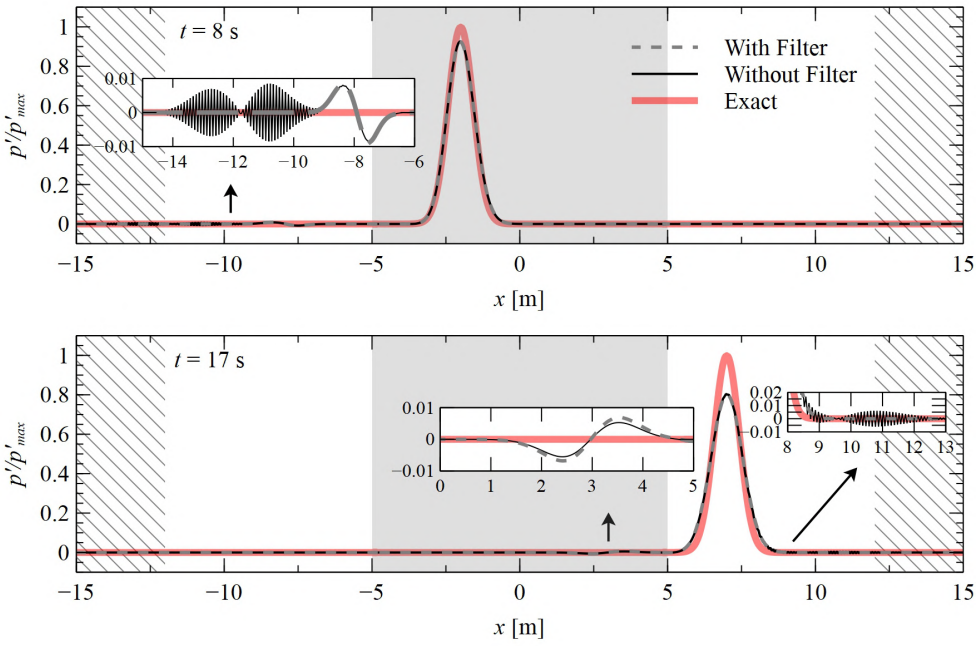

FIGURE 4.3: Elimination of the spurious waves by a 9-point explicit filter scheme.

At $t = 8$ s, spurious waves (short waves) and wave tail (black line) were observed respectively in left linear region of $x \in [-14, -9]$ and $[-9, -7]$ due to the wave travels from linear to nonlinear region, as presented in close-up plots of Figure 4.3. Similar spurious waves and wave tail were observed on the right and left sides of the wave at $t = 17$ s while the wave leaves the nonlinear region and enters linear region. These short waves can be removed by filtering the fields using 9-point explicit filter scheme [76] with filter strength of 0.5 based on numerical testing and remains the same for all simulations in this validation study. The corresponding filtered results are illustrated as grey dashed-line in Figure 4.3, showing the disappearance of spurious waves after the acoustic wave enters and leaves the nonlinear region. The filter scheme has shown its capability in eliminating short waves and preserving long wave simultaneously. The wave tail can be minimized by using higher overlap ratio R, which also helps in minimizing dissipation.

4.1.1 Effect of Overlap Ratio

To prove the overlap ratio parameter can be used to minimize dissipation error and wave tail observed in previous section, one- and two-dimensional simulations of a right-travelling wave propagation under a stationary infinite pipe

flow were conducted for different overlap ratio, R. For all cases, the linear ($x_{\mathrm{L}} \in \{[-100, -25], [25, 100]\}$) and nonlinear ($x_{\mathrm{NL}} \in [-25, 25]$) regions were discretized uniformly both in axial and transverse directions for the 2D case.

The linear region cell resolution was fixed for all cases, $\Delta x_{\mathrm{L}} = 1$. Two overlap ratio, $R = 1$ and 10 were chosen, corresponding to the nonlinear region grid resolution of $\Delta x_{\mathrm{NL}} = 1$ and 0.1, respectively. For 2D simulation, the cell width in transverse direction was fixed for both linear and nonlinear regions, $\Delta y = 0.1$ for $y \in [-0.5, 0.5]$. The mean states in both regions were initialized as such,

$$\bar{p}(x, y, t) = 1, \quad \overline{\mathbf{U}}(x, y, t) = 0, \quad \bar{\rho}(x, y, t) = 1.4 \; . \tag{4.7}$$

Instead of introducing sponge zone at both ends, periodic boundary conditions were implemented to simulate the effect of long distance acoustic waves propagation. An initial Gaussian wave was initialized as,

$$p'(x, y, 0) = \epsilon G(x; -65, 6) \; , \tag{4.8a}$$

$$\mathbf{U}'(x, y, 0) = \frac{\epsilon}{1.4} G(x; -65, 6) \; , \tag{4.8b}$$

$$\rho'(x, y, 0) = \epsilon G(x; -65, 6) \; , \tag{4.8c}$$

where $\epsilon = 10^{-5}$. All cases were computed with CFL $= 0.5$ until $t = 200$ s, which is one cycle.

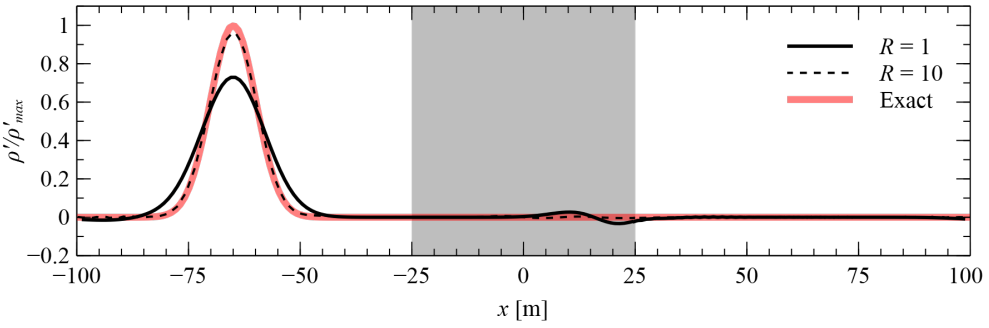

FIGURE 4.4: Propagation of a single acoustic wave under different overlap ratios, R in 2D simulations at $t = 200$ s.

For 2D simulations, the normalized ρ' waves for $R = 1$ and 10 cases are plotted in Figure 4.4 at $t = 200$ s. The observed significant dissipation error and wave tail at $x \in [1, 26]$ in the $R = 1$ case are minimized when $R = 10$ is used. Hence, the solver was observed to have better results with $R = 10$ than with $R = 1$.

TABLE 4.1: Relative CPU hours for different types of simulations of an acoustic wave propagation.

Simulation types	Mesh	Δt	Relative CPU hours
Linear	$\Delta x_{\mathrm{L}} = 1$	0.50	1.00
Nonlinear	$\Delta x_{\mathrm{NL}} = 1$	0.50	1.29
	$\Delta x_{\mathrm{NL}} = 0.5$	0.25	3.29
	$\Delta x_{\mathrm{NL}} = 0.2$	0.10	13.57
	$\Delta x_{\mathrm{NL}} = 0.1$	0.05	43.71
DDT	$R = 1$	0.50	1.14
	$R = 2$	0.25	2.71
	$R = 5$	0.10	8.14
	$R = 10$	0.05	20.14

The 1D and 2D results at $R = 10$ agree exactly with each other and match the theoretical result. The capability of the solver in higher dimensions has been proven. Table 4.1, adapted from reference [6], compares the required CPU hours of fully nonlinear and DDT simulations with respect to fully linear propagation solution of a single acoustic wave. The CPU hours incurred for both fully nonlinear and DDT simulations increase when the number of cell increases. The increment rate of CPU hours for DDT is lower than fully nonlinear simulations, indicating the initials computational advantage.

4.1.2 Interaction of An Acoustic/Entropy Wave with A Standing Shock Wave

Besides wave propagation, a wave interaction condition is considered for a more challenging validation case of the 2D DDT. Hence, the interaction of acoustic/entropy wave with a standing shock wave in [6] was replicated. For both 1D and 2D simulations, the nonlinear region ranges between $x \in [-5, 5]$, whereas the linear region covers between $x \in \{[-150, -5], [5, 150]\}$ with sponge layer width and strength of 20 and 0.025, respectively, at both ends, $x \in \{[-150, -130], [130, 150]\}$. In the transverse direction of 2D case, $y \in [-0.5, 0.5]$, the cells were discretized uniformly with $y_{\mathrm{NL}} = y_{\mathrm{L}} = 0.1$. The linear region cells in x direction were uniformly discretized as well, $x_{\mathrm{L}} = 1$. The nonlinear cells, however, were non-uniformly discretized, for which the nonlinear region $(2 < |x_{\mathrm{NL}}| < 5)$ where the cells are mapped onto the linear region will have uniform cell size of $x_{\mathrm{NL}} = 0.1$, while the inner

nonlinear cell size was refined geometrically from $x_{\mathrm{NL}} = 0.1$ until $x_{\mathrm{NL}} = 0.001$ is achieved at $x = 0$ in a symmetric manner.

A standing shock wave was initialized at $x = 0$ with Mach number, $M = 3$, on the supersonic side, whereas the subsonic side can be related as such,

$$\bar{p}(x,t) = p(x,0) = \begin{cases} 1\ , & x < 0 \\ \frac{2\gamma M^2 - \gamma + 1}{\gamma + 1}\ , & x > 0 \end{cases}\ , \tag{4.9a}$$

$$\overline{\mathbf{U}}(x,t) = \mathbf{U}(x,0) = \begin{cases} M\ , & x < 0 \\ \frac{(\gamma-1)M^2+2}{(\gamma+1)M}\ , & x > 0 \end{cases}\ , \tag{4.9b}$$

$$\bar{\rho}(x,t) = \rho(x,0) = \begin{cases} 1.4\ , & x < 0 \\ \frac{1.4(\gamma+1)M^2}{(\gamma-1)M^2+2}\ , & x > 0 \end{cases}\ . \tag{4.9c}$$

There are three types of linear waves can propagate in 1D uniform mean flow at speeds of $u \pm c$ (two acoustic waves) and u (entropy wave). c denotes as sound speed and equal to $\sqrt{\gamma \mathrm{R} T}$, where R = 287 for air. Once the $(u \pm c, c)$ waves interact with standing shock, only $u + c$ and c waves can propagate away from shock wave meanwhile the standing shock will shift its position. For conciseness, the quantities on the supersonic (left) and subsonic (right) sides are denoted with subscript 'l' and 'r', respectively. A $u_l + c_l$ wave was introduced to the domain as follows,

$$p'(x,0) = \epsilon G(x; -65, 12)\ , \tag{4.10a}$$

$$\mathbf{U}'(x,0) = \frac{\epsilon}{1.4} G(x; -65, 12)\ , \tag{4.10b}$$

$$\rho'(x,0) = \epsilon G(x; -65, 12)\ , \tag{4.10c}$$

where the $\epsilon = 10^{-2}$.

The interactions between the incoming acoustic wave and the standing shock wave will generate right propagating acoustic and entropy waves downstream of the shock wave. Figure 4.5 compares the normalized p' and ρ' waves from the 1D [6] and 2D simulations, showing excellent agreement. To demonstrate the effective two-way coupling, a close-up view of the dimensionless pressure near the shock wave is shown for both simulations in the right column of Figure 4.5. For both 1D and 2D results, the shock front translates downstream from its interaction with the acoustic wave, settling at a new position of approximately $x = 0.05$ (i.e.,

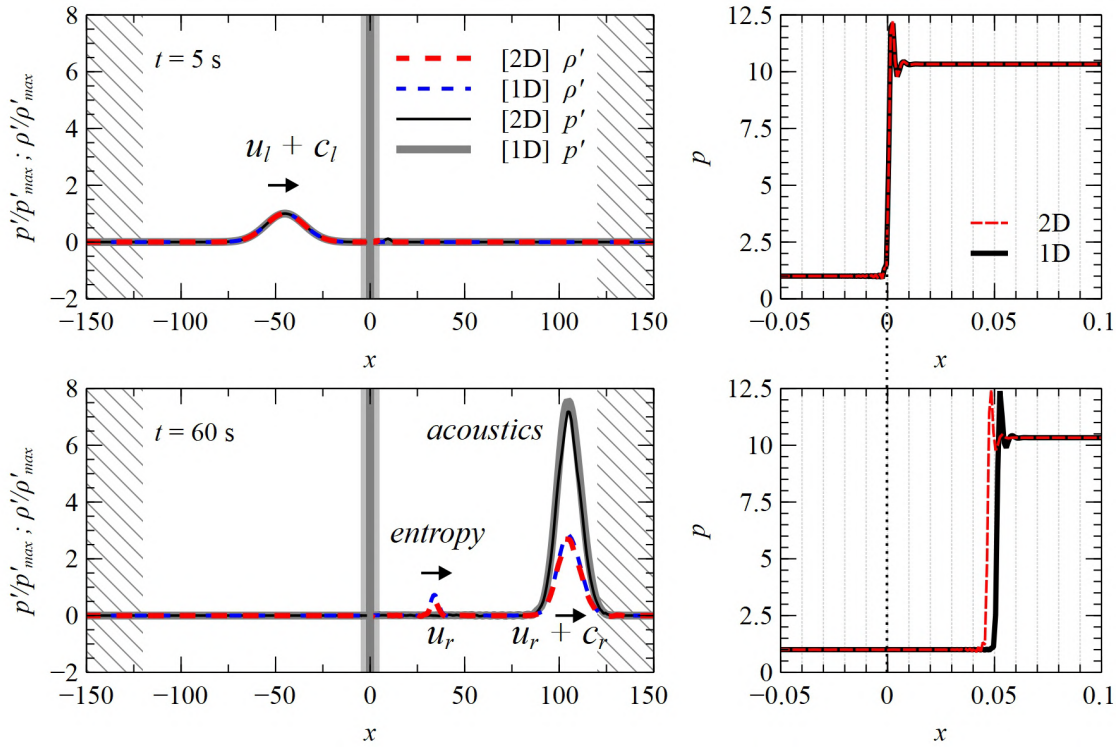

FIGURE 4.5: Comparison of 1D and 2D for interaction of a $u_l + c_l$ acoustic wave with a $M = 3$ standing shock with $\epsilon = 10^{-2}$. The standing shock is located within the dark grey region.

approximately 50 grid spacings from pre-interaction shock location of $x = 0$) after the prescribed acoustic wave leaves the nonlinear zone

The results presented in Figure 4.5 demonstrates that the linear wave prescribed in the linear supersonic region (i.e., $x < 0$) can propagate into the nonlinear zone and interact with the shock, then further disperse into an acoustic and entropy waves that propagate downstream into the linear subsonic region (i.e., $x > 0$). Hence, the two-way coupling feature of DDT is illustrated. Overall, the comparable 1D and 2D DDT simulation results of the validation case confirm that the method has been correctly extended to the higher spatial dimension.

4.2 Internal Flow: Converging-Diverging Nozzle

The 2D DDT was validated with rectangular pipe flow conditions with or without shock wave. However, all the validation cases do not have any significant variance in the transverse direction. Hence, a converging-diverging (CD) nozzle configuration

was chosen to showcase the true two-dimensionality and emulate scenario of jet engine exit nozzle where the upstream noise/acoustic wave propagates as illustrated in Figure 4.6.

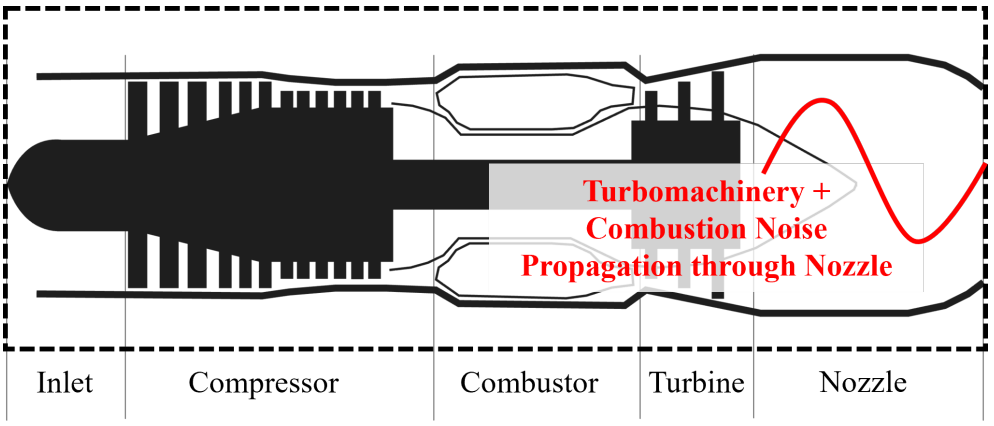

FIGURE 4.6: Upstream noise propagates through nozzle.

Under this section, the CD nozzle simulations was performed under different internal flow regimes: (i) subsonic and (ii) supersonic flows, as presented in Sections 4.2.1 and 4.2.2, respectively. The mesh independence study of fully nonlinear simulation was first investigated using '*buoyantPimpleFoam*' without buoyancy effect. Thereafter, DDT was adopted by dividing the computational domain into linear and nonlinear regions and using procedure (**b**) in Figure 3.2. The size of nonlinear region was examined to study its effects on wave propagation. Given the optimum nonlinear region size, DDT simulations with various overlap ratio, R, were conducted and compared with fully nonlinear simulations.

4.2.1 Subsonic Flow Regime

The schematic drawing of the subsonic CD nozzle is shown in Figure 4.7. The convergent and divergent contours are defined respectively as follow,

$$y = 1.5 \mp 0.5\cos\left(\frac{\pi x}{x_i}\right) \qquad \text{for} \quad x_i \leqslant x \leqslant 0\ , \tag{4.11}$$

$$y = 1.25 \mp 0.25\cos\left(\frac{\pi x}{x_o}\right) \qquad \text{for} \quad 0 < x \leqslant x_o\ , \tag{4.12}$$

where $x_i = -3$ m and $x_o = 3$ m. The half throat height, h_t, measured from symmetric axis at $x = 0$ m is 1 m.

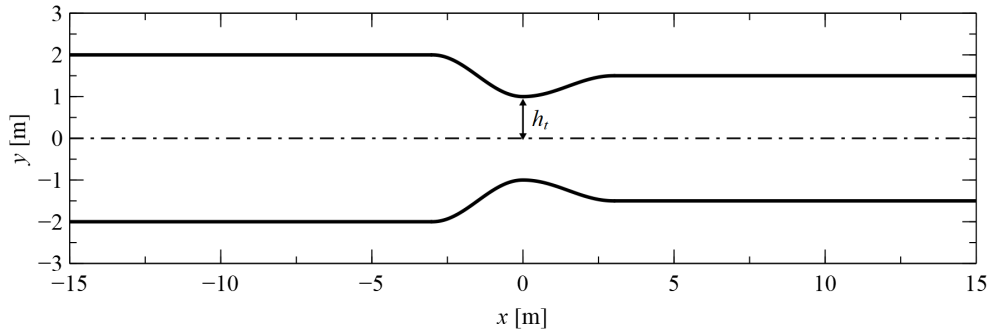

FIGURE 4.7: Computational domain of a converging-diverging nozzle simulation with half throat height, $h_t = 1$ m.

4.2.1.1 Mesh Independence Study

The entire computational domain was defined as a nonlinear region with uniform cell size $\Delta x = \Delta y = 0.05$ m. At the inlet, $x = -15$ m, its pressure and temperature boundary conditions were defined as unity total pressure, $p_0 = 1$, and total temperature, $T_0 = 1$, respectively. At outlet, $x = 15$ m, the pressure, often called back pressure, $p_b = 0.89$, and the temperature was assumed to be adiabatic. The fluid is an inviscid compressible flow and obeys ideal gas law. Slip wall condition was applied to the wall. The speed of sound, $a = 1$ while heat capacity ratio, $\gamma = 1.4$, and gas constant, R $= 1/1.4$. The simulation with CFL number of 0.3, was conducted until it reached the steady state.

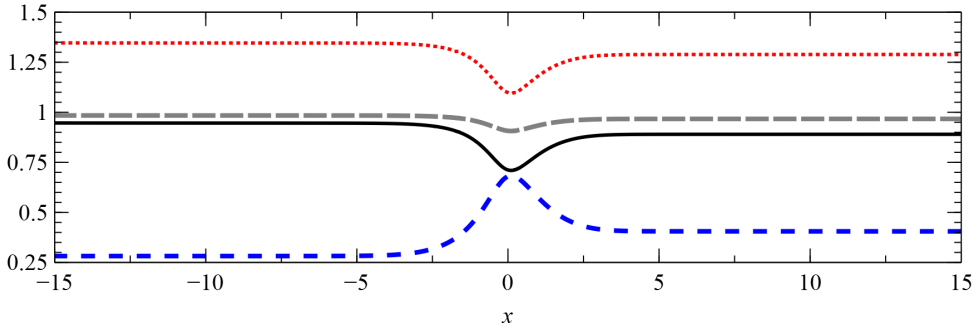

FIGURE 4.8: Steady states of the static pressure, $\overline{p}$ (black solid line), axial velocity, $\overline{\mathbf{U}}_x$ (blue short dashed-line), density, $\overline{\rho}$ (red dotted line), and temperature $\overline{T}$ (grey dashed-line).

Figure 4.8 presents the mean states of various variables along the symmetric axis (i.e., $y = 0$ m). Flow inside the nozzle is completely subsonic. It accelerates in the convergent segment, $x \in [-3, 0]$, from 0.28 to its maximum value 0.68 at the throat. Thereafter, the flow decelerated via the divergent segment, $x \in [0, 3]$, to 0.41 and maintains to the nozzle downstream. In contrast, the mean (static) pressure, $\overline{p}$,

decreases from 0.95 in the convergent segment to a minimum 0.71 at the throat, and increases to 0.89 in the divergent segment. Similar trends are observed for mean temperature, $\overline{T}$, and density, $\overline{\rho}$.

Upon reaching steady state, the acoustic plane wave was introduced to the domain. Hence, p, $\mathbf{U}$, and ρ are initialized with the combination of existing mean state and acoustic wave as defined below,

$$p(x, y, 0) = \overline{p}(x, y) + 0.01G(x; -10, 0.5) \ , \tag{4.13a}$$

$$\mathbf{U}(x, y, 0) = \overline{\mathbf{U}}(x, y) + \frac{0.01}{1.4}G(x; -10, 0.5) \ , \tag{4.13b}$$

$$\rho(x, y, 0) = \overline{\rho}(x, y) + 0.01G(x; -10, 0.5) \ . \tag{4.13c}$$

CFL number was set to be 0.12. Simulation time was up to $t = 30$ s. This fully nonlinear CD nozzle simulation was then repeated for:

(i) $\Delta x_{\text{NL}} = \Delta y_{\text{NL}} = 0.025$ m,

(ii) $\Delta x_{\text{NL}} = \Delta y_{\text{NL}} = 0.0075$ m,

(iii) $\Delta x_{\text{NL}} = \Delta y_{\text{NL}} = 0.00325$ m.

The normalized waves propagated from left to right at $t = \{2, 5, 10, 15\}$ s, are presented in Figure 4.9 for different cell sizes. Multiple humps, as indicated by **B**, are the reflection waves as the consequence of wave passing the converging-diverging section. During initialization of the acoustic wave, a fictitious wave **A** is generated and travels to left and rebounds when hitting the boundary, but only for coarse mesh resolutions. This artificial wave is greatly reduced for finer mesh resolution $\Delta x_{\text{NL}} = 0.0075$ m and $\Delta x_{\text{NL}} = 0.00325$ m. Hence, the results are converged at cell size of $\Delta x_{\text{NL}} = 0.0075$ m. Next, DDT will be implemented to improve the wave propagation, prevent reflection as well as reduce the computational cost.

4.2.1.2 Effect of Nonlinear Region Size

The mean state results obtained from fully nonlinear cases were used to initialize the DDT simulations. Same configuration as shown in Figure 4.7 was used but the computation domain consists of two regions, namely linear and nonlinear region

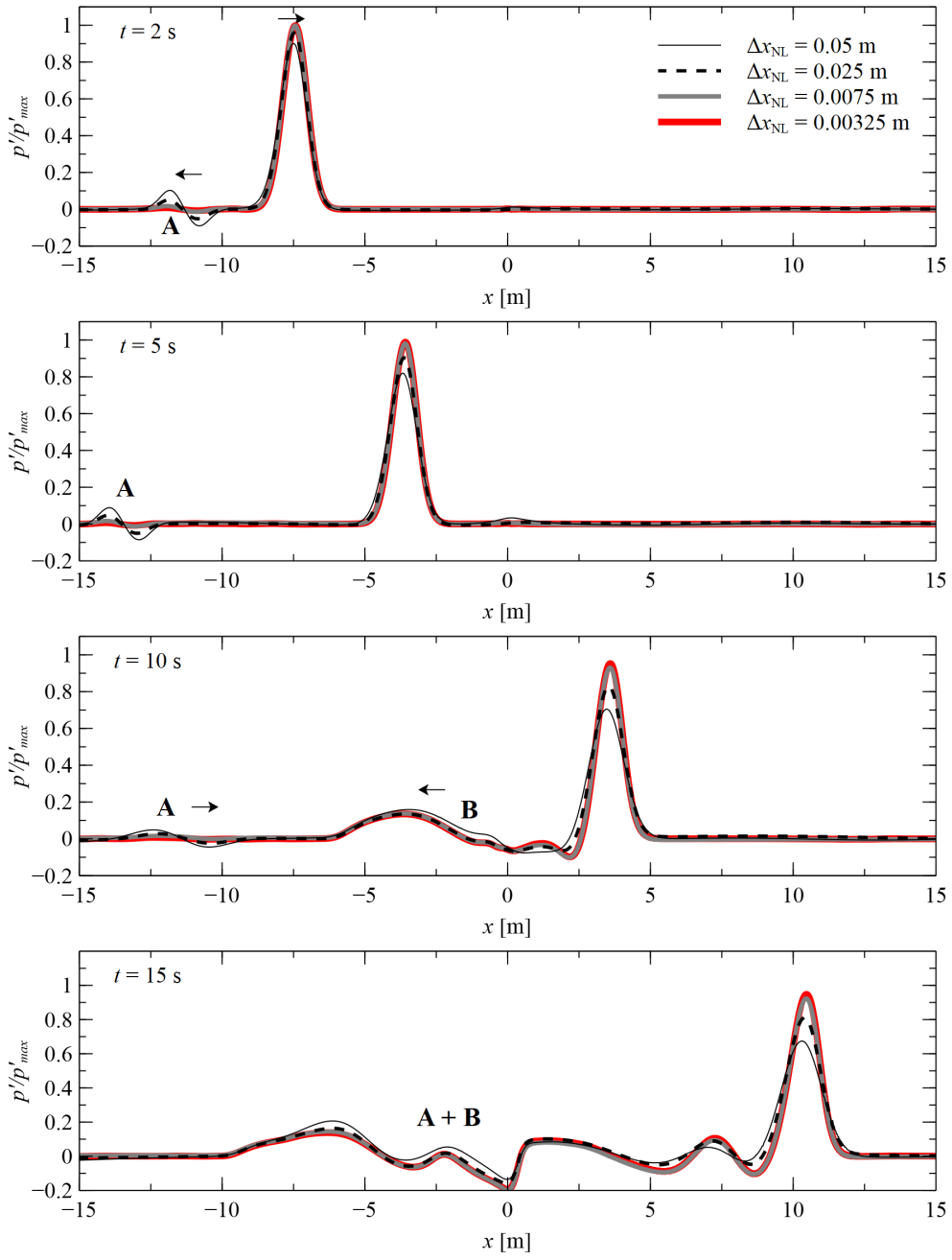

FIGURE 4.9: Comparison of normalized acoustic wave profile for different cell sizes of fully nonlinear CD nozzle cases at various times, where $p'_{max} = 0.01$. It showed the simulations were converged at $\Delta x_{\mathrm{NL}} = 0.0075$ m.

with mesh resolutions $\Delta x_{\mathrm{L}} = 0.05$ m and $\Delta x_{\mathrm{NL}} = 0.0075$ m, respectively, so $R = 20/3$. Different ranges of nonlinear domain were chosen to investigate its effect on the wave propagation. Basically, it is to study how far should the nonlinear domain extends such that the mean states of the linear region remain unchanged and the dissipation error incurred in nonlinear region is minimized. Two ranges

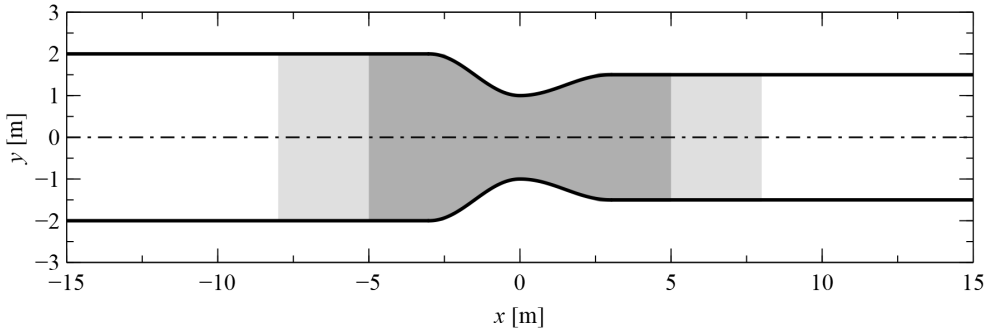

FIGURE 4.10: Two nonlinear region sizes $x_{\mathrm{NL}} \in [-5, 5]$ and $[-8, 8]$, as indicated in the shading area of the CD nozzle.

were selected, they were $x_{\mathrm{NL}} \in [-5, 5]$ and $[-8, 8]$ as shown in Figure 4.10 as grey zones. In the linear region, the 7-point DRP [73] and 9-point artificial selective damping [76] schemes (sponge zone) were implemented. The sponge zone was defined near to the boundary of linear region, where $x \in [-15, -12]$ and $[12, 15]$.

In Section 4.2.1.1, settings of CFL = 0.12, initiated acoustic wave as in Equation (4.13) and inviscid flow condition were used in this DDT nonlinear region size study. Figure 4.11 has shown that there is no significant difference between the two results despite the slight phase shift for large nonlinear region case. The discrepancies can be attributed to the extended nonlinear region, which increases the dissipation and dispersion errors. The DDT simulations also demonstrate qualitative agreement with fully nonlinear solution. Thus, the following DDT simulations will be conducted with smaller nonlinear region defined between $-5 \leqslant x \leqslant 5$ for different overlap ratio, R.

4.2.1.3 Comparison of DDT and Fully Nonlinear Simulations

Two additional DDT simulations were conducted with overlap ratio $R = 1$ and 2. The linear region cell size was fixed at $\Delta x_{\mathrm{L}} = 0.05$ m. The wave profiles at $t = 5$ s, 15 s and 20 s of three DDT cases as well as fully nonlinear with $\Delta x_{\mathrm{NL}} = 0.0075$ m were compared in Figure 4.12. The distortion is minimized while wave enters nonlinear region for $R = 20/3$ as illustrated in Figure 4.12 at $t = 5$ s. At $t = 15$ s, it shows that the dissipation error decreases when the overlap ratio R increases. No wave reflection is observed for all DDT simulations since sponge zone was applied to linear region, whereas the fully nonlinear simulation (grey line) shows reflected wave on the right boundary at $t = 20$ s.

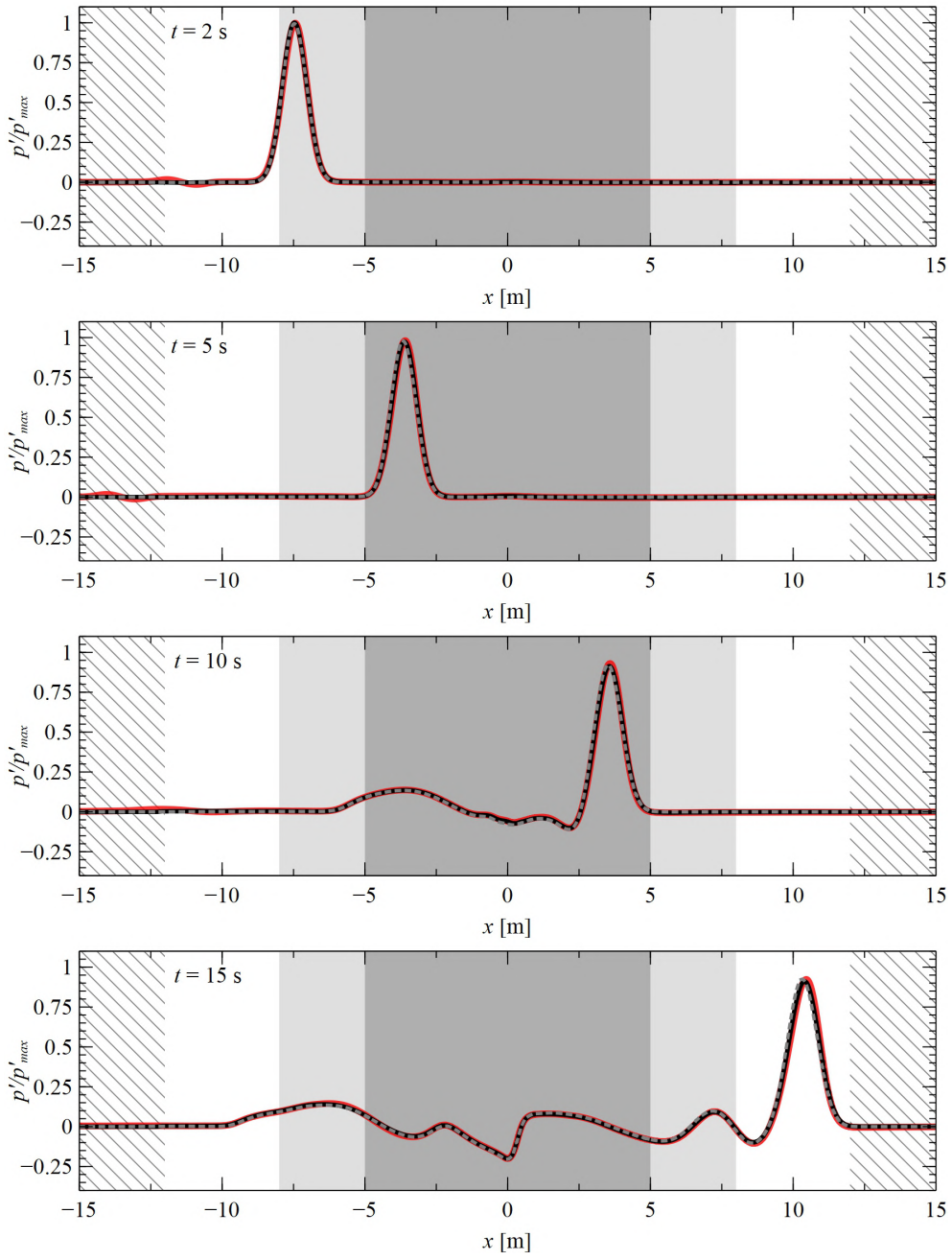

FIGURE 4.11: Time sequence of wave propagation inside CD nozzle for comparison of two nonlinear region sizes, $x_{\mathrm{NL}} \in [-5, 5]$ (grey dotted-line) and $[-8, 8]$ (black solid line) with converged fully nonlinear solution (red thick line). Sponge zone is shaded with lines.

Error analysis was done through evaluation of the root-mean-square deviation (RMSD), taking nonlinear case with $\Delta x_{\mathrm{NL}} = 0.0075$ m as the reference. RMSD

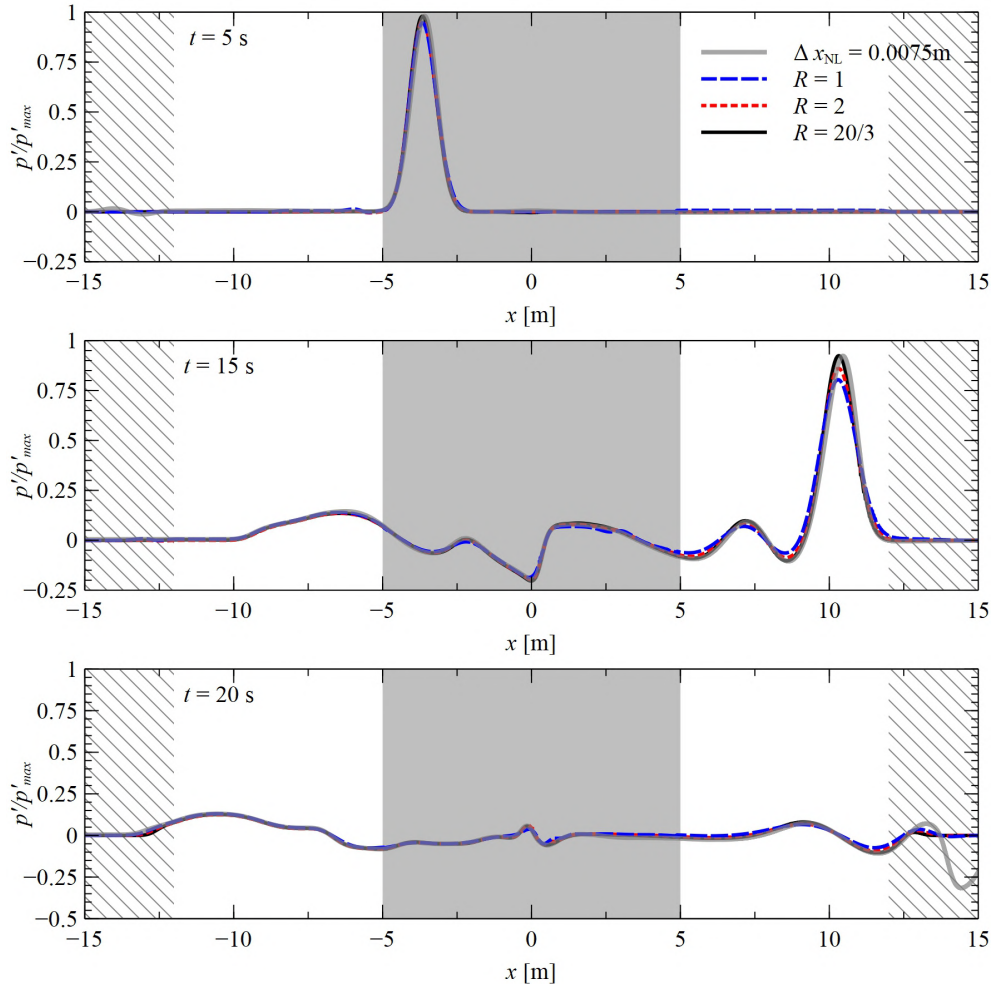

FIGURE 4.12: Comparison the acoustic wave profile at $t = 5$ s, 15 s and 20 s for various types of computation and mesh resolutions. The shaded zone indicates the nonlinear region for domain decomposition simulations at various R. Linear region cell size is fixed at $\Delta x_{\mathrm{L}} = 0.05$ m.

was computed as follows,

$$\mathrm{RMSD} = \sqrt{\frac{\sum_{i=1}^{N} \left(p'_i - p'_{i,ref}\right)^2}{N}}\,, \tag{4.14}$$

where N is the total number of points along the symmetric axis, $y = 0$ m. The results at $t = 15$ s are summarized in Table 4.2. In general, at each time, the RMSD decreases from coarse to fine grid resolutions and when increasing R. The required relative CPU hours of all cases with respect to the converged fully nonlinear simulation ($\Delta x_{\mathrm{NL}} = 0.0075$ m) are also listed in Table 4.2. For $R > 1$, the DDT simulations always have smaller RMSD and took less CPU hours than their corresponding fully nonlinear simulation. For instance, the required CPU hours for

DDT case of $R = 20/3$ is just at most 16% of its corresponding converged nonlinear case yet obtaining satisfactory results. These additional costs needed for $R = 1$ can be attributed to extra mappings and interpolations happened at the overset boundary.

TABLE 4.2: Comparison of root-mean-square deviation and relative CPU hours for different computational types of various mesh resolution at $t = 15$ s using $\Delta x_{\mathrm{NL}} = 0.0075$ m as reference case.

Simulation types	Resolution	RMSD	Relative CPU hours
Nonlinear	$\Delta x_{\mathrm{NL}} = 0.05$	6.39×10^{-4}	0.00165
	$\Delta x_{\mathrm{NL}} = 0.025$	3.50×10^{-4}	0.0218
	$\Delta x_{\mathrm{NL}} = 0.0075$	–	1.0
DDT*	$R = 1$	3.53×10^{-4}	0.002
	$R = 2$	2.11×10^{-4}	0.0054
	$R = 20/3$	1.30×10^{-4}	0.155

*where the $\Delta x_{\mathrm{L}} = 0.05$ m.

In accordance with Figure 4.12 and Table 4.2, the advantages of using DDT are clearly shown: (i) The ability of implementing wave absorption zone in linear region helps to prevent the wave reflection; (ii) With higher R, the wave is able to propagate with minimum distortions; (iii) The required CPU hours to achieve desire solution can be reduced up to 84% while using DDT with higher R for current CD nozzle condition.

4.2.2 Supersonic Flow Regime

4.2.2.1 Fully Nonlinear Simulations

The CD nozzle configuration shown in Figure 4.13 was used in this section. Ratio between convergent and divergent segments is 0.5 with half throat height, $h_t = 1$ m. The contours can be defined as follow,

$$y = \pm 2 \qquad \text{for} \quad |x| < 3 \,, \tag{4.15a}$$

$$y = \pm 1.5 \mp 0.5 \cos\left(\frac{\pi x}{x_i}\right) \qquad \text{for} \quad -3 \leqslant x \leqslant 3 \,, \tag{4.15b}$$

Fully nonlinear computational domain was first considered to perform mesh convergence analysis. For all mesh resolutions, since the existence of a curved shock

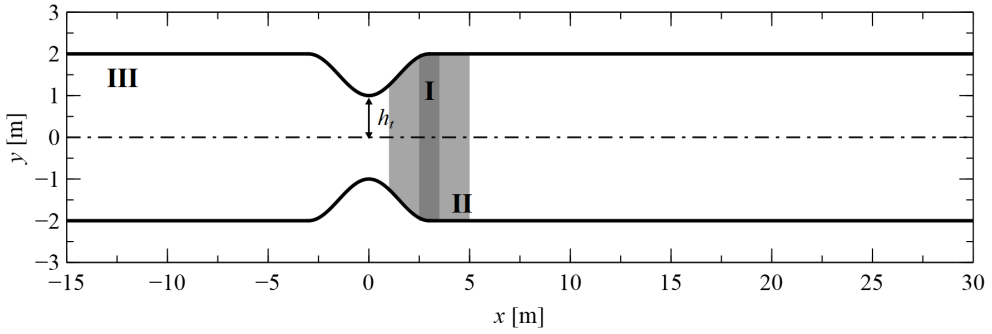

FIGURE 4.13: Computational domain of a converging-diverging nozzle simulation with half throat height, $h_t = 1$ m. Zone **I** indicates the estimated curved shock wave location.

wave is expected near the end of divergent segment, the cells between $2.5 \leqslant x \leqslant 3.5$ (zone **I** in Figure 4.13) were uniformly discretized with size of $\Delta x_{\text{NL}} = 0.001$ m to capture the shock motion correctly. The zone **II**, a 1.5 m extensions of zone **I**, was coarsen geometrically outward to locations, $x = 1$ m and $x = 5$ m until the cell size achieved $\Delta x_{\text{NL}} = 0.04,\ 0.02,$ and 0.01 m, respectively, for three different mesh resolution simulations. In the outermost zone **III**, the Δx_{NL} was uniformly discretized, with cell sizes of $\Delta x_{\text{NL}} = 0.04,\ 0.02,$ and 0.01 m towards both left and right boundaries. For transverse axis, the Δy_{NL} in all zones was discretized uniformly with cell widths of $\Delta y_{\text{NL}} = 0.04,\ 0.02,\ 0.01$ m for the three mesh resolutions, respectively.

At the left boundary, unity total pressure and temperature were applied. Meanwhile, adiabatic condition and back pressure, $p_b = 0.5$, at the right boundary were set such that the flow is choked and accelerated into supersonic flow regime in the divergent segment. Moreover, adiabatic and slip wall conditions were assumed in this problem. Again, inviscid and compressible flow was considered together with no body force and perfect ideal gas assumption.

First, a quasi-steady state was obtained at constant CFL $= 0.5$, $\gamma = 1.4$, and R $= 1/1.4$ before introducing an acoustic wave. The mean pressure and Mach number contours are presented in Figure 4.14, showing a curved shock wave located at approximately $x = 2.5$ m. Quantitatively, several fields on the symmetric axis of the nozzle are plotted in Figure 4.15. It clearly indicates that a shock wave is formed and divides the fields into different mean states. Inside the convergent-divergent segment, $\overline{p}$, $\overline{\rho}$ and $\overline{T}$ decrease to their corresponding minimum values before exiting the divergent segment where the shock wave is observed. The flow,

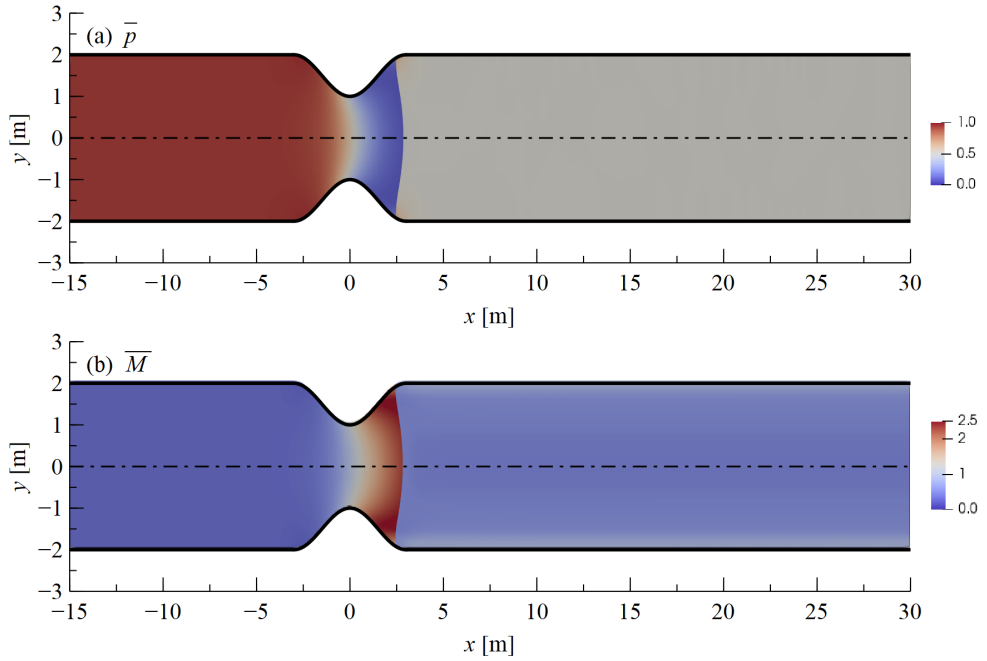

FIGURE 4.14: Mean (a) pressure, $\overline{p}$, and (b) Mach number, $\overline{M}$, contours from $\Delta x = 0.01$ m case show the discontinuity of the mean fields, indicating the presence of shock wave.

however, accelerates from subsonic to supersonic flow regime until the shock wave. The flow becomes subsonic again at the post-shock region. With the mean states stabilized, a Gaussian acoustic wave was then introduced into the domain as follows,

$$p(x, y, 0) = \overline{p}(x, y) + \epsilon G(x; -10, 0.5) \ , \tag{4.16a}$$

$$\mathbf{U}(x, y, 0) = \overline{\mathbf{U}}(x, y) + \frac{\epsilon}{1.4} G(x; -10, 0.5) \ , \tag{4.16b}$$

$$\rho(x, y, 0) = \overline{\rho}(x, y) + \epsilon G(x; -10, 0.5) \ . \tag{4.16c}$$

where $\epsilon = 10^{-2}$. All simulations were computed until $t = 30$ s with constant CFL $= 0.5$.

The interaction of a single acoustic wave with the curved shock wave inside a CD nozzle is presented in Figure 4.16 as a normalized wave for all three fully nonlinear cases. The multiple left-travelling waves marked as **C** can be attributed to the convergent-divergent segment, where generates reflection, similar to the subsonic simulation (see **B** in Figure 4.9). A hump marked as **D** could be attributed to converging-diverging effect but further investigation is needed to confirm. A significant reduction of the acoustic wave amplitude was observed from $t = 15$ s

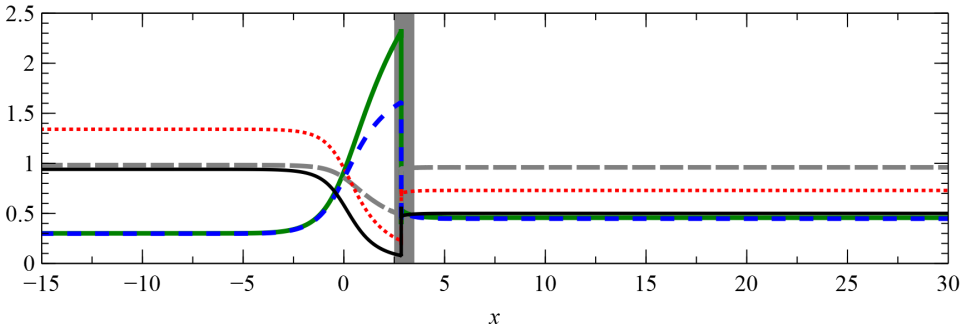

FIGURE 4.15: Steady states of the static pressure, $\overline{p}$ (black line), axial velocity, $\overline{\mathbf{U}}_x$ (blue short dashed-line), density, $\overline{\rho}$ (red dotted-line), temperature $\overline{T}$ (grey dashed-line) and Mach number, $\overline{M}$ (green thick line). Shaded area is the location of shock wave.

to 20 s. Since all three grid resolutions have the same observation, it is unlikely caused by a lack of resolution. Instead, the acoustic wave attenuation may be a result of superpositioning of different waves dispersed by the interaction with the shock.

4.2.2.2 Comparison of DDT and Fully Nonlinear Simulations

In this section, the linear region bounded between $x_{\mathrm{L}} \in \{[-15,-5],[10,30]\}$, whereas the nonlinear region is extended between $x_{\mathrm{NL}} \in [-5,10]$. The range of the nonlinear region was set based on several trials such that the lingering instability of the fields in the post-shock region has minimal influence towards the results in linear region. The linear region was uniformly discretized with $\Delta x_{\mathrm{L}} = \Delta y_{\mathrm{L}} = 0.04$ in the axial and transverse directions. Three overlap ratios, R, were considered, $R = 1,\ 2$ and 4, corresponding to the fully nonlinear cases with grid resolutions in zone **III**, $\Delta x_{\mathrm{NL}} = 0.04,\ 0.02$, and 0.01 m, respectively. Hence, the nonlinear region of each R simulation inherited the mesh setup from their corresponding fully nonlinear simulation. Likewise, the mean states of each cases from the fully nonlinear simulations in Section 4.2.2.1 were used to initialize the DDT simulations according to their R. DRP-7 point scheme [73], 9-point explicit filter scheme [76] and wave-absorption zone between $x_{\mathrm{L}} \in [-15,-12]$ and $[27,30]$ with 0.05 strength were applied to the linear region.

Figure 4.17 compares the DDT simulations with the fully nonlinear simulation that consists of the finest grid resolution ($\Delta x_{\mathrm{NL}} = 0.01$ m). All the features observed in the fully nonlinear case are reproduced in the DDT simulations, regardless of

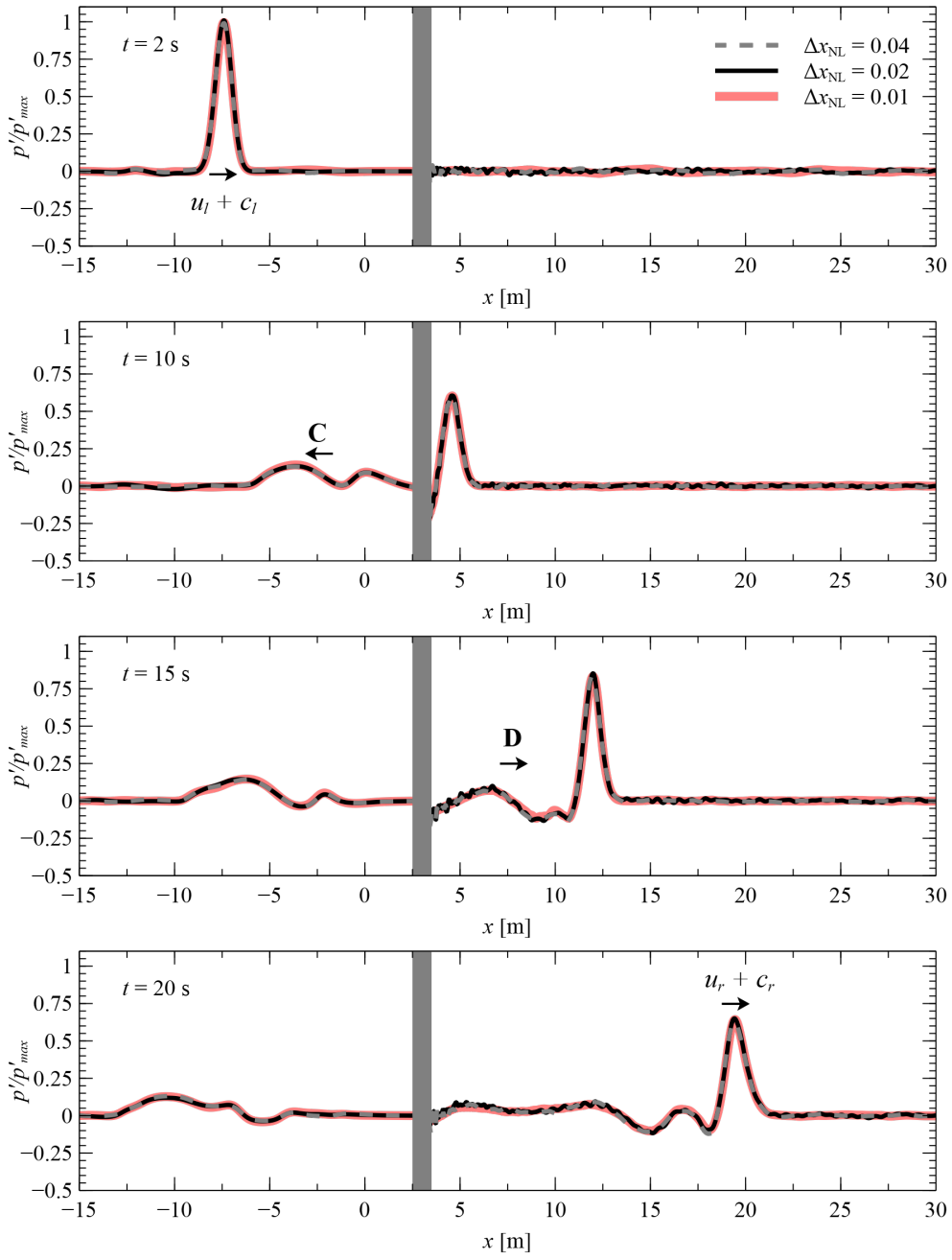

FIGURE 4.16: Interaction of acoustic wave with shock wave inside a CD nozzle with three resolutions. $\Delta x_{\text{NL}} = \{0.04, 0.02, 0.01\}$ m for zone **III** region on the fully nonlinear computational domain (see Figure 4.13). Note the shaded area is shock wave location, $p'_{max} = \epsilon$.

the value of R. A slight phase shift between DDT and fully nonlinear results is observed at $t = 20$ s. Among the DDT simulations, the normalized p' wave profile with $R = 4$ has slightly higher wave amplitude after interacting with shock wave. These discrepancies are attributed to the reduced range of fine nonlinear region, which decreases both dispersion and dissipation errors.

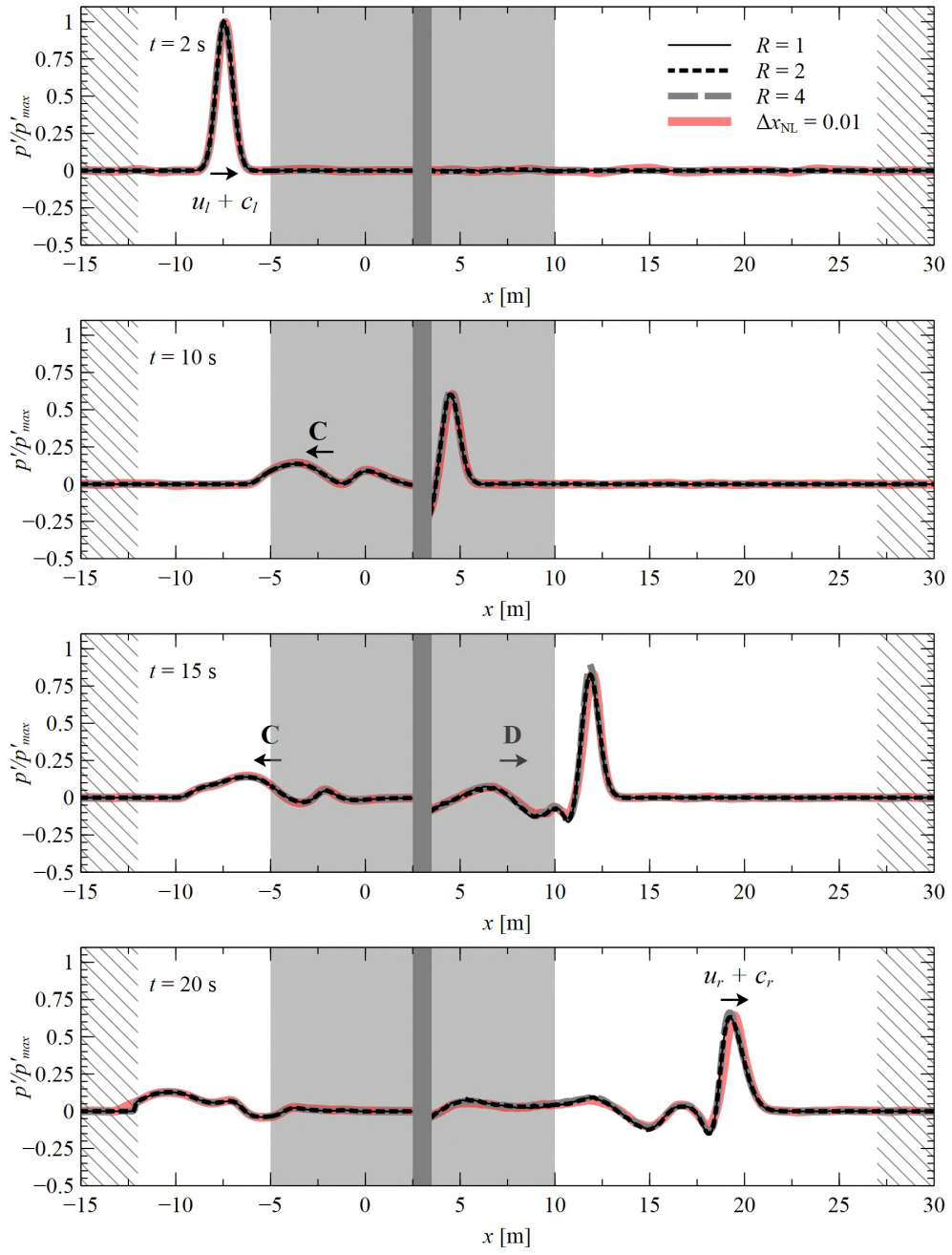

FIGURE 4.17: Comparison of the normalized p' at $t = \{2, 10, 15, 20\}$ s for DDT and converged fully nonlinear simulations. The nonlinear region for DDT is shaded grey, whereas sponge zone is shaded with lines. Shock wave location is in dark grey region, $p'_{max} = \epsilon$.

To quantify accuracy, the root-mean-square deviation was evaluated at $t = 20$ s with respect to fully nonlinear simulation ($\Delta x_{\text{NL}} = 0.01$ m), as presented in Table 4.3. Furthermore, the CPU hours consumption by each simulation cases are compared to examine the effectiveness of DDT. The DDT cases with $R = 1$ and 2

required higher computational hours due to the additional interpolation and mapping procedures at the interface between both linear and nonlinear regions. In short, based on Table 4.3, the advantage of DDT is obvious when R is high, as proven by the case with $R = 4$, which reduces approximately 51% of the computational hours and has relatively low RMSD value.

TABLE 4.3: Comparison of root-mean-square deviation and relative CPU hours for different computational types of various mesh resolution at $t = 20$ s using $\Delta x_{\mathrm{NL}} = 0.01$ m as reference case.

Simulation types	Resolution	RMSD	Relative CPU hours
Nonlinear	$\Delta x_{\mathrm{NL}} = 0.04$	1.6×10^{-4}	0.035
	$\Delta x_{\mathrm{NL}} = 0.02$	1.1×10^{-4}	0.072
	$\Delta x_{\mathrm{NL}} = 0.01$	–	1.0
DDT*	$R = 1$	2.1×10^{-4}	0.053
	$R = 2$	1.8×10^{-4}	0.099
	$R = 4$	1.5×10^{-4}	0.488

*where the $\Delta x_{\mathrm{L}} = 0.04$m.

4.3 External Flow: Acoustic Scattering Over Supercritical Airfoil

The purpose of this study case is to emulate the external flow scenario where engine noise scatter over the wing and how it interacts and propagates into the far-field as illustrated in Figure 4.18. An inviscid transonic flow over a 2D supercritical airfoil was studied to examine the feasibility of DDT for this external flow condition. The supercritical airfoil is designed to enhance the performance of airfoil in transonic flow regime by postponing the formation of transonic buffet flow field (a flow separation zone) due to the interaction of shock wave with turbulent boundary layer. Since inviscid flow was assumed, the transonic buffet flow will not be present, but the shock waves are still expected to form. Mesh independence study was done in fully nonlinear simulations using '*buoyantPimpleFoam*' without buoyancy effect, and then procedure (**b**) in Figure 3.2 was adopted to carry out the DDT simulations. Thereafter, the point and periodic acoustic sources were introduced to observe the interaction between both the acoustic and shock waves that have formed on the airfoil surface. The process was repeated for different Mach number flows.

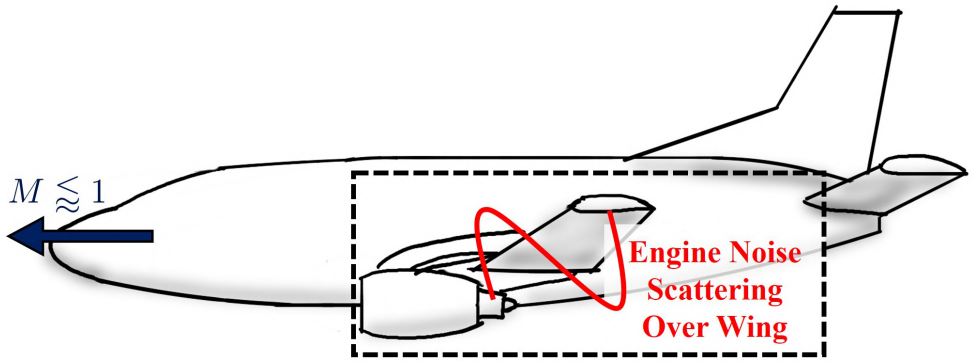

FIGURE 4.18: Scattering of engine noise over the wing while the aircraft traveling at transonic velocity.

4.3.1 Mesh Independence Study

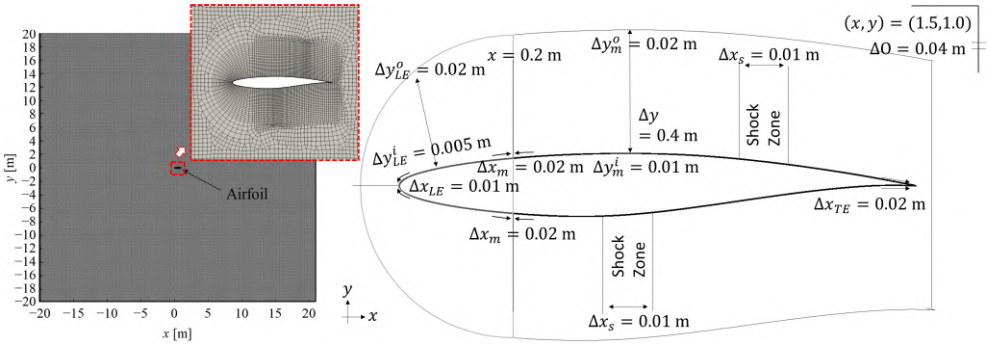

FIGURE 4.19: (Left) The 2D computational domain of airfoil RAE2822 with zoom-in view of coarsest mesh resolution around airfoil. (Right) Schematic diagram of type C-grid with various scales.

A supercritical airfoil, RAE2822, was chosen for this study so as to validate with the inviscid numerical results by [85]. A coarsest mesh was first constructed with domain size of 20 chord length extended from the airfoil for fully nonlinear simulation as shown on the left hand size of Figure 4.19. Type C-grid was adopted in near-field of the airfoil, as illustrated in zoom-in view, enclosed with red dashed box. Looking outward, combination of triangle and quad grids makes up the intermediate region up to two chord-length. In addition, the mesh in the far-field region beyond two chord-length from the airfoil was discretized uniformly in all directions, $\Delta x = \Delta y = 0.05$ m.

With zero angle of attack, $\alpha = 0$, freestream Mach number, $M_\infty = 0.775$, total pressure $p_\infty = 101.3$ kPa and total temperature, $T_\infty = 288$ K, both upper and lower airfoil surfaces are expected to form shock waves. Hence, the anticipated shock regions (upper: $0.7 < \Delta x/c < 0.8$; lower: $0.4 < \Delta x/c < 0.5$) are refined

to capture the shock structures properly. All the grid scaling around the airfoil are depicted on the right-hand side of Figure 4.19 for the coarsest mesh resolution (*gridV0*). Slip wall and adiabatic boundary conditions were implemented on the airfoil surface. An ideal perfect gas was assumed for the fluid properties. For all the simulations, constant CFL = 0.5, $\gamma = 1.4$, and gas constant, R = 287, were considered.

Upon reaching the steady state condition, the local Mach number on the airfoil surface (green line) is calculated and plotted in left graph of Figure 4.20 for comparison with benchmark inviscid numerical results (grey line) [85]. Even with the coarsest grid resolution, the results of fully nonlinear simulation show good agreement with the reference simulation. The locations of the shock waves agree well with the reference, through the slope of shock wave is less steep, suspecting more diffusion in the coarsest grid simulation have. Meanwhile, the local Mach number distributions over the airfoil surface are inline despite higher local Mach number observed near the leading edge ($x/c < 0.3$), as compared to the reference results.

With the grid setting shown in Figure 4.19, the refinement was performed by using double the number of grids on airfoil surface. For example, the shock zone cell size was reduced half from $\Delta x_s = 0.01$ to 0.005 m. The number of cells of upper and lower airfoil surfaces for *gridV0* is 73×71, *gridV1* is 140×137, and *gridV2* is 279×273. The far-field grid resolution was remain the same as 0.05 m for all refinements. From Figure 4.20, both local Mach number and pressure coefficient, C_p, plots show that the gradient of M and C_p at shock region get sharper when finer resolution is used. However, both M and C_p values were observed to have noticeable oscillations upstream of shock waves if the resolution is too small like in *gridV2*.

To eliminate the unwanted oscillations upstream of the shock waves and preserve the shock wave structures, a mesh, *gridV3* was constructed with the combination of near field mesh resolution of *gridV1* and shock region mesh resolution of *gridV2*. The results are compared in Figure 4.20 as a thin red line, containing sharp gradient of shock wave without the spurious oscillation, showing a fully converged nonlinear solution.

The mean pressure contour over the airfoil and local Mach number contour lines are illustrated in Figure 4.21. The local Mach number lines indicate the flow

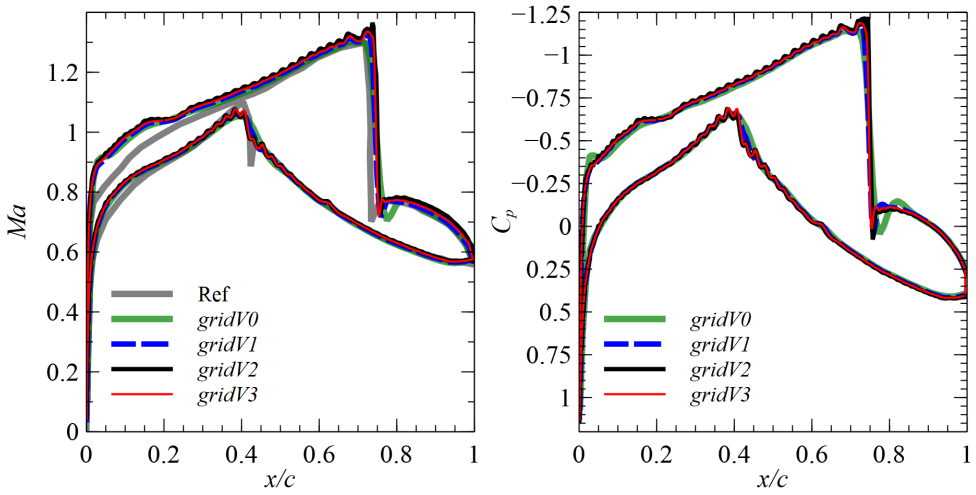

FIGURE 4.20: (Left) Comparison of local Mach number distribution on the airfoil surface between fully nonlinear simulations and numerical solution reference (grey line). (Right) Comparison of pressure coefficient among the fully nonlinear simulations with different grid resolutions.

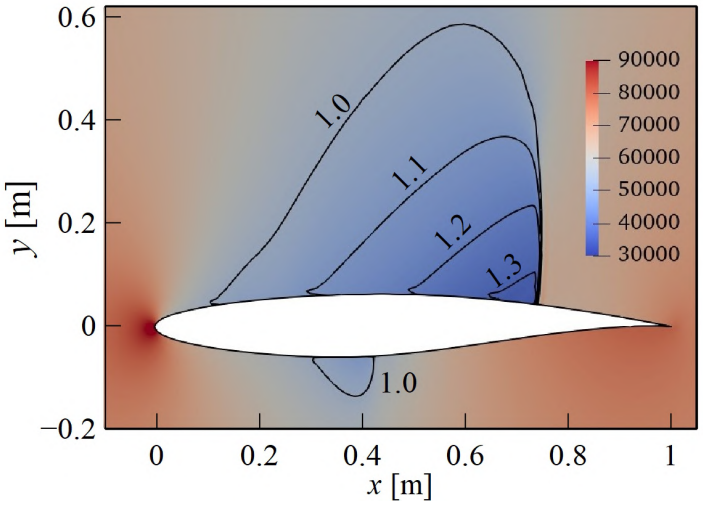

FIGURE 4.21: Mean pressure contour over RAE2822 at freestream Mach number, $M_\infty = 0.775$ and local Mach number contour lines.

acceleration around the airfoil from subsonic to supersonic, followed by a large deceleration at the shock wave that sharply slow the flow back to the subsonic regime.

4.3.2 Acoustic Scattering in Fully Nonlinear and DDT Simulations

The DDT simulations discussed in this section applied same grid resolution used in fully nonlinear simulation (*gridV3*) for nonlinear region with overlap ratio, $R = 1$, unless mentions exclusively. Whereas, the linear region in DDT computational domain was discretized uniformly ($\Delta x = \Delta y = 0.05$ m), solved by 7-point DRP scheme [73] and 9-point explicit filter scheme [76] with filter strength of 0.05 to eliminate the short waves. The strength and size of sponge zone used in DDT simulation were fixed at 0.01 and 3 m width, respectively.

The optimum nonlinear domain size was obtained by examining three DDT simulations with nonlinear domain size of five, seven and nine chord lengths away from the airfoil. The results show no difference among three nonlinear domain sizes regardless of the time needed for both regions to achieve steady state condition before introducing acoustic waves, as needed for procedure (**b**) in Figure 3.2. It was observed that the larger the nonlinear domain size, the longer the simulation time needed to achieve steady state in DDT simulation before introducing acoustic waves. Nonetheless, nonlinear domain must be in adequate size in order to preserve the non-linearity such as the formation of shock wave. Hence, nonlinear domain size of five chord length away from airfoil was chosen as depicted in Figure 4.22 on the left.

Upon deciding the final mesh resolution and nonlinear domain size, two additional simulations with freestream Mach number, $M_\infty = 0.4$ and 0.735 were conducted until achieving the steady state solutions as illustrated on the right hand side of Figure 4.22 as mean pressure fields and Mach number contour lines. In the cases of $M_\infty = 0.735$ and 0.775, shock waves are generated on the upper surfaces of the airfoil for both cases and mild shock wave on lower airfoil surface for $M_\infty = 0.775$ case. With that, two types of artificial acoustic sources, point and periodic acoustic sources were initialed in linear region of DDT and converged fully nonlinear simulations (*gridV3* mesh resolution) for all three freestream Mach number cases.

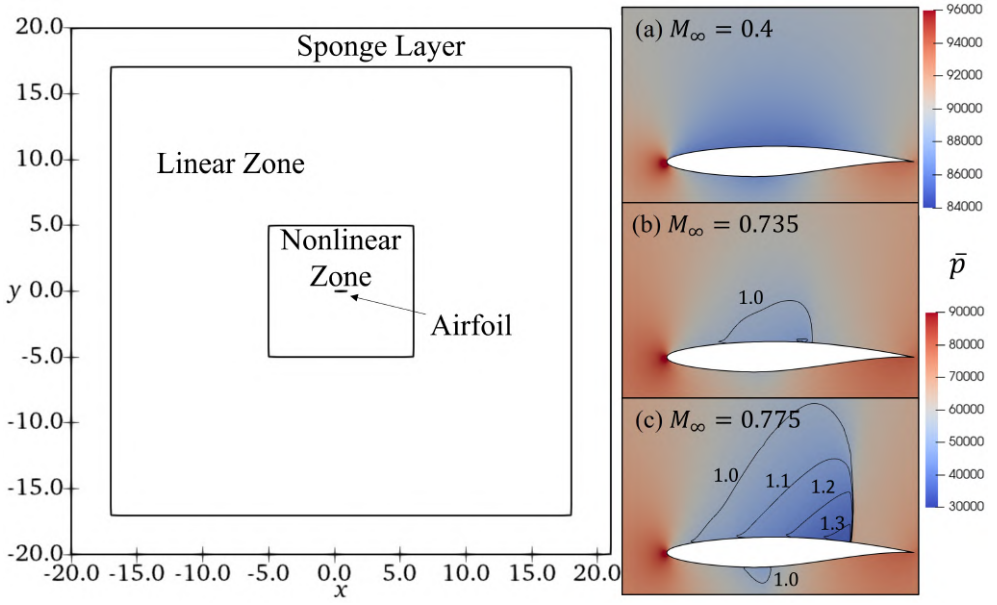

FIGURE 4.22: (Left) The optimized DDT computational domain consists of linear, nonlinear and sponge zones. (Right) Mach number contour lines and mean pressure fields for freestream Mach number flow, (a) $M_\infty = 0.4$, (b) $M_\infty = 0.735$ and (c) $M_\infty = 0.775$

4.3.2.1 Point Acoustic Sources

First, the point acoustic source at $\boldsymbol{x}_0 = (-11, 0)$ was initialized in both fully nonlinear and DDT simulations as follows,

$$p'(\boldsymbol{x}, 0) = \epsilon H(\boldsymbol{x}; \boldsymbol{x}_0, \sigma) \,, \tag{4.17a}$$

$$\rho'(\boldsymbol{x}, 0) = \frac{\epsilon}{\bar{c}^2} H(\boldsymbol{x}; \boldsymbol{x}_0, \sigma) \,, \tag{4.17b}$$

where $\epsilon = 5000$, $\sigma = 0.2$, and $\bar{c} = \sqrt{\gamma \mathrm{R} \overline{\overline{T}}}$ is the mean acoustic speed based on mean temperature, $\overline{T}$. Constant CFL number of 0.35 was used for this acoustic wave scattering simulation.

The far-field fully nonlinear simulation results at $M_\infty = 0.775$ are shown as pressure perturbation, p', contours in Figure 4.23. Note that, the pressure perturbations are depicted as red/blue lines which represent ± 50 Pa, whereas black/grey lines represent ± 20 Pa. The p' contours are captured at (left) $t = 0.016$ s and (right) $t = 0.037$ s, showing pre-scattering and post-scattering, respectively. Moreover, the irregular p' contour lines in the far-field regions can be attributed to the numerical errors generated in the nonlinear domain, which solves at the background pressure level, which is at $\mathcal{O}(10^4)$ about 90 kPa, at least three time higher than the

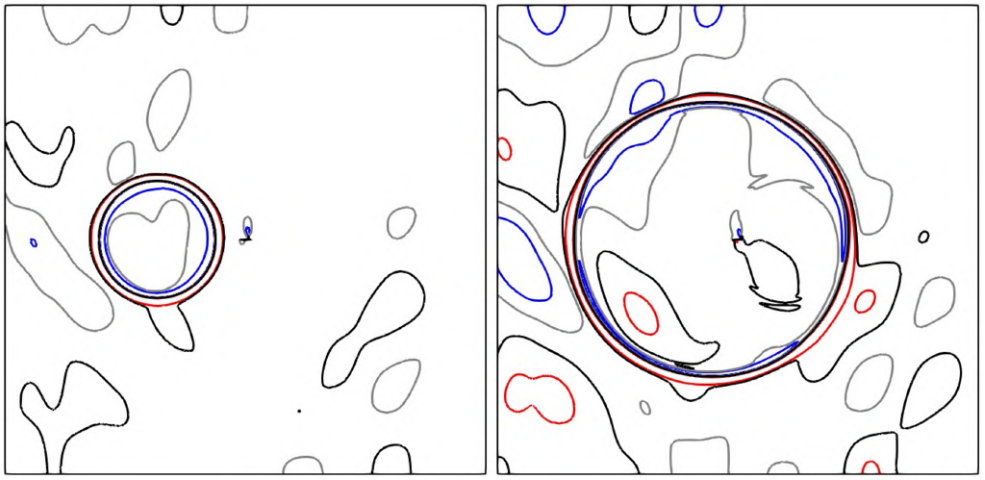

FIGURE 4.23: Acoustic wave, initialized at $\boldsymbol{x}_0 = (-11, 0)$, scattering over supercritical airfoil for fully nonlinear simulation of $M_\infty = 0.775$ at (left) $t = 0.016$s and (right) $t = 0.037$ s. The pressure perturbation contours were illustrated as red/blue lines which represent ± 50 Pa, whereas black/grey lines represent ± 20 Pa.

perturbation order shown in Figure 4.23. This numerical noise can be eradicated if DDT is applied so that the linear solver, which solves at the perturbation level, can be used to take care of these small perturbations.

The far-field DDT results are presented in Figure 4.24 for $M_\infty = 0.775$ at (left top) $t = 0.016$ s, (right top) $t = 0.037$ s, (left bottom) $t = 0.05$ s, and (right bottom) $t = 0.06$ s. First row p' contours in Figure 4.24 are corresponding to Figure 4.23, showing clean far-field regions with the help of linear solver. The left top corner plot shows slight distortion of the acoustic wave when entering the nonlinear region due to dissipation. Reconstruction of the acoustic wave from nonlinear to linear region is shown at right top corner plot. The right bottom plot shows the outgoing wave is absorbed by the sponge zone (outer box) effectively. Similar far-field behaviors were observed for $M_\infty = 0.40$ and $M_\infty = 0.735$ DDT simulations.

In the near-field, Figure 4.25 presents the point acoustic source interactions with airfoil under three different freestream Mach number flow, each contour plot size is equivalent to the red dotted-box in Figure 4.22. For subsonic flow (left column), $M_\infty = 0.40$, a negative amplitude of acoustic wave, labeled as **A**, was observed to travel in opposite direction of main acoustic wave due to the scattering with the airfoil. Similar scattering waves (**A**) are generated for (middle column) $M_\infty = 0.735$ and (right column) 0.775 cases with stronger strength indicated by narrow beam-shaped black contour lines (10 Pa). Two unique features, labeled as **B** and **C**

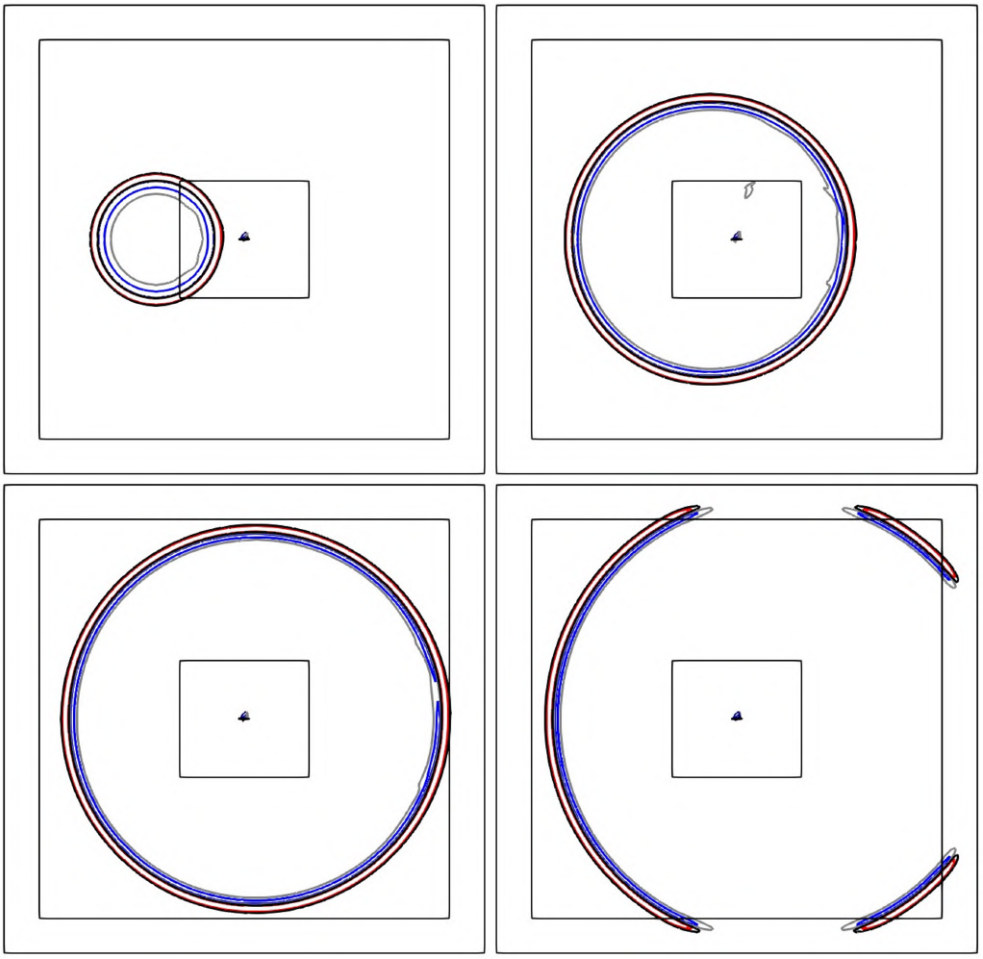

FIGURE 4.24: Illustration of the wave propagation in far-field for case of $M_\infty = 0.775$. Inner box is the nonlinear region, outer box is the sponge zone, and the region bounded between inner and outer box is the linear region. Red/blue lines indicate ± 50 Pa, whereas black/grey lines represent ± 20 Pa.

in Figure 4.25, are only observed for the cases involved shock waves. Hence, the presence of the shock waves is believed to be responsible for the generation of small secondary waves, similar to the study in [6] where secondary wave is created at the downstream of a normal shock wave while interacting with acoustic/entropy wave.

Same strength point acoustic source but different location was initialized at $\boldsymbol{x}_0 = (-11, -11)$ to investigate the scattering of acoustic wave in different direction toward airfoil and shock wave. The far-field p' contours of fully nonlinear simulation are illustrated in Figure 4.26 at (left) $t = 0.03$ s and (right) $t = 0.05$ s, representing pre- and post-scattering states, respectively. Reflected wave was observed at the bottom boundary. Similar to Figure 4.23, the numerical noise in far-field was observed, DDT is applied to eliminate this issue.

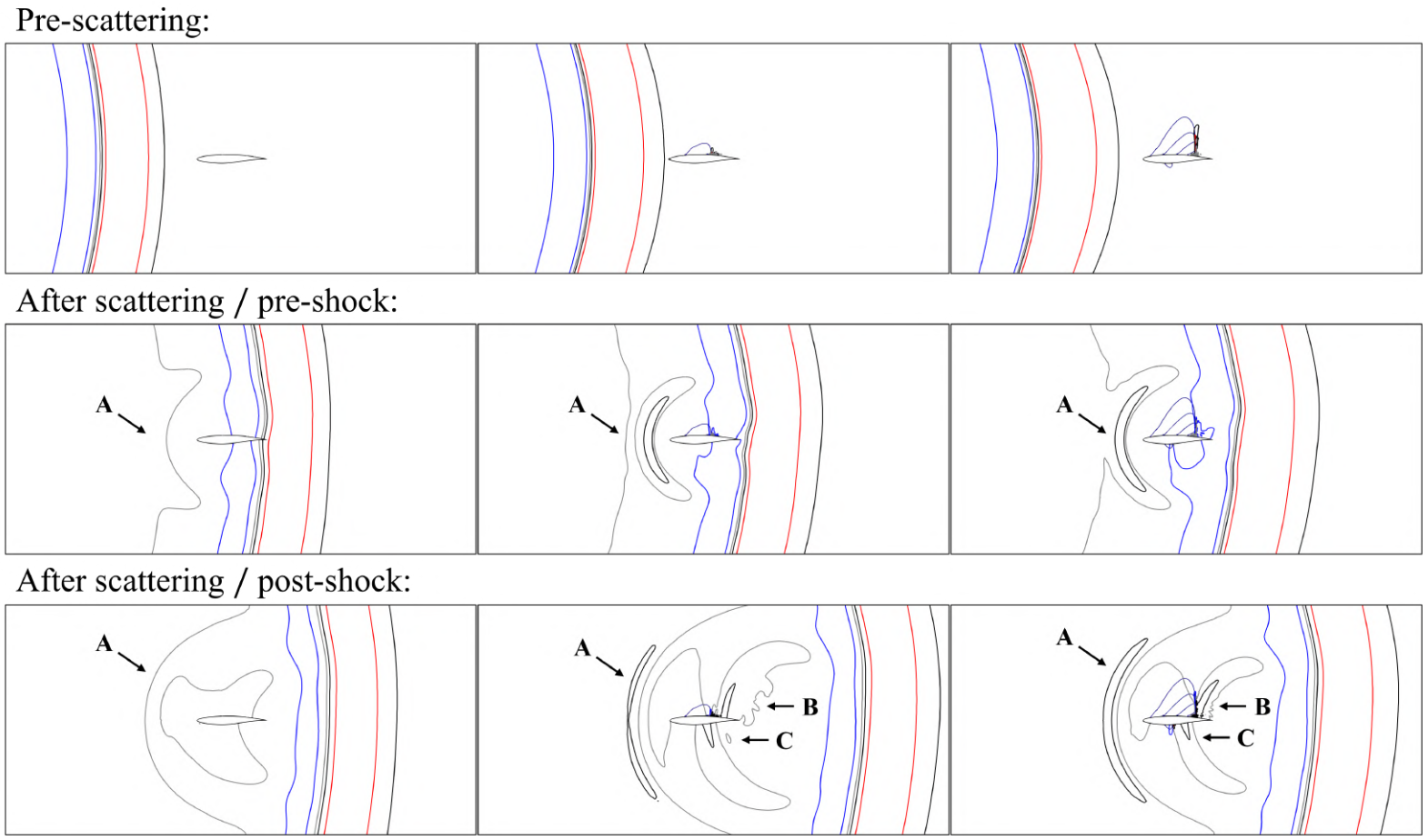

FIGURE 4.25: The acoustic scattering over airfoil RAE2822 under different freestream Mach number: (left column) $M_\infty = 0.40$, (middle column) $M_\infty = 0.735$ and (right column) $M_\infty = 0.775$. Red/blue lines indicate ± 50 Pa, whereas black/grey lines represent ± 10 Pa.

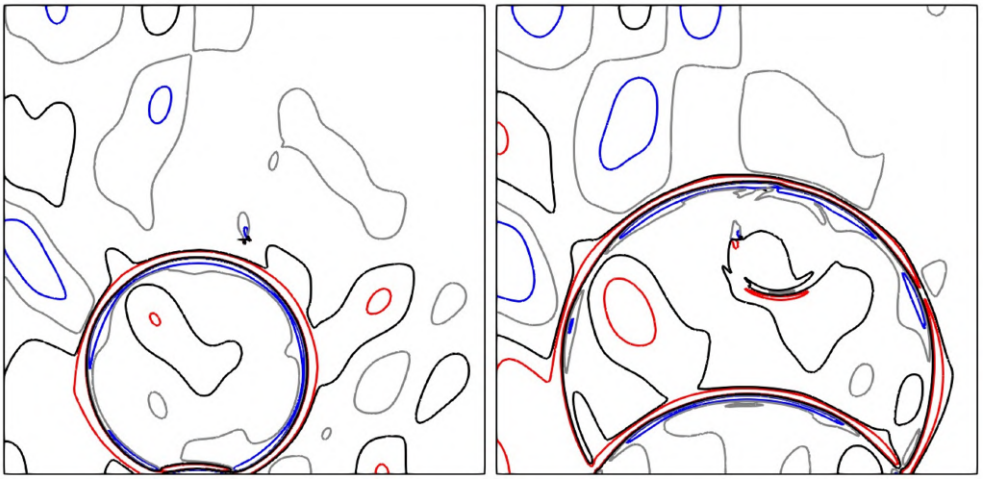

FIGURE 4.26: Acoustic wave, introduced at $\boldsymbol{x}_0 = (-11, -11)$, scattering over supercritical airfoil for fully nonlinear simulation of $M_\infty = 0.775$ at (left) $t = 0.03$s and (right) $t = 0.05$s. The pressure perturbation contours were shown as red/blue lines, which represent ± 50 Pa, whereas black/grey lines represent ± 20 Pa.

The DDT simulation of $M_\infty = 0.775$ results are demonstrated in Figure 4.27 as sequence of p' propagation contours in far-field region. The top row p' contours are drawn at (left) $t = 0.03$s and (right) $t = 0.05$s, have clearly shown a clean far-field region as compared to corresponding fully nonlinear simulation contours (Figure 4.26). The scattering (**A**) and secondary (**B**) waves propagate into the linear region, which are not observed in Figure 4.24. This is caused by the incident angle of the wave with respect to the airfoil such that the acoustic wave encounters a larger surface area of airfoil, as compared to Figure 4.24, and eventually resulting in diffractive scattering.

Moreover, there are spurious reflection waves, indicated as **D** and **E**, due to the propagation of the acoustic wave into the interfaces between linear and nonlinear regions and between linear region and sponge zone, respectively. The spurious reflection wave **E** in Figure 4.27 can be eradicated easily by increasing the sponge zone size. Increasing overlap ratio, R, can help to minimize the occurrence of spurious reflection waves, **D**.

Figure 4.28 presents sequence of the interaction between acoustic wave and airfoil with or without shock waves depend on the freestream Mach number, M_∞. Compared to Figure 4.25, the scattering waves (**A**) were observed for all cases right after the main acoustic wave propagated through the airfoil. Likewise, the secondary acoustic waves (**B**) are seen to be lagging behind the main acoustic wave due to

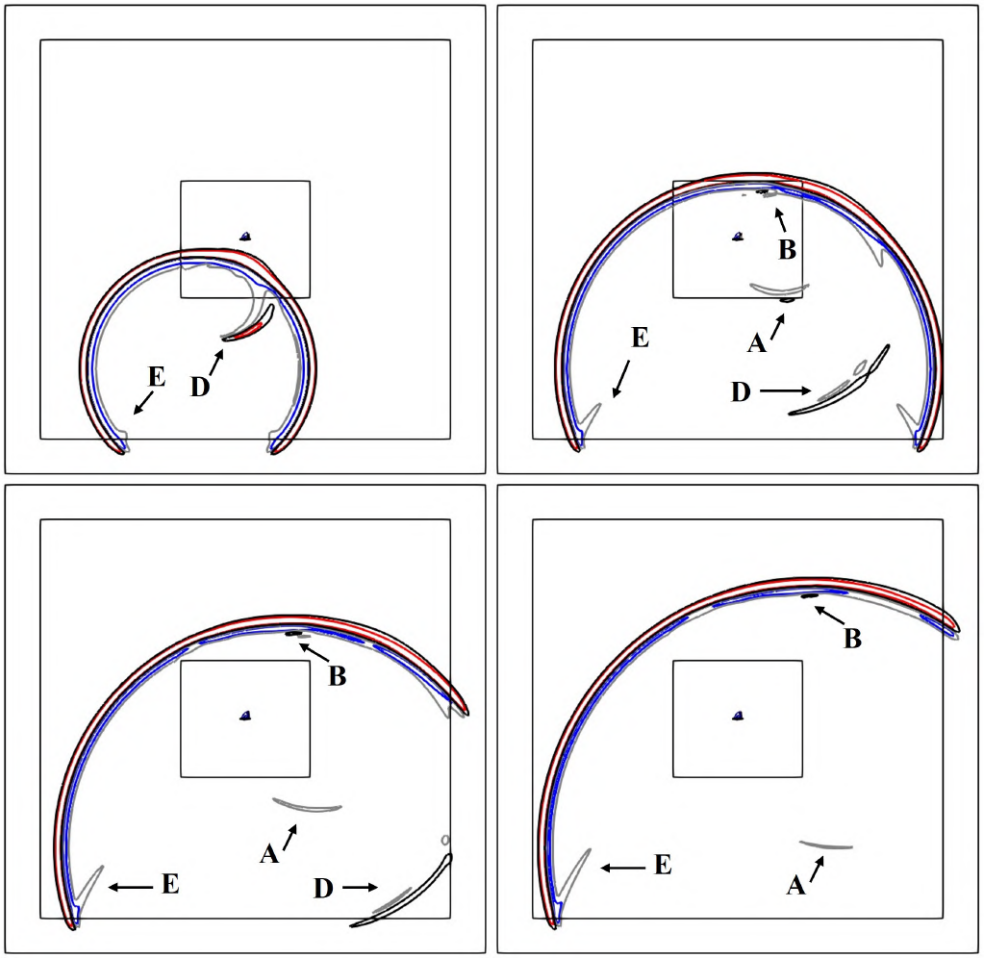

FIGURE 4.27: Illustration of the wave propagation in far-field for case of $M_\infty = 0.775$ at (left top) $t = 0.03$s, (right top) $t = 0.05$s, (left bottom) $t = 0.06$s, and (right bottom) $t = 0.07$s. Red/blue lines indicate ± 50 Pa, whereas black/grey lines represent ± 20 Pa.

the interaction between main acoustic wave and the shock wave. The secondary acoustic wave located at lower airfoil surface, which appeared in Figure 4.25 as **C**, is not be able to identify in Figure 4.28.

The fully nonlinear simulation (right bottom of Figure 4.29), corresponding to $R = 2$ DDT case, was conducted with uniform cell size of $\Delta x_{\text{NL}} = 0.025$ m in the far-field as a benchmark fully nonlinear numerical solution. The results of DDT with $R = 1, 2$ and 5 and benchmark fully nonlinear simultions are shown as normalized p' contours at $t = 0.03$ s in Figure 4.29. The results then show the spurious reflecting wave **D** is not detectable but the reflections from the domain boundary and the numerical noise in the far-field are clearly observed, which are not observed in DDT simulations. By refining the nonlinear cell resolution and

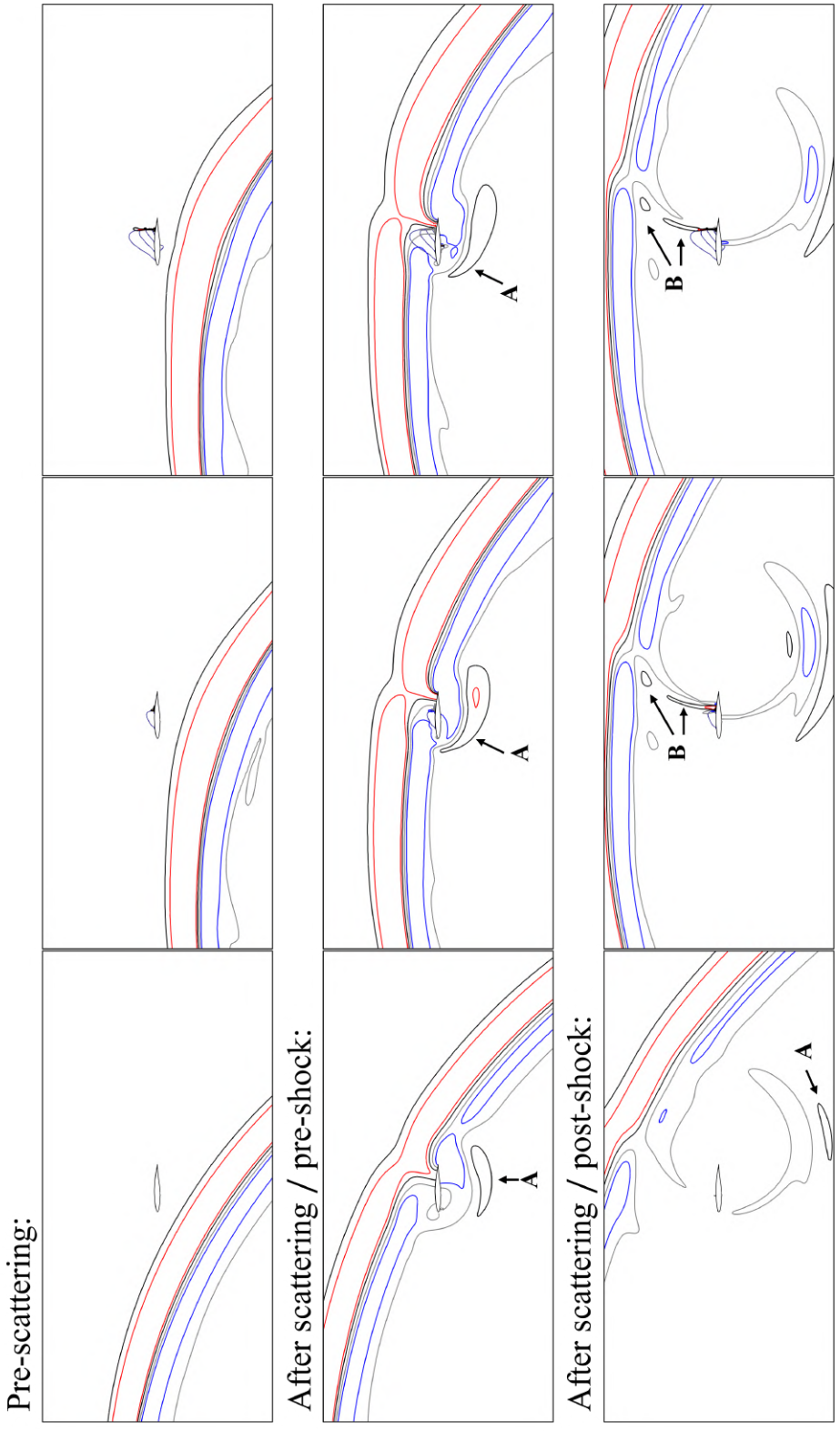

FIGURE 4.28: The acoustic scattering over airfoil RAE2822 under different freestream Mach number: $M_\infty = 0.40$ (left column), $M_\infty = 0.735$ (middle column) and $M_\infty = 0.775$ (right column).

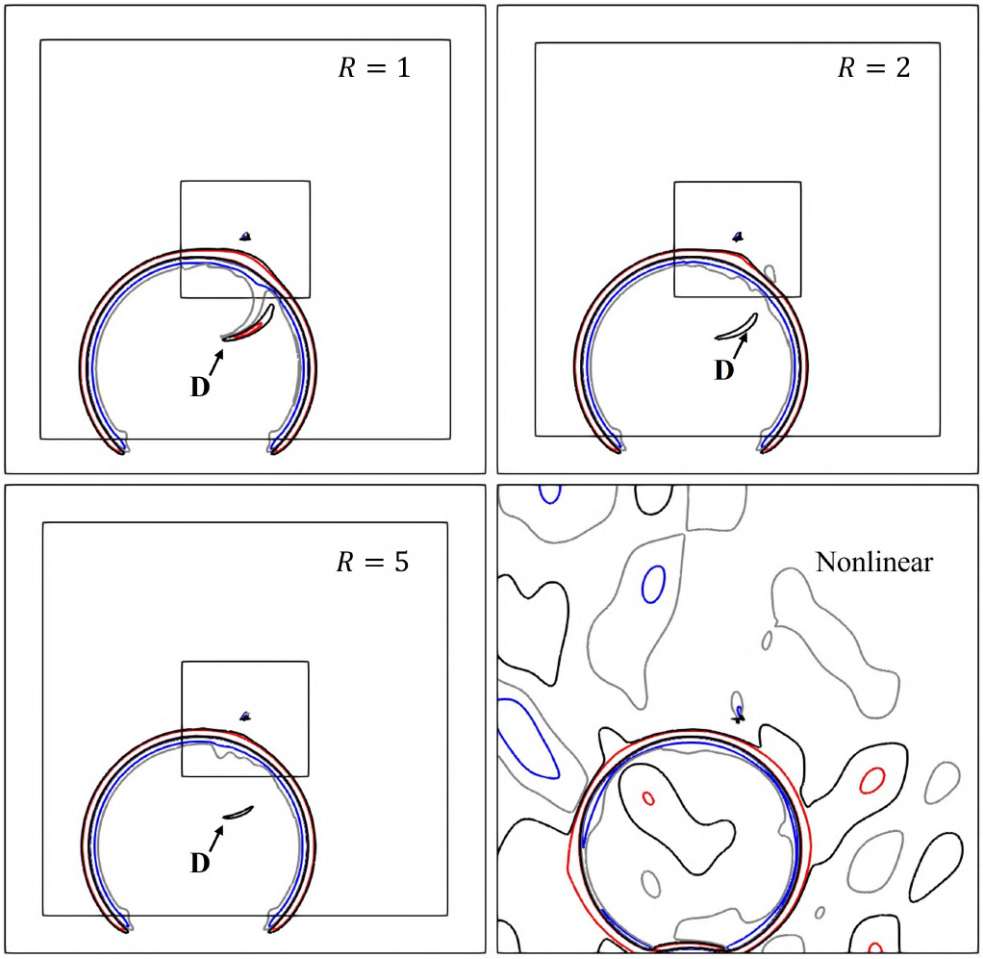

FIGURE 4.29: The spurious reflection wave (**D**) is reduced when overlap ratio, R is increased. Red/blue lines indicate ±50 Pa, whereas black/grey lines represent ±20 Pa.

hence increasing the overlap ratio R, the spurious reflection wave **D** is reduced or even eliminated as proven in Figure 4.29. For example, the DDT simulation with (left bottom plot) $R = 5$ gives minimal reflection waves and clean far-field region as compared to (right bottom plot) fully nonlinear simulation. Thus, the technique shows higher overlap ratio ($R \geqslant 5$) yields better accuracy and its advantage of implementing the sponge zone, which helps to eliminate the spurious/reflection waves. In addition, the computational cost is greatly reduced while maintaining the adequate accuracy. For instance, the total CPU times incurred by DDT cases with $R = 2$ and 5 DDT are only 10.5% and 34.4% of the fully nonlinear simulation, respectively, showing the computational cost-saving advantage of using domain decomposition technique.

4.3.2.2 Periodic Acoustic Sources

A periodic acoustic wave is considered in this section in conjunction with the important finding from the previous point acoustic source study, where overlap ratio $R = 5$ yields best accuracy. Thus, $R = 5$ setting was implemented in all three freestream Mach number DDT simulations with initialization of 2D periodic acoustic source in linear region as such,

$$p'(\boldsymbol{x}, t) = \epsilon F(\boldsymbol{x}, t; \boldsymbol{x}_0, \sigma, f) \ , \tag{4.18a}$$

$$\rho'(\boldsymbol{x}, t) = \frac{\epsilon}{\bar{c}^2} F(\boldsymbol{x}, t; \boldsymbol{x}_0, \sigma, f) \ , \tag{4.18b}$$

where $\epsilon = 100$, $\sigma = 0.1$, and $f = 500$ Hz. The resultant p'_{max} used to normalize the pressure perturbation is set such that the interested features are preserved with 100 Pa, 1000 Pa, and 1000 Pa, for $M_\infty = 0.4$, 0.735, and 0.775, respectively. The normalized pressure perturbation color contour are shown in Figure 4.30 for (left) far- and (right) near-fields regions. The red/blue color ranges within ± 1 of normalized pressure perturbation.

In the far-field region, as shown in left column of Figure 4.30, the periodic wave propagates in different ways, whereby the wave can propagate to the left side of the source for a subsonic background flow. This is known as the Doppler effect where the wavelength at the left-hand side of the acoustic source is shorter than that on the right-hand side.

Besides, both far- and near-fields normalized pressure perturbation contours in Figure 4.30 show the wave interference wavefront at the right-hand side of acoustic source ($x > -11$ m), most noticeable in the transonic cases. The interaction between the incoming and scattering waves induces wave interference at the leading edge of airfoil as labeled by '**A**' in the near-field regions. The interference get stronger with the strength of scattering waves, resulting in the significant distortions of wavefront at the downstream of airfoil for the transonic cases.

Additionally, the pressure perturbation at the post-shock regions, labeled as '**B**' in Figure 4.30, will amplify due to the interaction of acoustic waves with shocks, akin to the secondary waves generation observed in Figure 4.25. These multiple secondary waves will not only intensify the lift coefficient fluctuation, c'_l, but also shift its mean, $\overline{c_l}$, as shown in Figure 4.31 on the left plot. Approximately 0.8%

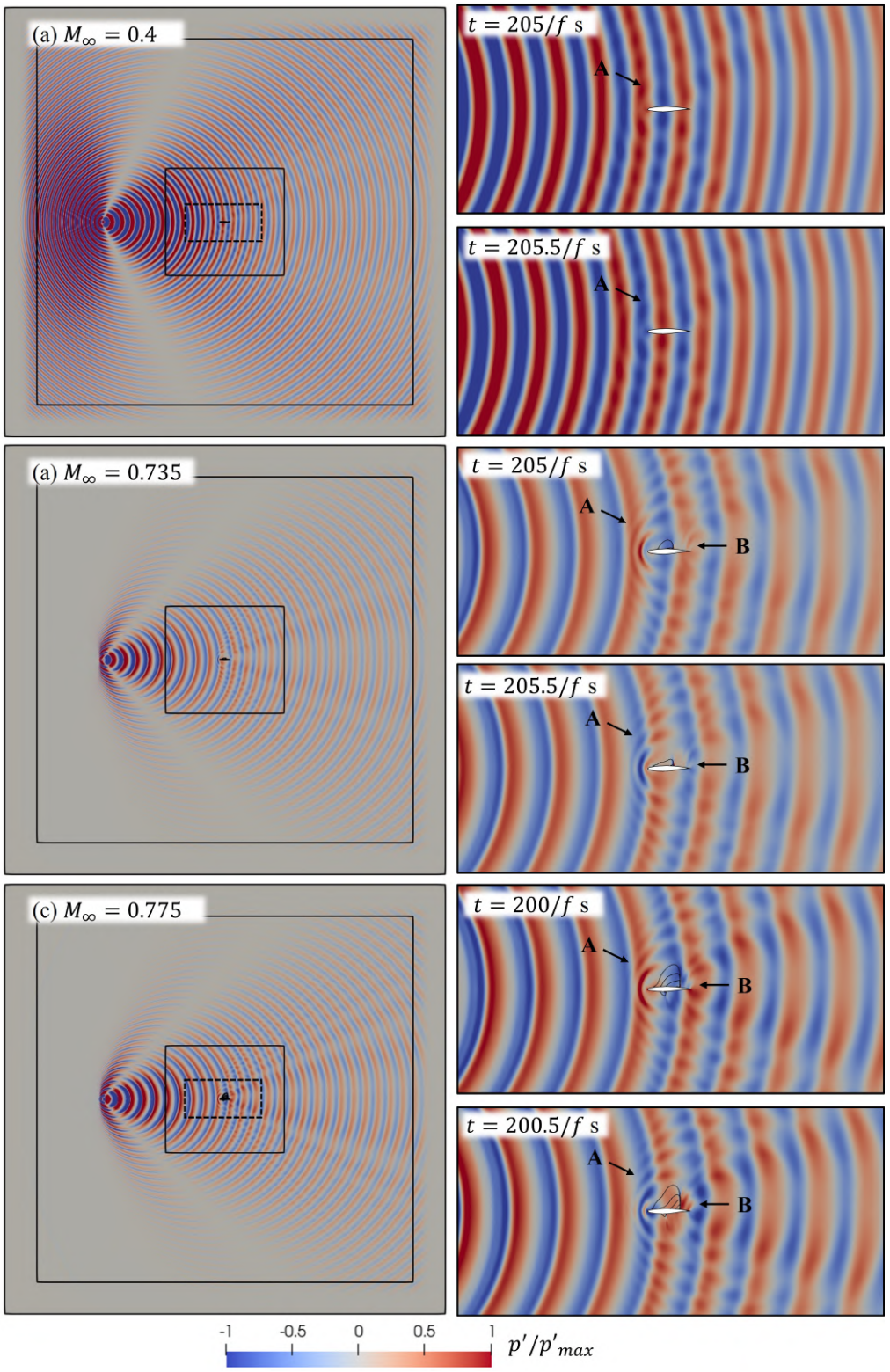

FIGURE 4.30: (Left) Illustration of the Doppler effect in the far-field for (a) $M_\infty = 0.4$, (b) $M_\infty = 0.735$, (c) $M_\infty = 0.775$. (Right) Two corresponding near-field normalized pressure perturbation contours (enclosed location by black dotted-box) show repetitive behavior and wave interference.

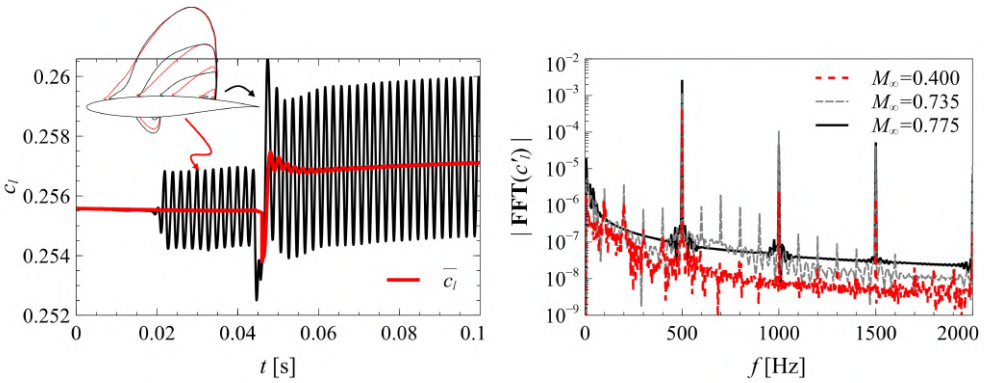

FIGURE 4.31: (Left) Graph of the lift coefficient, c_l, over the airfoil RAE2822 against time, t, at $M_\infty = 0.775$ shows the changes of $\overline{c_l}$ at $t = 0.05$ s. Red and black M contour lines are plotted at 0.03 s and 0.06 s, respectively. (Right) The fast Fourier transform (FFT) of the lift coefficient perturbation, c_l' for 0.3 s $< t <$ 0.5 s.

increment of $\overline{c_l}$ at $t = 0.045$s for $M_\infty = 0.775$ case is observed. Meanwhile, the M contours on the left top corner of Figure 4.31 show the movement of shock waves. Similar trend is observed in $M_\infty = 0.735$ case but not in $M_\infty = 0.40$ case, as expected.

Furthermore, the c_l of all cases between 0.3 s $< t <$ 0.5 s (quasi-steady state) was processed with fast Fourier transform (FFT) analysis to examine the underlying resonance frequencies. The FFT results are shown on right plot of Figure 4.31. All cases exhibit a dominant frequency of 500 Hz, which is related to the frequency of the periodic acoustic source, despite the difference in amplitude. Overall, the DDT has shown its superiority in dealing typical wave interactions, such as with solid body and fluid/shock, and providing accurate wave propagation solutions which fully nonlinear solution tends to having numerical noise and excessive numerical diffusion at the far-fields.

4.4 Non Isothermal Viscous Flow

In Sections 4.2 and 4.3, the feasibility of solving 2D inviscid compressible flow by domain decomposition technique has been demonstrated. Next, the approach is extended to problem involving heated viscous flow in the nonlinear zone, as a preceding research for development of thermoacoustic DDT simulations. The nonlinear domain is solved by '*buoyantPimpleFoam*' without buoyancy effect, whereas

linearized NS (LNS) is solved in linear region for propagation of small perturbation or acoustic wave initialization. Procedure (**a**), as mentioned in Chapter 3, was chosen in this type of problem. The statistical mean states were first collected in fully nonlinear simulation. Thereafter the mean field states were mapped into DDT simulation and then follow by introducing point and periodic acoustic sources in linear region to study the thermoacoustic interaction.

4.4.1 Configurations

TABLE 4.4: Configurations of computational domain of different types of simulations.

Computational type	Fully nonlinear	DDT
Domain size [m]	$-1.5 < x_{\mathrm{NL}} < 1.5$	$-1.5 < x_{\mathrm{L}} < 1.5$, $-0.5 < x_{\mathrm{NL}} < 0.5$
	$-2.5 < y_{\mathrm{NL}} < 1.0$	$-2.5 < y_{\mathrm{L}} < 1.0$, $-0.5 < y_{\mathrm{NL}} < 1.0$
Δx_{NL} or Δy_{NL}	refer Figure 4.32	
Δx_{L} or Δy_{L}	-	0.005 m

A heater with diameter, $D = 0.04$ m and constant wall temperature, $T_W = 350$ K is placed in a laminar flow field moving vertically upwards as shown in Figure 4.32. Ambient velocity, temperature and pressure are $v_\infty = 0.03$ m/s, $T_\infty = 300$ K and $p_\infty = 1 \times 10^5$ Pa, respectively. Ideal gas law is applied and the dynamics viscosity of air, $\mu = 1.82 \times 10^{-5}$. The CFL is maintained at 0.3 for collecting statistical mean state. The computational domain size for DDT simulation is shown in Figure 4.32, contains 0.43M of cells. Note for nonlinear region is extended to sponge zone for fully nonlinear simulation as summarized in Table 4.4. In linear region, DRP-7 point scheme [73] was applied and 9-point explicit filter scheme [76] was used to reduce the short waves. The strength of sponge zone was set to be 0.005 to completely absorb the outgoing waves.

To minimize the dissipation in fully nonlinear region for both types of simulations, time step is vital and hence a time convergence study for a plane wave under current grid resolution was done. It found that at $\Delta t = 1 \times 10^{-6}$ s, corresponds to CFL = 0.07, the dissipation rate is low with reasonable computational cost. With that, the time step of $\Delta t = 1 \times 10^{-6}$ s was used for both types of simulations.

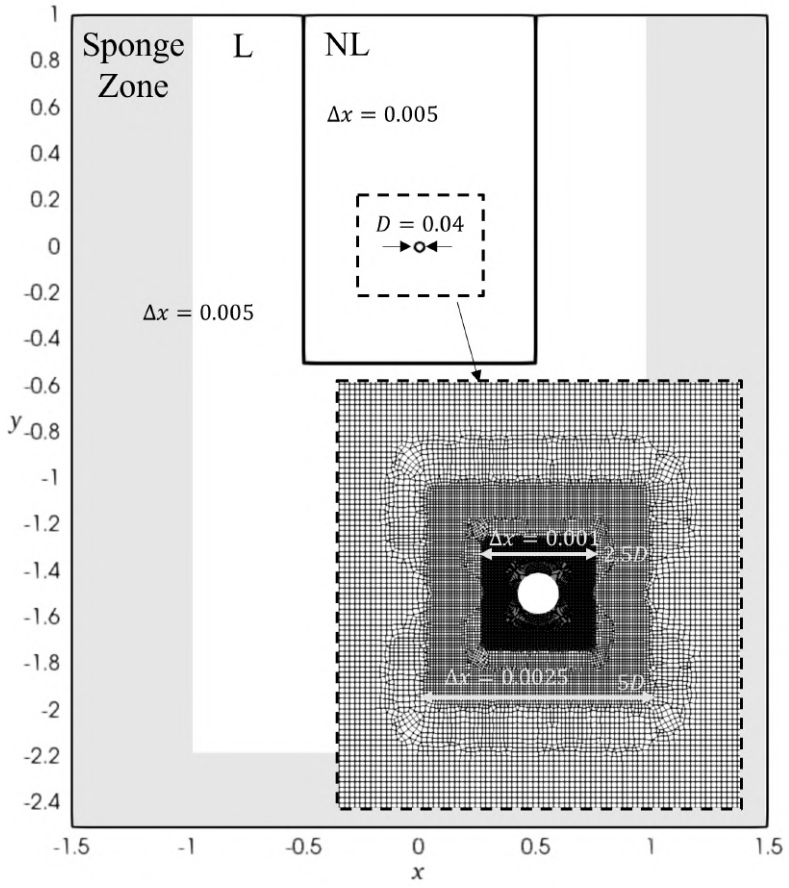

FIGURE 4.32: The domain decomposition computational domain: (**L**) linear region, (**NL**) nonlinear region and shaded sponge zone. Dotted box indicates the mesh resolutions at the near-field of the cylinder heater. All measurements are in meter [m].

4.4.2 Comparison of Fully Nonlinear And DDT Simulations

After the transient phase ($t = 120$ s), the statistical means for the primitive variables were collected up to $t = 160$ s. The results are shown as grayscale contour in Figure 4.33 for instantaneous (a) velocity and (c) density as well as their corresponding mean fields. Vortex shedding, an oscillating flow feature when a fluid flows past a bluff body (cylinder heater here), is observed in both instantaneous velocity and density fields. Vortices are formed periodically at the downstream of the heater, forming a Von Kármán vortex street at frequency of 0.2 Hz. Heat release by heater forms less dense hot air and is also convected downstream at the same frequency of the flow, as shown in the density variance in Figure 4.33 (c)

and (d). Quantitatively, the vortex shedding is illustrated in Figure 4.34 along the symmetric axis.

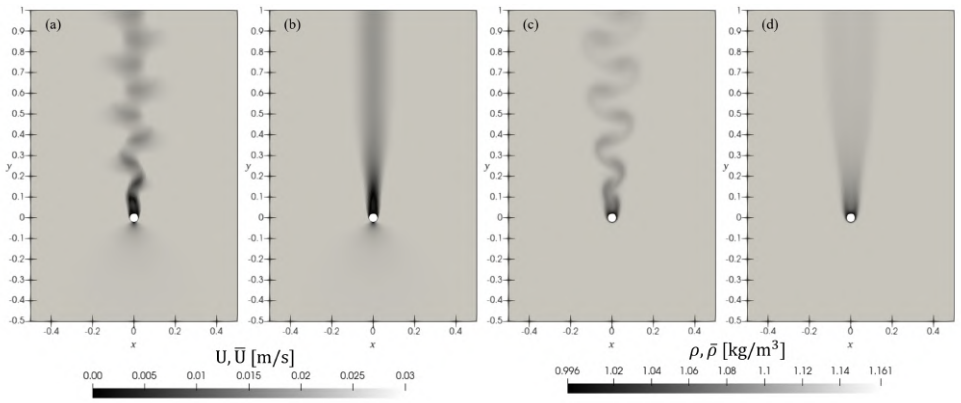

FIGURE 4.33: The contours of instantaneous (a) velocity magnitude and (c) density show the vortex shedding at the downstream of cylinder heater. (b) and (d) are mean velocity magnitude and density contours, respectively.

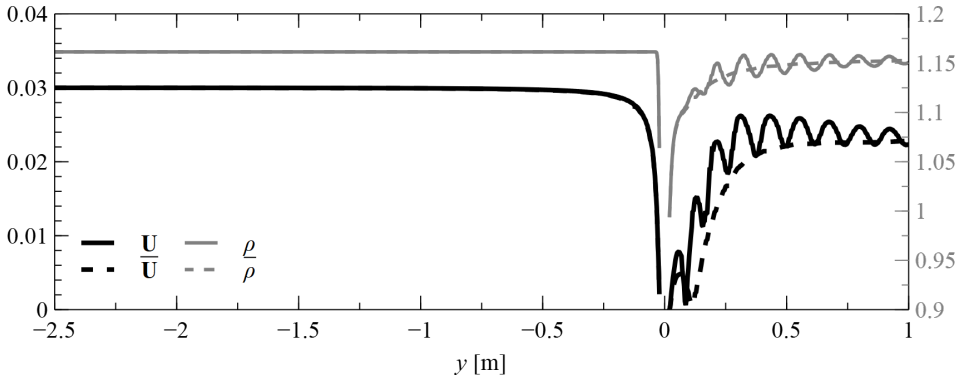

FIGURE 4.34: Profiles of instantaneous velocity and density, as well as their mean states.

4.4.2.1 Point Acoustic Source

A point acoustic source was initialized at $\boldsymbol{x}_0 = (0, -0.75)$ with $\epsilon = 100$ and $\sigma = 0.05$ for both fully nonlinear and DDT simulations. Hence, the maximum amplitude of pressure and density perturbations are $p'_{max} = \epsilon$ and $\rho'_{max} = \epsilon/\bar{c}^2$, respectively. The propagation of p' and ρ' in both (a) pure NL and (b) DDT simulations are presented in Figure 4.35 and Figure 4.36, respectively at three instants: (i) $t = 0.002$ s (pre-scattering), (ii) $t = 0.003$ s (scattering) and (iii) $t = 0.004$ s (post-scattering).

The normalized p' contours in Figure 4.35 shows the acoustic wave is scattered by the heater, form a secondary wave, denoted as contour **A** for both fully nonlinear

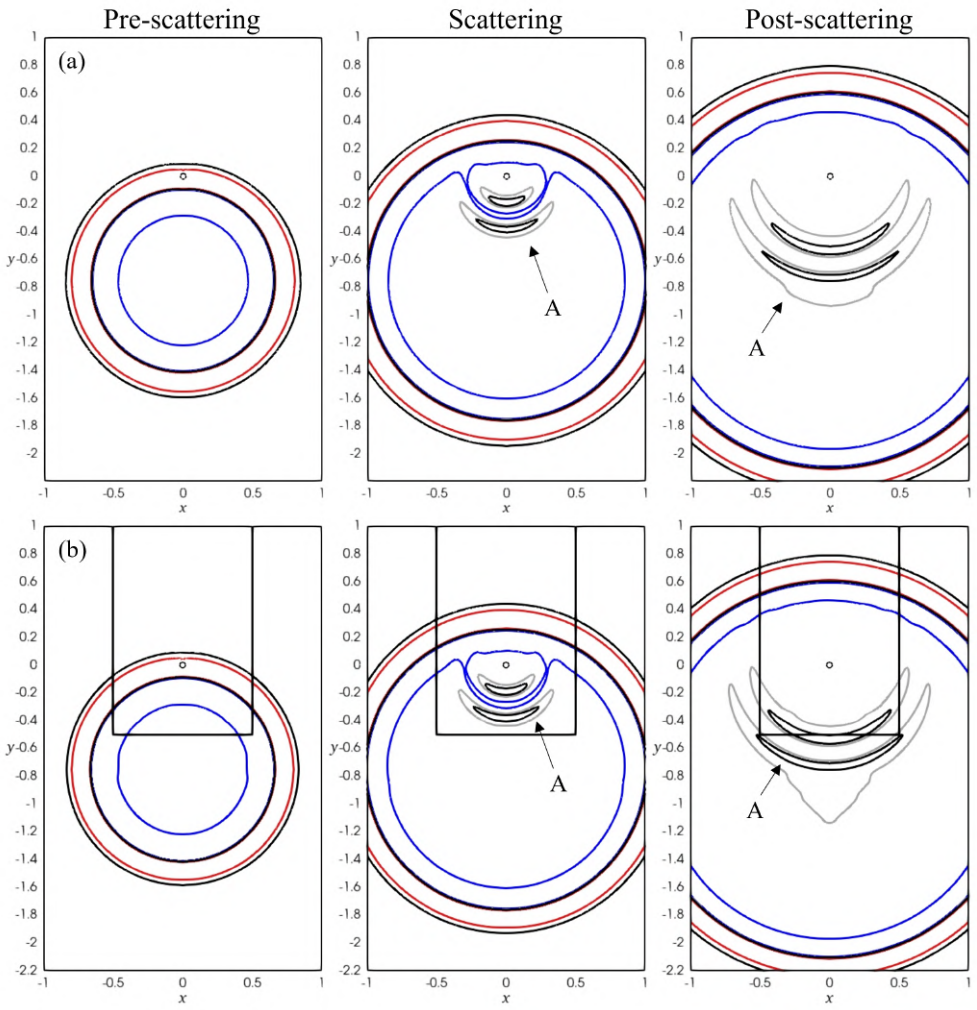

FIGURE 4.35: Series of interaction between thermal plume, cylinder heater and acoustic wave for (a) fully nonlinear and (b) DDT simulations. The contour lines are the normalized pressure perturbation, for which red/blue lines represent ± 0.01 and black/grey lines indicate ± 0.001.

and DDT simulations. The scattered wave **A** propagates downward and enters the linear region for DDT simulation. The normalized ρ' contours in Figure 4.36 share similar scattering wave contours, whereby scattered wave **A** is observed as well. In addition, the perturbation contour **B** in Figure 4.36 presents the density fluctuation due to the vortex shedding which has several order higher than the ρ'_{max}.

Post-scattering, the normalized p' and ρ' contours are observed to have differences among fully nonlinear and DDT simulations. This may be attributed to the excessive diffusion incurred in fully nonlinear simulation for propagation of small perturbation over long distance. Hence, a refined fully nonlinear simulation was

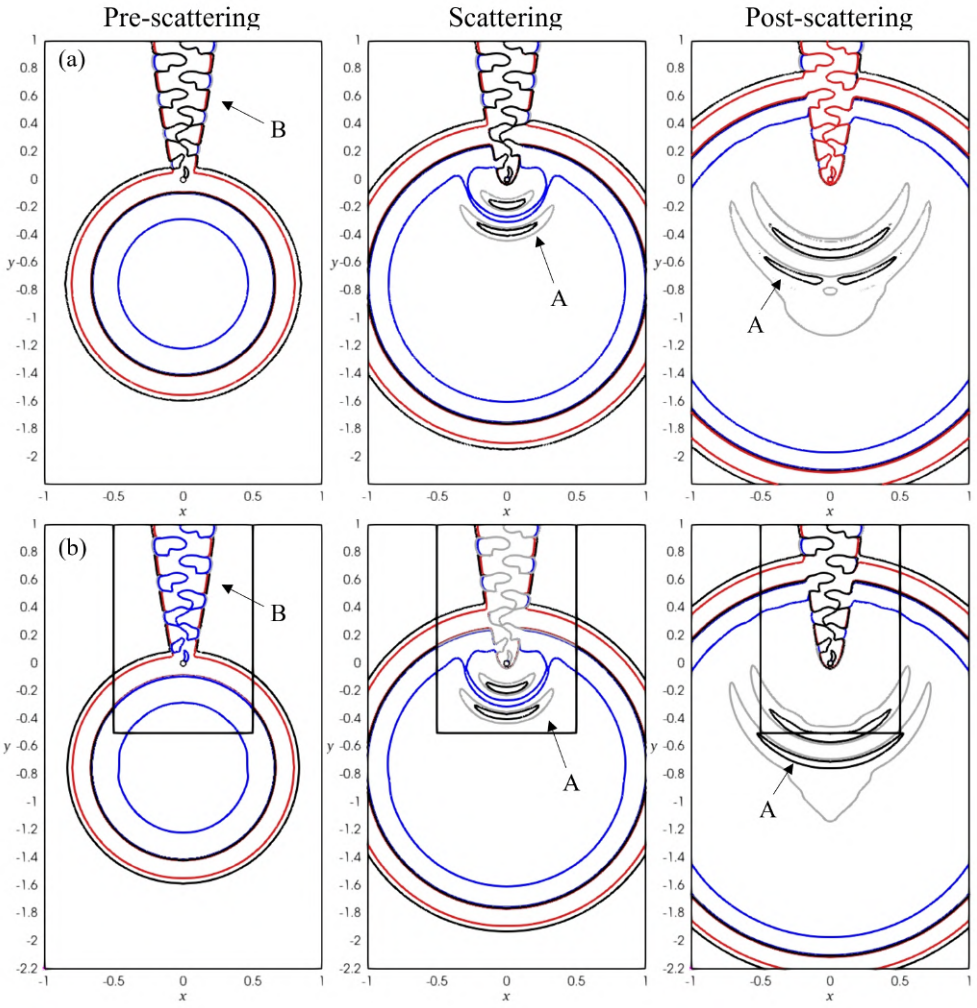

FIGURE 4.36: Series of interaction between thermal plume, cylinder heater and acoustic wave for (a) fully nonlinear and (b) DDT simulations. The contour lines are the normalized density perturbation, for which red/blue lines represent ± 0.01 and black/grey lines indicate ± 0.001.

conducted with far-field mesh resolution of $\Delta x = 0.0025$ m, making the total cells increased to 1.7M. The post-scattering results as shown in Figure 4.37 are compared with the fully nonlinear, refined fully nonlinear and DDT simulations for normalized (a) pressure and (b) density perturbations. In terms of scattered waves, the $\Delta x_{\mathrm{NL}} = 0.0025$ m simulation shows less diffusion as compared to $\Delta x_{\mathrm{NL}} = 0.005$ m fully nonlinear case, especially for normalized ρ' contours.

Quantitatively, the normalized p' was plotted along the axisymmetric line, as shown in Figure 4.38 at each instant corresponding to Figure 4.35 contours for all simulations. Likewise, the normalized ρ' is plotted along the axisymmetric line as

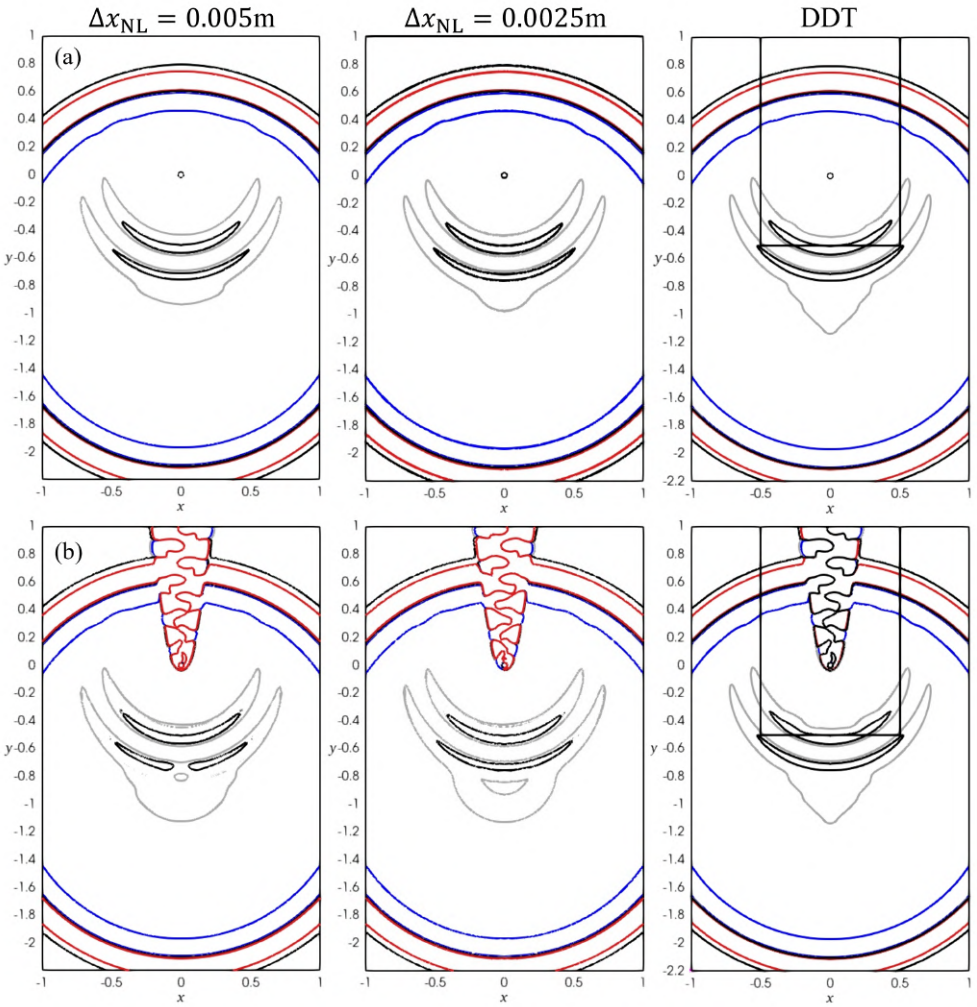

FIGURE 4.37: At $t = 0.004$ s, fully nonlinear ($\Delta x_{\mathrm{NL}} = 0.005$ and 0.0025 m) and DDT simulations are compared in term of normalized (a) pressure and (b) density perturbations contours, for which red/blue lines represent ± 0.01 and black/grey lines indicate ± 0.001.

presented in Figure 4.39. The source and scattered waves (**A**) of both fully nonlinear simulations concluded that the fully nonlinear simulation with $\Delta x_{\mathrm{NL}} = 0.005$ m is good enough and converged despite the discrepancy of vortex shedding ρ' contour (**B**) due to different phases. The ρ' source wave superposition with the density fluctuation due to vortex shedding, but this cannot be observed due to the higher order of ρ' by vortex shedding.

According to Table 4.5, DDT simulation, which yields better wave propagation results (as shown in Figure 4.38 and Figure 4.39), has saved the computational times up to 13.3% compared to converged fully nonlinear simulation ($\Delta x_{\mathrm{NL}} = 0.005$).

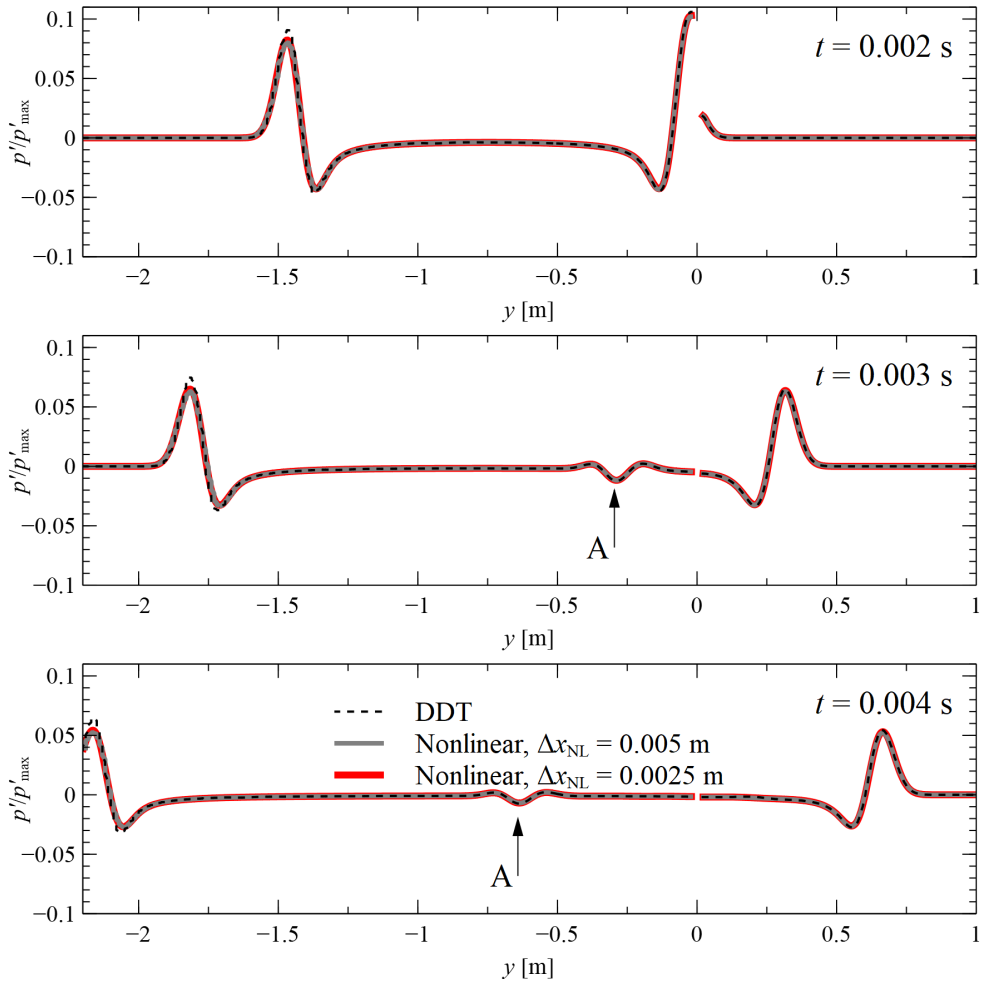

FIGURE 4.38: Comparing fully nonlinear ($\Delta x_{\mathrm{NL}} = 0.005$ (grey) and 0.0025 m (red)) and DDT simulations, the series of the normalized p' wave propagation are plotted at time stamps of $t = 0.002$ s, 0.003 s and 0.004 s, corresponding to pre-scattering, scattering and post-scattering conditions, respectively. **A** indicates the wave scattered by the heater located at $(0, 0)$.

TABLE 4.5: Comparison of computational cost-saving among different simulation types.

Simulation types	Resolution	Relative CPU hours	Cost-Saving
Nonlinear	$\Delta x_{\mathrm{NL}} = 0.005$	1	–
	$\Delta x_{\mathrm{NL}} = 0.0025$	4.7	–
DDT*	$R = 1$	0.867	13.3%

*where the $\Delta x_{\mathrm{L}} = 0.005$ m.

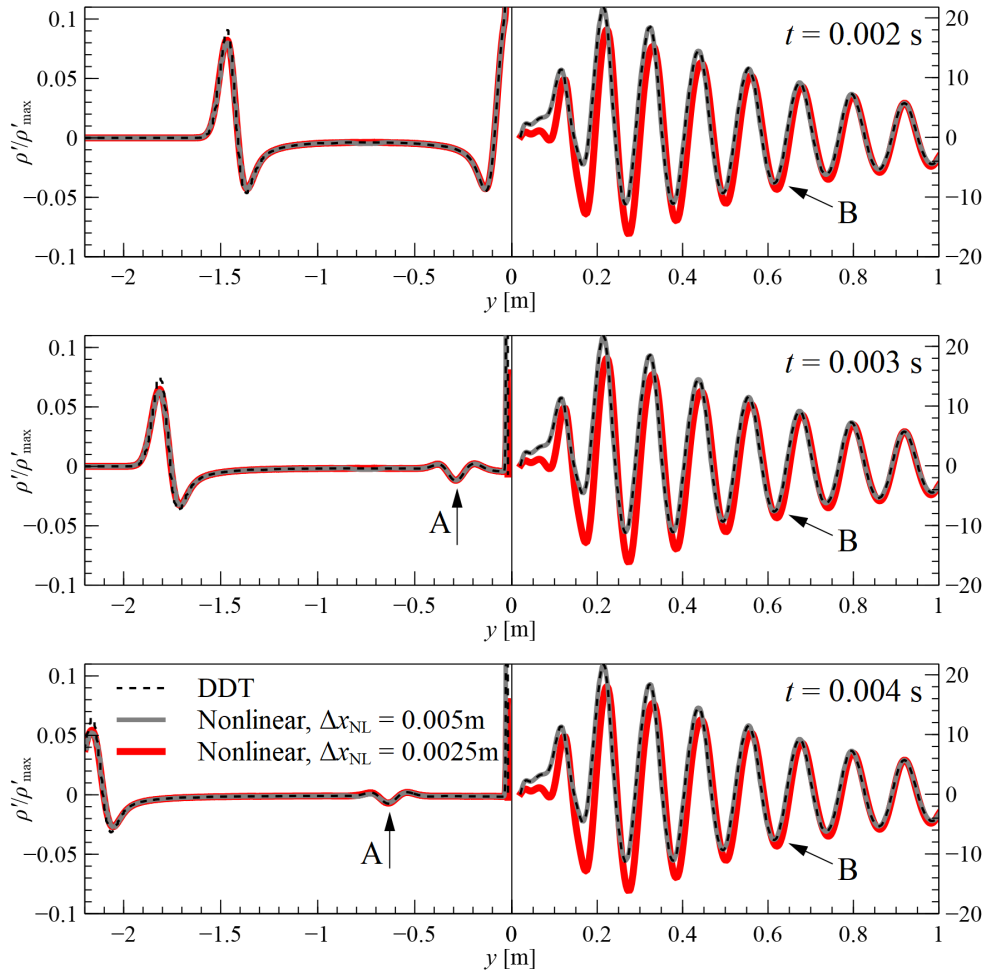

FIGURE 4.39: Comparing fully nonlinear ($\Delta x_{\mathrm{NL}} = 0.005$ (grey) and 0.0025 m (red)) and DDT simulations, the series of the normalized ρ' wave propagation are plotted at time stamps of $t = 0.002$ s, 0.003 s and 0.004 s, corresponding to pre-scattering, scattering and post-scattering conditions, respectively. Noted that, different scales are used for $y-$axis to show the scattered wave (**A**) and density fluctuation due to the vortex shedding (**B**).

4.4.2.2 Periodic Acoustic Source

A periodic p' and ρ' waves were initialized for DDT simulation in the linear region:

$$p'(\vec{r},t) = \epsilon \cos(k(\vec{r}-\vec{r_0}) - \omega t)\ , \quad \text{for} ||\vec{r}|| < \lambda \tag{4.19a}$$

$$\rho'(\vec{r},t) = \frac{\epsilon}{\bar{c}^2} \cos(k(\vec{r}-\vec{r_0}) - \omega t)\ , \quad \text{for} ||\vec{r}|| < \lambda \tag{4.19b}$$

where $\vec{r}$ is radius vector with $\vec{r_0} = (0,-1)$ and $\epsilon = 100$ Pa. $\omega = 2\pi f$ with frequency, $f = 500$ Hz. The wave number is defined as $k = 2\pi/\lambda$, and $\lambda = c/f$ is wavelength

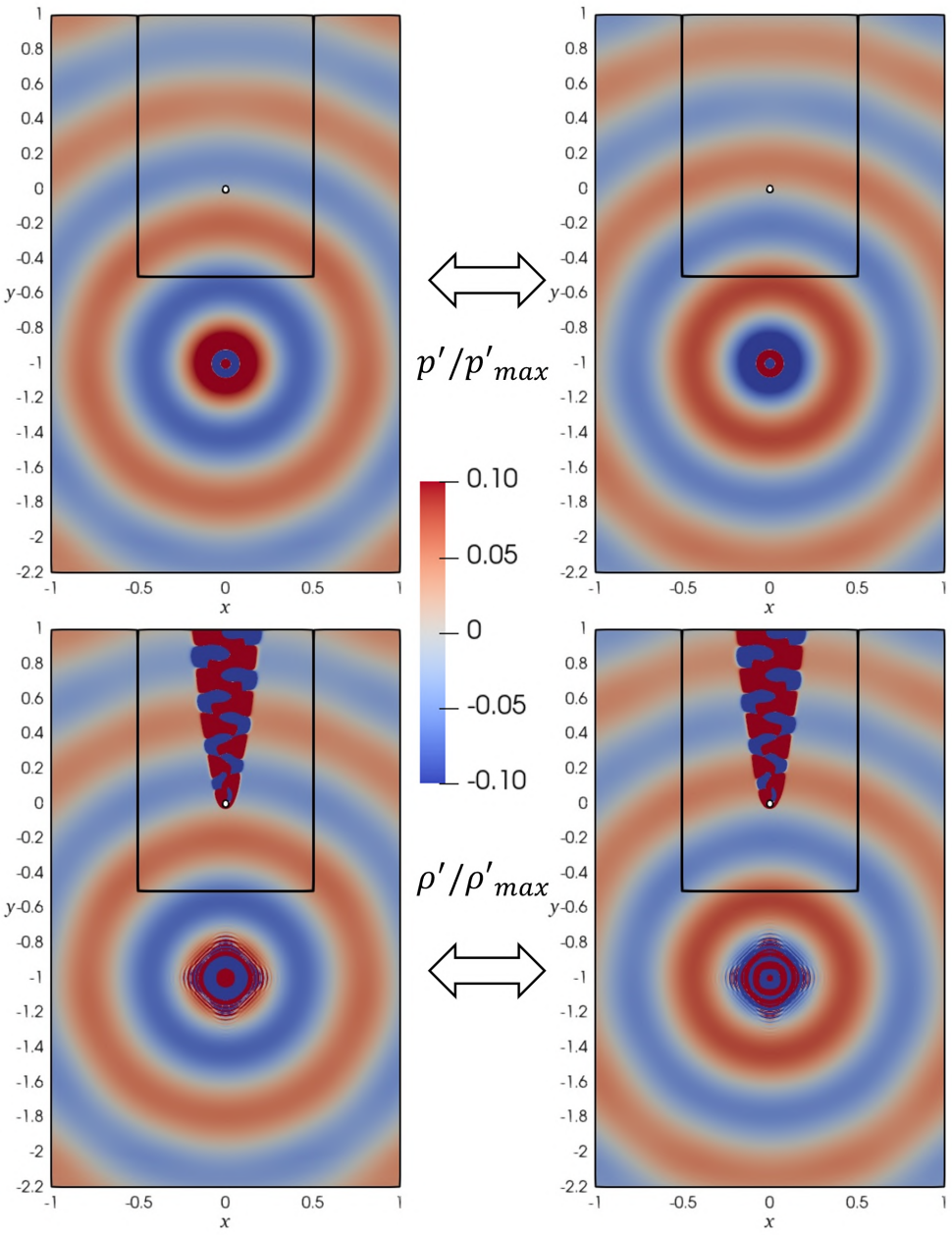

FIGURE 4.40: The normalized (Top row) p' and (bottom row) ρ' contours show periodic waves propagation over a heated cylinder for DDT simulation.

of the wave travelling in sound speed, c. The DDT simulation was conducted at $\Delta t = 1 \times 10^{-6}$ s with at least two periods of vortex shedding, i.e. until $t = 10$ s.

The DDT simulation results with periodic acoustic wave is shown in Figure 4.40 as the normalized (top row) pressure and (bottom row) density perturbations. The p'/p'_{max} contours show periodic pattern and same observation for ρ'/ρ'_{max} contours. Due to the relatively low acoustic and density fluctuations, there is no significant changing for the thermal plume and vortex shedding.

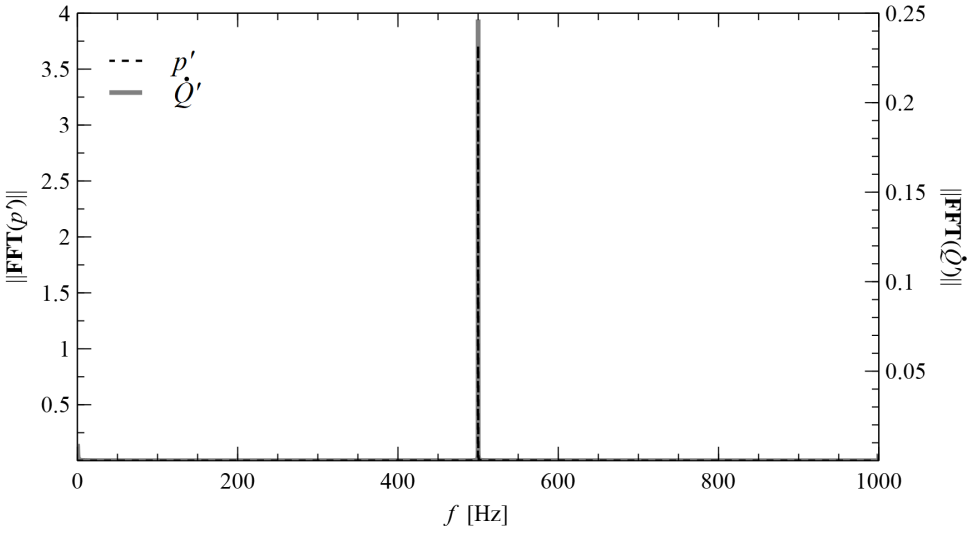

FIGURE 4.41: Fundamental frequency of 500 Hz for both p' and $\dot{Q}'$.

Quantitatively, FFT is performed for p' and $\dot{Q}'$ to evaluate the influence of periodic acoustic wave interaction with heated flow. The FFT of p' at location $(0.0, 0.5)$ and $\dot{Q}'$ by the heater are plotted in Figure 4.41. The fundamental frequency of p' and $\dot{Q}'$ is 500 Hz, matching with the periodic wave frequency. Low frequency 0.2 Hz observed in $\dot{Q}'$ FFT spectrum corresponds to the vortex shedding frequency. The periodic acoustic wave, generated in the linear region, propagates into nonlinear region where the heater exists and alters the flow fields around the heater and consequently resonates with the total heat release rate, $\dot{Q}$, of the heater. Fluctuation of heat release rate, $\dot{Q}'$, therefore, has shown the feasibility of DDT in solving the thermoacoustic problem.

4.5 Summary

To this end, the uses of DDT in 2D applications have been performed through internal and external flows cases with subsonic to supersonic flow regimes and heated flow. Among all 2D applications, the FFT studies have shown connection between linear and nonlinear regions and thus coupling by DDT is attained. Moreover, the reduction of the computational costs can be up to 89% while higher cell size ratio is used. Therefore, the superiority of DDT has clearly demonstrated by its computational cost-saving ability while preserving the accuracy.

Chapter 5

Preliminary Assessments on 3D DDT Applications

In this chapter, extension of domain decomposition technique (DDT) to 3D application was attempted to study the acoustic wave generation from a turbulent jet. An isothermal and two heated turbulent jets (see Appendix B.2) at temperature, $T = 600$ K and 900 K were simulated with $Re = 1 \times 10^4$. Comparison was done between fully nonlinear and DDT simulations. Several issues from DDT were reported for further evaluations. Additionally, an isothermal turbulent jet experiment was carried out to qualitatively validate the simulation results (see Appendix A). Moreover, to confirm LES flow solver can correctly predict the acoustic generation and propagation, the Rijke tube simulations were conducted with heater and chemically reacting flow as heating sources. The Rijke tube configuration will generate acoustic waves by establishing the thermoacoustic instability at specific resonance frequency. The assessment of the instabilities on numerical results was performed via the evaluation of Rayleigh criteria [7, 8].

5.1 Isothermal Turbulent Jet Flow

In the previous chapters, the DDT has been successfully extended to 2D space and successfully convected acoustic (cf. Section 4.3) and entropy waves (cf. Section 4.4). An extension of DDT to 3D space is preferred. By design, the extension is relatively straightforward. The mesh resolution setting and computational domain for fully

nonlinear turbulent jet simulation are illustrated in Figure 5.1 for the $xy-$ and $xz-$planes. The highlighted box shows the use of structured grid for jet inlet with diameter, $D = 0.01$ m, and encloses with combination of both structured and unstructured grids with resolutions of $\Delta = 0.0025$ m and $\Delta = 0.005$ m within $\pm 5D$ and $\pm 10D$, respectively. Far-field ($> \pm 20D$) region was constructed by uniform girds of size $\Delta = 0.01$ m. In jet axis direction ($y-$axis), structured grid was stretched with $\Delta y = 0.001$ m at the jet inlet ($y = 0$ m), $\Delta y = 0.01$ m at the outlet ($y = 0.8$ m) with the hyperbolic tangent function as the expansion ratio.

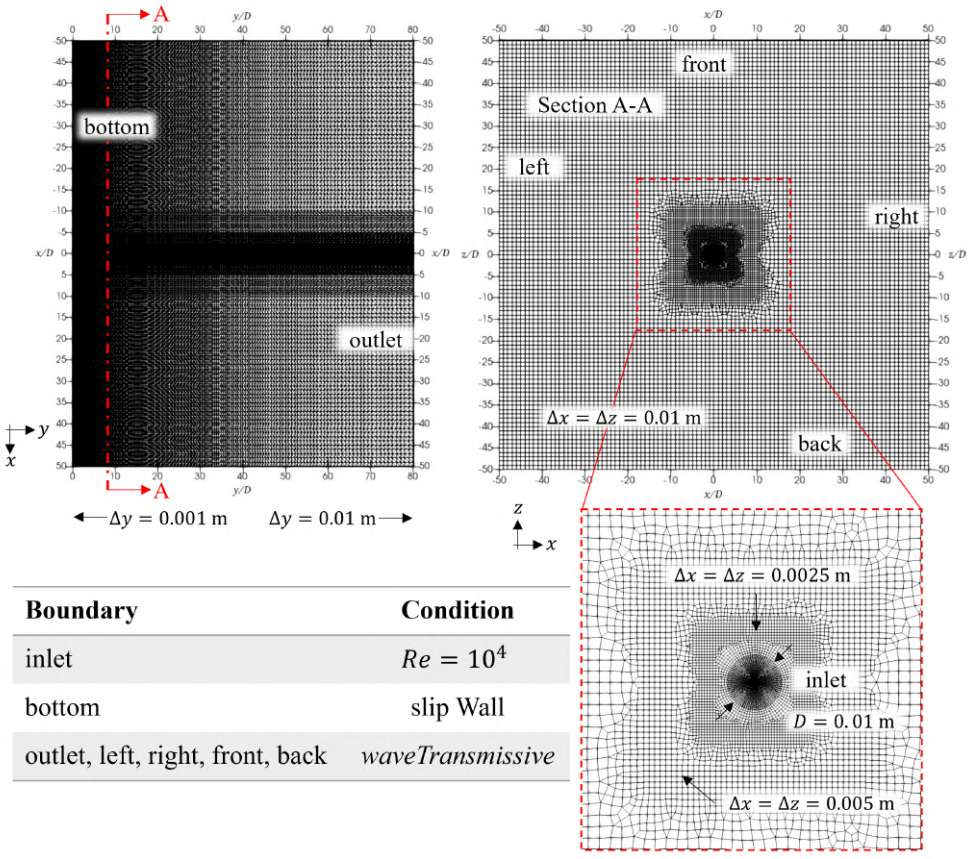

Boundary	Condition
inlet	$Re = 10^4$
bottom	slip Wall
outlet, left, right, front, back	*waveTransmissive*

FIGURE 5.1: A three-dimensional computational domain of fully nonlinear simulation, showing in $xy-$ and $xz-$planes. Jet inlet was located at (0,0,0) with diameter, $D = 0.01$ m.

The inlet velocity was set to be $v = 16$ m/s, corresponding to $Re \approx 10^4$, with the velocity fluctuation scales of 0.05% and 0.03% in axial and radial directions. The bottom boundary was in slip wall condition since the boundary layer is not the interest of this topic. The rest of the boundaries adopt '*waveTransmissive*'

boundary condition to transport outgoing ϕ waves from domain by solving (5.1) .

$$\partial_t \phi + w_p \cdot \nabla \phi = 0 \,, \tag{5.1}$$

where w_p is boundary wave speed which consists of sound speed, c and velocity component normal to the boundary, u_n. The jet temperature was maintained at $T = 300$ K for isothermal case. Heated jet cases, however, were maintained at $T = 600$ K and $T = 900$ K, correspond to typical compressor exit range and turbine inlet range, respectively. Idea gas law was applied for all cases. Constant specific heat capacity, Cp, and viscosity, μ were assumed for isothermal simulation, whereas, JANAF thermodynamics tables and Sutherland model were used to obtain Cp and μ, respectively, for heated jet simulations. LES subgrid model [80], *kEqn*, were applied for turbulent closure.

5.1.1 Acoustic and Vortical Wave Interactions

A 3D fully nonlinear isothermal turbulent jet simulation was conducted for 20 flow through time (FTT) of transition stage. Thereafter, collection of statistical mean fields was done for another 40 FTT. The instantaneous and mean contours of velocity and pressure fields are compared in Figure 5.2 along the centerplane. Spreading and decaying of the jet are observed in velocity magnitude fields. Meanwhile, the low pressure region (in blue color) indicates the end of jet potential core and start of the jet expansion.

To validate the jet, centerline mean velocity and half width of jet are examined quantitatively and compared to analytical solutions [86] as illustrated in Figure 5.3. The centerline mean velocity is plotted in log-scales, it shows the length of potential core is approximately $6D$, which is close to the potential core length of an axisymmetric free jet $6.2D$. The half width of jet is defined as the local distance of the points with half the local maximum velocity. The analytical decaying function (dotted line) is defined as,

$$\mathrm{U}/\mathrm{U}_{\max} = 6.2(y/D)^{-1} \,, \tag{5.2}$$

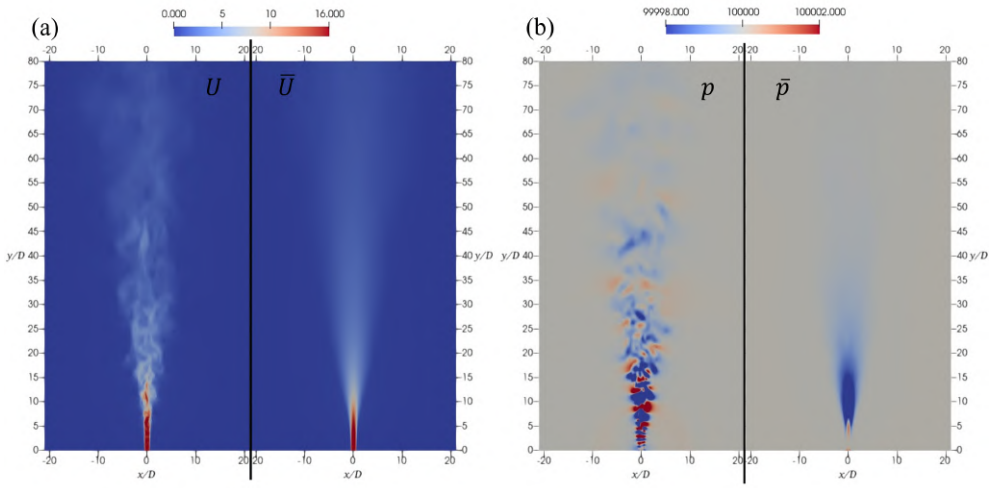

FIGURE 5.2: Comparison of the instantaneous and statistical mean contours of (left) the velocity magnitude and (right) pressure fields along the centerplane $z/D = 0$.

whereas, the analytical jet width is linearly dependent on streamwise direction,

$$r_{0.5}/D = 0.114(y/D) \ . \tag{5.3}$$

Based on Figure 5.3, the simulation results agree well with the theories especially the jet width profile despite the slight discrepancy of the centerline velocity decaying profile. The mean axial velocity profile showed in bottom graph of Figure 5.3 is found to attain self-similarity beyond $y/D = 10$.

TABLE 5.1: Summary of different time step for fully nonlinear jet noise simulations.

Δt	CFL	Wave behaviors
5×10^{-6} s	1.736	Nearly diffused once emitted
2×10^{-6} s	0.694	Diffused significantly at far-field
1×10^{-6} s	0.347	Waves are distinct and clear

Time convergence study was conducted to decide the time step for observing the jet noise generation as well as propagation. The results are summarized in Table 5.1. Three time steps were selected, $\Delta t = 1 \times 10^{-6}$ s, 2×10^{-6} s and 5×10^{-6} s, correspond to maximum CFL of 0.347 , 0.694 , 1.736 in term of sound speed. At $t = 0.03$ s, the instantaneous turbulent jet noise is presented in terms of pressure perturbation, p' at the centerplane of $x/D = 0$ and $y/D = 5$ in Figure 5.4 for different time steps. For $\Delta t = 1 \times 10^{-6}$ s, the number of observed wave is the

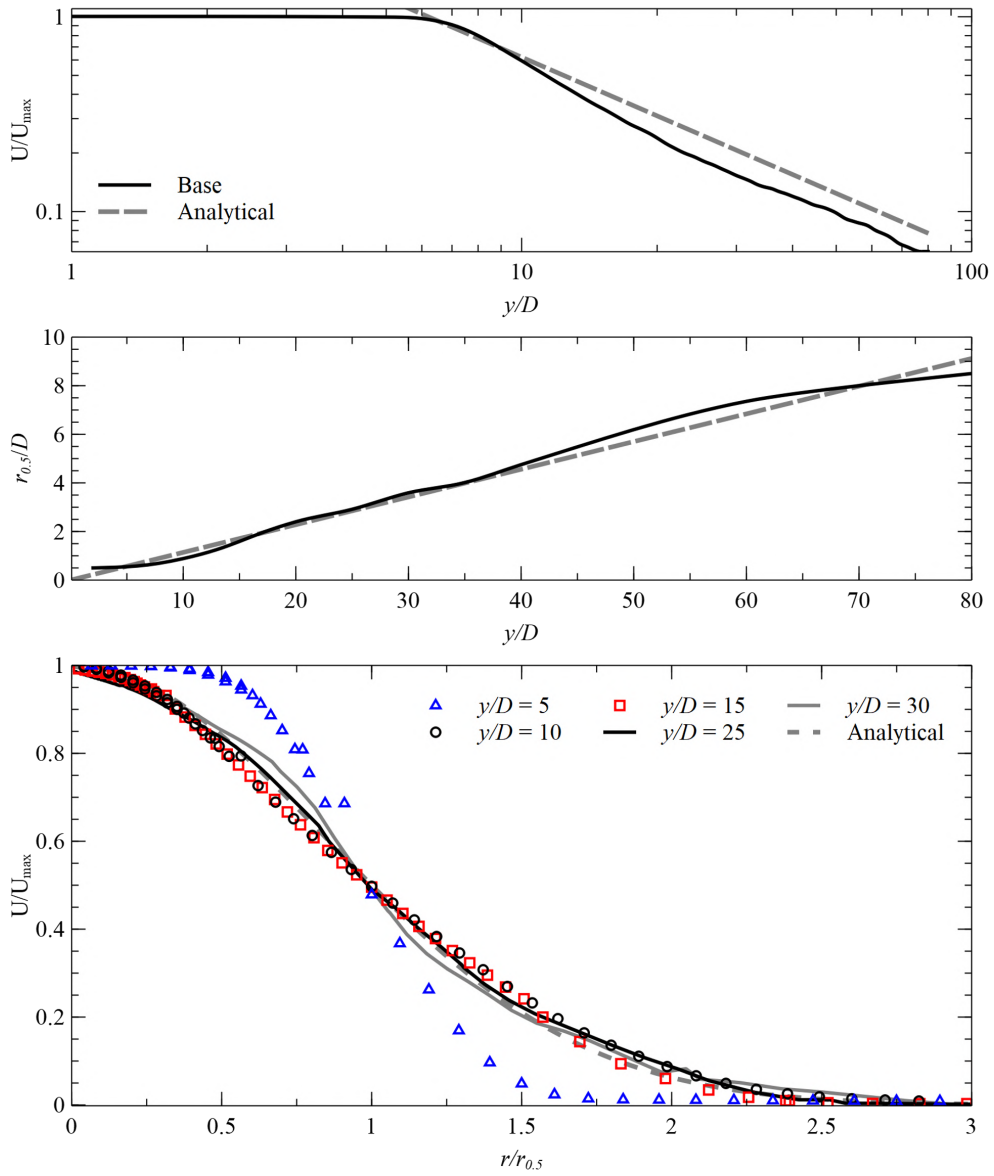

FIGURE 5.3: Comparison between simulation (solid line) and analytical solutions (dashed line) for (top) normalized centerline jet mean velocity profile and (middle) jet width and (bottom) self-similarity of the jet axis velocity.

highest compared to other Δt. Hence, the smaller the time step, the higher the number of observable wave due to the less of dissipation error. It is safe to say that $\Delta t = 1 \times 10^{-6}$ s is adequate since CFL is less than 0.5 and p' propagation is clearly observed. In this isothermal jet simulations, therefore, $\Delta t = 1 \times 10^{-6}$ s is considered for the rest of both fully nonlinear and DDT simulations.

From Figure 5.4, the jet noise, p' originates from the jet lip at inlet and propagates downstream. This is known as jet noise caused by the high-velocity jets which creating shear layer with the ambient air. The shear layer is believed to be responsible

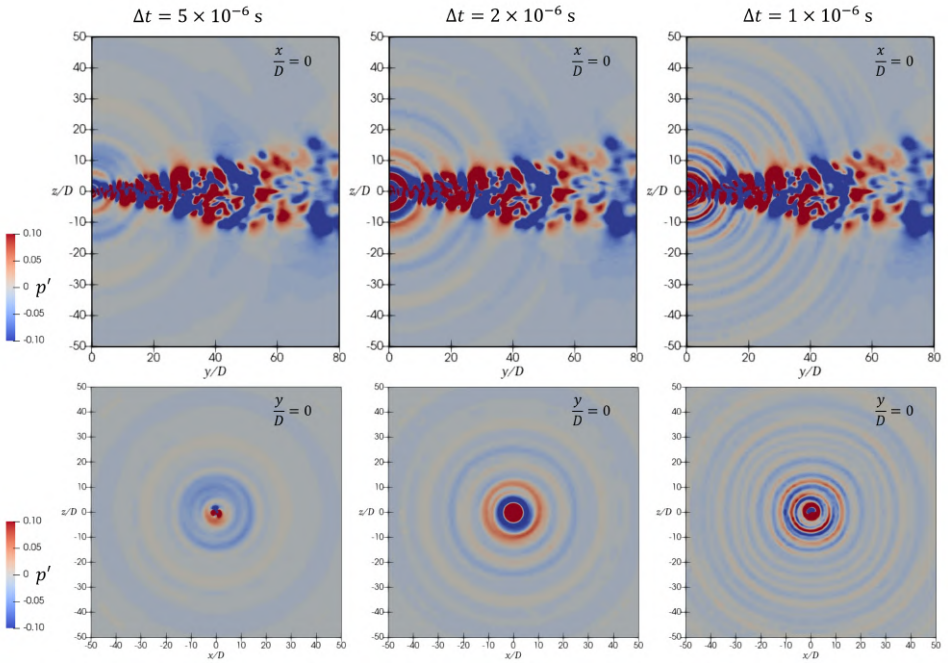

FIGURE 5.4: The pressure perturbation contours at $t = 0.03$ s on (first row) $x/D = 0$ and (second row) $y/D = 5$ for different time step. The smaller the time step, the higher the number of waves can be observed.

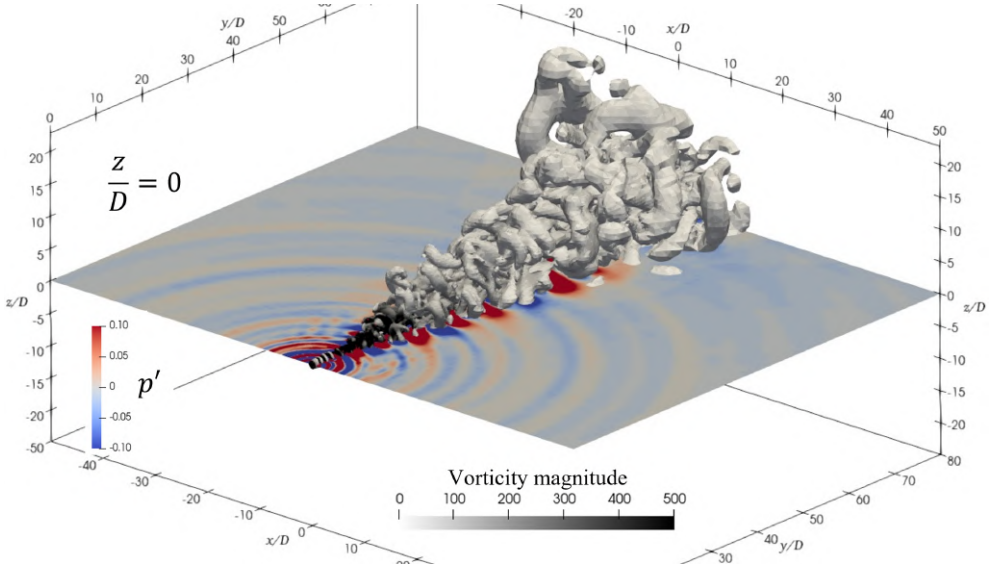

FIGURE 5.5: Isosurface of Q-criterion colored by vorticity magnitude for Q = 1 together with contour centerplane of pressure perturbation at $t = 0.1$ s.

for the noise generation. It can be proven by observing Q-criterion graph as shown in Figure 5.5. The isosurface of Q-criterion, at Q = 1, extracts the coherent vortical structures, colored by vorticity magnitude, is presented along with p' contours at centerplane $z/D = 0$. The annular isosurface of Q-criterion near to the inlet indicates the shearing layer between the jet and ambient air with approximately

zero vorticity magnitude. This annular-shaped shearing layer serves as the source of noise, where the p' contours shows the waves are emitted and propagating from it.

5.1.2 Domain Decomposition Technique Simulations

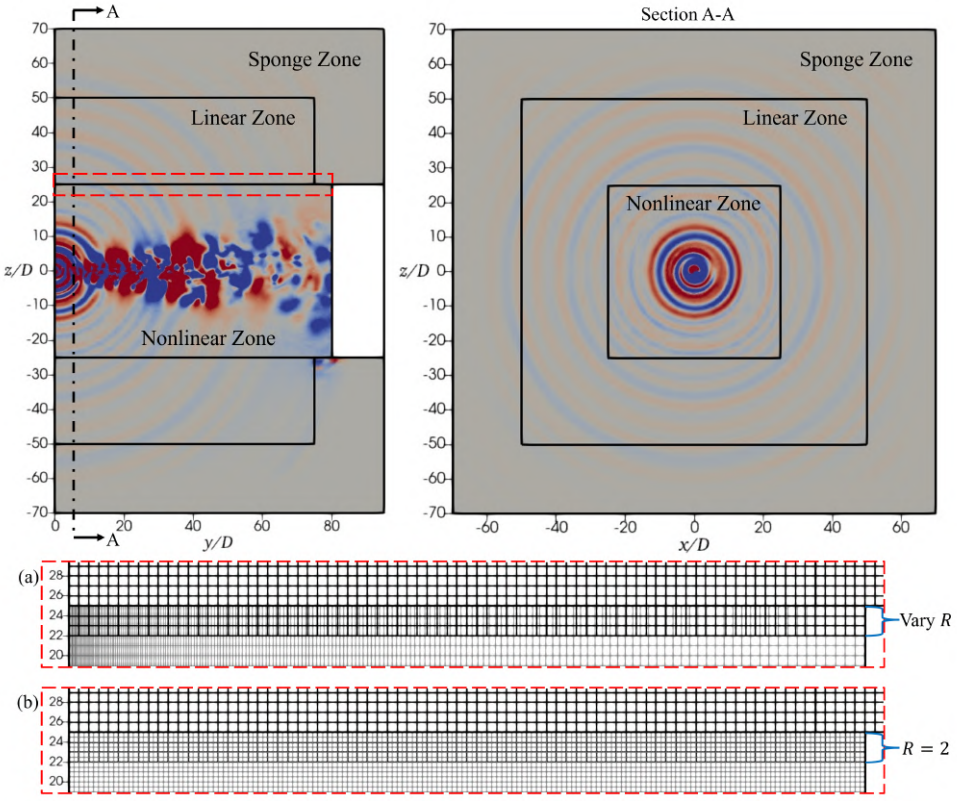

FIGURE 5.6: A schematic drawing describes the proportion of three zones (the nonlinear, linear and sponge zones) in a DDT simulation at (left) $x/D = 0$ and (right) $y/D = 5$ planes. The overlapping zone as featured in dotted-box shows the overlap ratio between linear (black grids) and nonlinear (grey grids) cells, R, is either (a) varying or (b) constant $R = 2$ along the jet axis for two different DDT simulations.

A DDT simulation was conducted using the same mesh resolution in the previous fully nonlinear (combination of structured and unstructured grids) simulation for nonlinear region ($-25 \geqslant x/D, z/D \geqslant 25$), whereas the linear region consists of uniform Cartesian mesh with size of 0.01 m throughout the range of $-50 \geqslant x/D, z/D \geqslant 50$ and $0 \geqslant y/D \geqslant 75$ as depicted in Figure 5.6. The overlap ratio, R is varies along the $y-$axis as shown in Figure 5.6 (a). Another DDT simulation was conducted with nonlinear region consists of fully uniform structured

cells, 0.005 m in size, has overlap ratio of two, $R = 2$ as illustrated in Figure 5.6 (b). For both DDT simulations, the linear regions were terminated with a sponge layer of $20D$ width and strength of 0.05 to absorb the outgoing waves. As discussed earlier, $\Delta t = 1 \times 10^{-6}$ s is used for these two DDT simulations. 7−point DRP scheme [73] was applied to solve linear equations, hence three layer of linear cells were used for mapping, and 9-point explicit filter scheme [76] with 0.05 strength was considered.

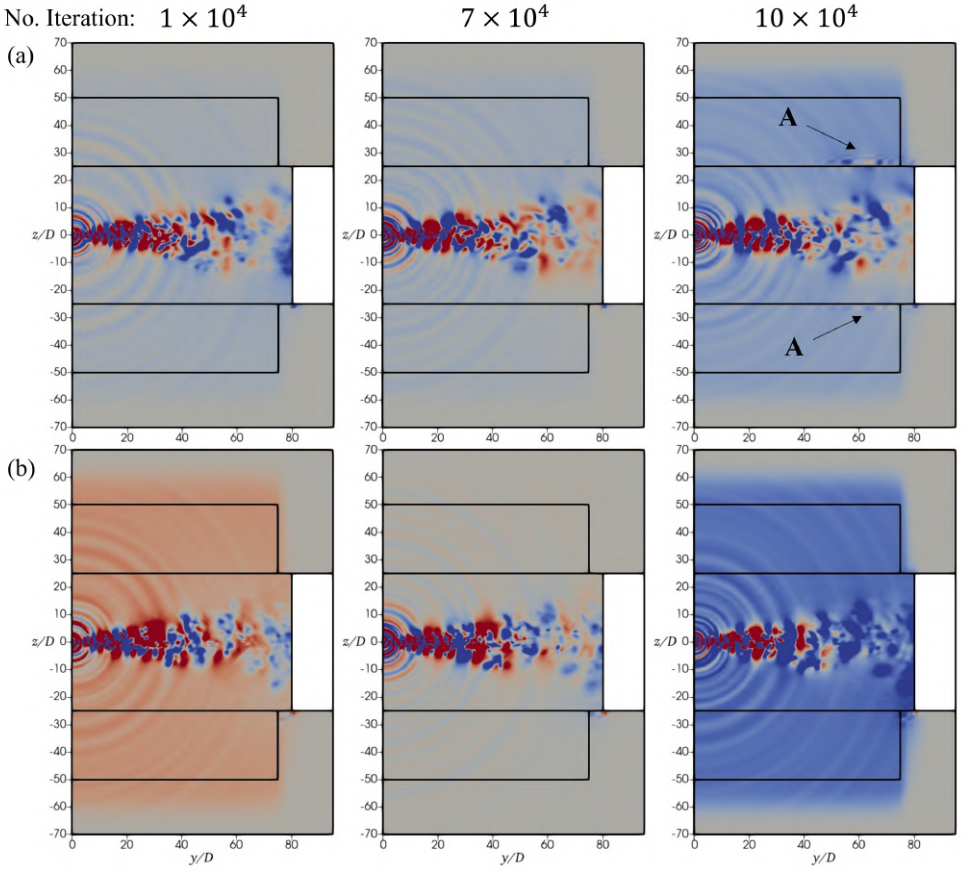

FIGURE 5.7: Pressure perturbation, p' contours are shown at (left column) 1×10^4, (middle column) 7×10^4, and (right column) 10×10^4 numbers of iteration for (a) vary R and (b) $R = 2$ grid settings of DDT simulations. Contour color ranges within ±0.2 Pa. The observed spurious oscillations ('**A**') at interface can be eliminated with a constant R.

Solutions of three iteration steps are summarized in Figure 5.7 as the pressure perturbation contours with color ranges between ±2 Pa. For vary R simulation, Figure 5.7 (a) shows the accumulative error appeared at the downstream of the interface between linear and nonlinear regions when time increases. This spurious oscillations, labeled as **A**, are not observed in fully nonlinear simulation and it can be evaded by using constant overlap ratio R. This is proven in Figure 5.7 (b), using

$R = 2$, where the spurious oscillations at the interface are not observable and no sign of recurrence.

Beside the spurious oscillation problem, the pressure mean state is varying overtime in both simulations as presented in Figure 5.7 where the background color is changed from light blue to dark blue for (a) vary R case and red to blue for (b) constant $R = 2$ case. Therefore, the overlap ratio $R = 2$ is still not sufficient for 3D DDT simulation to work well. Higher overlap ratio is required as suggested in Chapter 4. It is, however, become intractable due to the tremendous number of cells and costs required for high overlap ratio. Nonetheless, this isothermal turbulent jet study has suggested constant and higher R is better and shown DDT works for 3D, but not without caveats.

5.2 Assessment of Thermoacoustic Instability

To extend the 2D thermal plume simulation done in Section 4.4 and confirm the capability of LES in acoustic generation prediction, the Rijke tube configuration is selected for its simple geometry and the ability of acoustic generation via thermoacoustic instability. For this study, fully nonlinear Rijke tube simulations are considered with heater and chemical reacting flow as heating sources. Combustion models [81, 83] are integrated into LES solver to represent the chemical reacting flows. The existence of instabilities in numerical results was then assessed by Rayleigh criteria [7, 8].

5.2.1 Assessment Criteria

A common way to assess thermoacoustic instability is by examining the Rayleigh criterion [87–89]. Traditionally, the standard Rayleigh criterion [7] was used as it is easy to implement both numerically and experimentally. Recently, the extended Rayleigh criterion [8] has been introduced as a more accurate technique because it accounts for acoustic losses that are neglected by the standard Rayleigh criterion. In general, one can treat the extended Rayleigh criterion as the generalization of the standard Rayleigh criterion. However, the extended Rayleigh criterion can only be implemented numerically.

Thermoacoustic instability can be directly assessed from the acoustic energy equation. The linearized, inviscid acoustic energy equation is given by [90],

$$\partial_t e'_a + \nabla \cdot (p'\mathbf{U}') = s' \ , \tag{5.4}$$

where e'_a and s' are small perturbations of the specific acoustic energy and acoustic source, respectively. The small perturbations of pressure, p', velocity, $\mathbf{U}'$, and specific heat-release rate, $\dot{q}'$, are computed from,

$$p'(\mathbf{x},t) = p(\mathbf{x},t) - \bar{p}(\mathbf{x}) \ , \tag{5.5a}$$

$$\mathbf{U}'(\mathbf{x},t) = \mathbf{U}(\mathbf{x},t) - \overline{\mathbf{U}}(\mathbf{x}) \ , \tag{5.5b}$$

$$\dot{q}'(\mathbf{x},t) = \dot{q}(\mathbf{x},t) - \bar{\dot{q}}(\mathbf{x}) \ , \tag{5.5c}$$

where $|p'(\mathbf{x},t)| \ll |\bar{p}(\mathbf{x})|$, $|\mathbf{U}'(\mathbf{x},t)| \ll |\overline{\mathbf{U}}(\mathbf{x})|$ and $|\dot{q}'(\mathbf{x},t)| \ll |\bar{\dot{q}}(\mathbf{x})|$ are typically assumed. In essence, (5.5a), (5.5b) and (5.5c) define the decomposition of the time-varying variables into their respective steady, $\overline{(\,)}(\mathbf{x})$, and unsteady, $(\,)'(\mathbf{x},t)$, components. The linearized acoustic source is calculated from,

$$s' = \frac{\gamma - 1}{\gamma} \frac{p'\dot{q}'}{\bar{p}} \ . \tag{5.6}$$

Rearranging and integrating (5.4) over a finite volume, it can be shown that,

$$\frac{d}{dt} \int_{CV} e' dV = \int_{CV} s' dV - \int_{CS} (p'\mathbf{U}') \cdot d\mathbf{S} \ , \tag{5.7}$$

where dV represents a cell volume and $d\mathbf{S}$ is a local cell surface area vector. It is observed that the last term represents an acoustic flux. So, (5.7) can be reduced to an ordinary differential equation,

$$\frac{dE'}{dt} = S' - F' \ , \tag{5.8}$$

where E' is the integral acoustic energy, and F' and S' terms refer to the acoustic loss and acoustic source/sink terms, respectively. From (5.6), S' accounts for unsteady pressure, p', and unsteady specific heat release rate, $\dot{q}'$, which depends on the heat source. The standard Rayleigh criterion can be recovered by integrating

(5.8) without the acoustic loss term, F',

$$E'_{std}(t) = \int_0^t S'(t^*)dt^* \ . \tag{5.9}$$

Hence, in accordance with the standard Rayleigh criterion, the acoustic energy budget, E'_{std}, must be greater than zero to trigger thermoacoustic instabilities [7]. On the other hand, the extended Rayleigh criterion [8] retains the acoustic loss and is therefore given by,

$$E'_{exd}(t) = \int_0^t \big(S'(t^*) - F'(t^*)\big)dt^* \ . \tag{5.10}$$

A finite-volume based tool is developed to evaluate the acoustic sources and acoustic losses. First, a control volume, V, is defined, for which the volume bounded within the Rijke tube wall is used in this work. For chemically reacting flows, the flames are the heat sources and can result in a non-local heat distribution depending on the complex interaction of the turbulent flow and flames. The acoustic source, S', is then obtained from,

$$S' = \sum_{i=1}^{N} \frac{\gamma - 1}{\gamma} \frac{p'_i \dot{q}'_i}{\bar{p}_i} \Delta V_i \ , \tag{5.11}$$

where N and ΔV_i are the total number of cells in the prescribed control volume and individual volume of cell i, respectively. $\dot{q}_i$ is interpolated from a thermo-chemical table that is computed based on chemical reaction rate. The acoustic flux, F', is computed from,

$$F' = \sum_{i=1}^{N} \left(\sum_{f=1}^{M} p'_f \mathbf{U}'_f \cdot \mathbf{A}_f \right)_i \ , \tag{5.12}$$

where M and $\mathbf{A}_f$ are the total number of cell faces and one of the surface area vectors of the individual cell i. p'_f and $\mathbf{U}'_f$ are the pressure and velocity perturbations on a cell face surface f, interpolated linearly from the ith cell center. Both versions of acoustic energy budgets, E'_{std} and E'_{exd}, are then calculated based on (5.9) and (5.10), respectively. Note that, for the above equations, F' is general while S' is dependent on the type of heat source. For the case of a heating element, the heat

source, $\dot{Q}$ can be computed from Fourier's law,

$$\dot{Q} = \sum_{k=1}^{N_{\text{adj}}} -\kappa A_k \frac{dT}{dn} \,, \tag{5.13}$$

where N_{adj} is the total adjacent cells next to the heater wall and dT/dn is the normal temperature gradient at the heater wall, A_k.

Note that the standard Rayleigh criterion can be simplified further for non-combustion cases with concentrated local heat source. To trigger thermoacoustic instabilities, $E'_{std} > 0$, so the time integration of S' must be positive. This is only possible if (i) the phase difference between p' and $\dot{Q}'$ is within $\pm 90°$ and (ii) p' and u'_z are out of phase [47].

5.2.2 Numerical Configurations

Two numerical setups were investigated. First, a non-combustion configuration that adds heat to the flow using a donut-shaped heater is placed, from the bottom of the tube, at $L/4$ and $3L/4$ separately (shown in Figure 5.8 for the case with heater at $L/4$), where L is the length of the Rijke tube. Second, a combustion configuration in which fuel/air mixture is introduced from a Bunsen burner outlet at $0.2L$ from the bottom of the tube (as shown in Figure 5.9). All simulations are performed in a three-dimension cylindrical domain with height equal to $1.6L$ and radius equal to $52.5D$, where D is the diameter of Bunsen burner nozzle. The blockage ratio, defined as the ratio of nozzle diameter (or two times the thickness of heater) to tube diameter, is 0.2 in all configurations. For all simulations, $L = 1$ m and $D = 1$ cm. The domain extent was tested to verify that minimal acoustic reflections occur from the outer boundary conditions.

Figure 5.8 highlights the heating element zone, which consists of: (i) a donut-shaped heater surrounded by dense and unstructured grids as shown in sectional view A-A; (ii) a 'butterfly' topology mesh (O-H grids) throughout the domain as illustrated in sectional view B-B. Figure 5.9 shows the combustion Rijke tube setup, which consists of structured grids with 'butterfly' topology as illustrated in the sectional view C-C. There are a total of 1.3M and 2.4M cells used for the non-combustion and combustion configurations, respectively.

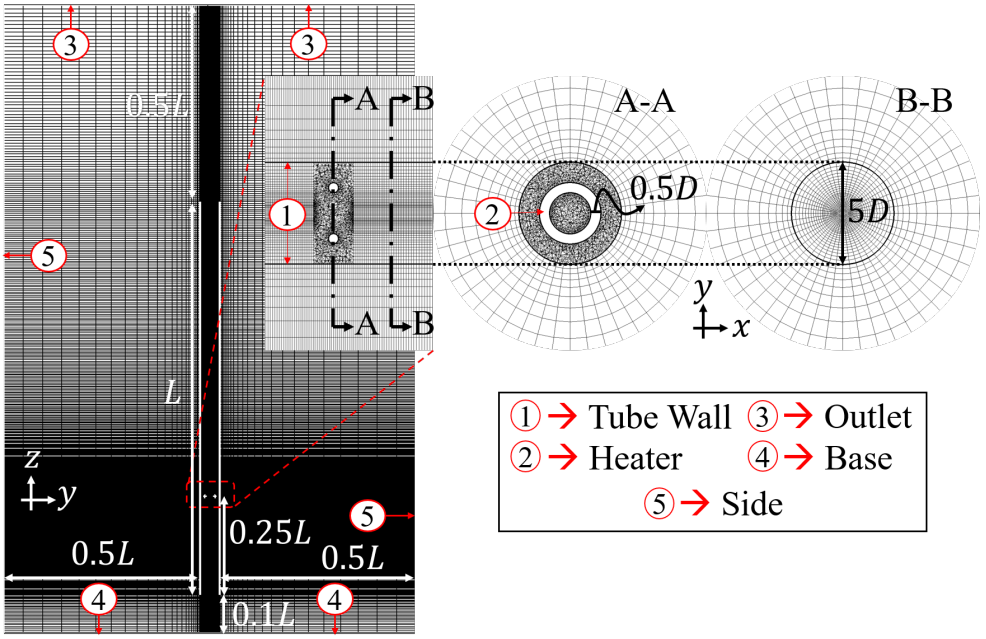

FIGURE 5.8: A three-dimensional computational domain of non-combustion Rijke tube case, consisting of hybrid mesh of unstructured grids near heating donuts-shaped element at $L/4$ from the bottom of tube and structured everywhere else. The parameters $L = 1$ m and $D = 1$ cm.

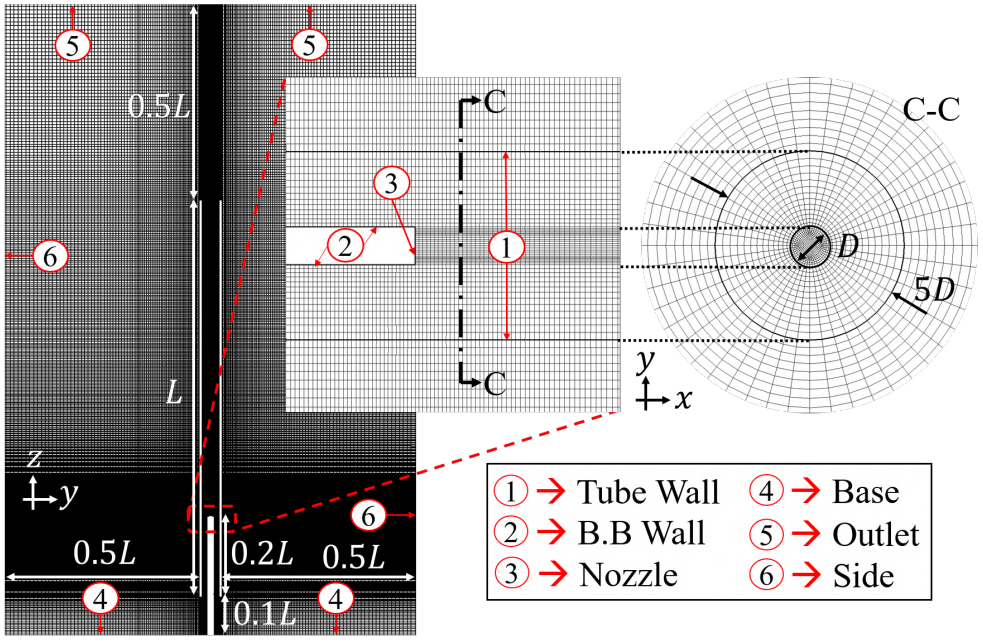

FIGURE 5.9: A structured three-dimensional computational domain of combustion Rijke tube case where the parameters $L = 1$ m and $D = 1$ cm.

No-slip condition was applied to the Rijke tube, heater, and Bunsen burner walls. For non-combustion cases, the heater temperature was maintained at 1500 K and all other wall boundaries were adiabatic. For combustion cases, propane (C_3H_8)

was used as the fuel. The inlet mixture fraction, Z, of the FPI and FPV cases were set to 0.2 and 1.0, respectively, with inlet velocity adjusted to match the fuel mass flow rate of the two cases. Moreover, the inlet mixture fraction variance, Z''^2, and progress variable, C, were set to zero for both FPI and FPV cases. Zero gradient condition was used for all other boundaries of the Z, Z''^2, and C variables.

For all simulations, the ambient pressure and temperature were 1 bar and 300 K, respectively. The dynamics viscosity, μ, was obtained from the Sutherland model [91] for the heater case and interpolated from thermo-chemical tables [92] for the combustion simulations. The JANAF thermodynamics tables were used for both cases in the calculations of the specific heat capacity.

5.2.3 Baseline Rijke Tube Configuration

Figure 5.10 presents the instantaneous temperature contours at different time. Figure 5.11 presents the local flow velocity $\mathbf{U}_z$ evaluated at $z/L = 0.75$ along the centerline, where $z/L = 0$ denotes the bottom of tube. From both figures, it is clear that three different acoustic phases exist. Initially there is a transient phase I, followed by a transitional phase II, and finally a fully developed quasi-periodic phase III. In phase I, the natural convection is induced by the donut-shaped heater where the ambient air gains heat and rises. From the local axial velocity in Figure 5.11, $\mathbf{U}_z$ increases sharply to approximately 1.5 m/s during transition to phase II. In this period, the hot air continues to rise and forms an annular convected plume, as shown in the bottom row of Figure 5.10.

To further examine the three acoustic phases, the fast Fourier transform (FFT) is used to examine the frequency spectrum of p' and $\mathbf{U}'_z$ computed at $z = 3L/4$ along the centerline, as plotted in Figure 5.12. The frequency spectra of $\mathbf{U}'_z$ in phase I and II show low frequency broadband response due to the developing flow, along with a weaker periodic structure around 177 Hz. In phase III, $\mathbf{U}'_z$ has a dominant fundamental frequency, indicating that the periodic fluctuations illustrated in Figure 5.11 are due to resonance. The same periodic fluctuations are also reflected in the instantaneous temperature contours in Figure 5.10 in the form of a periodic flow structure downstream of the heater element.

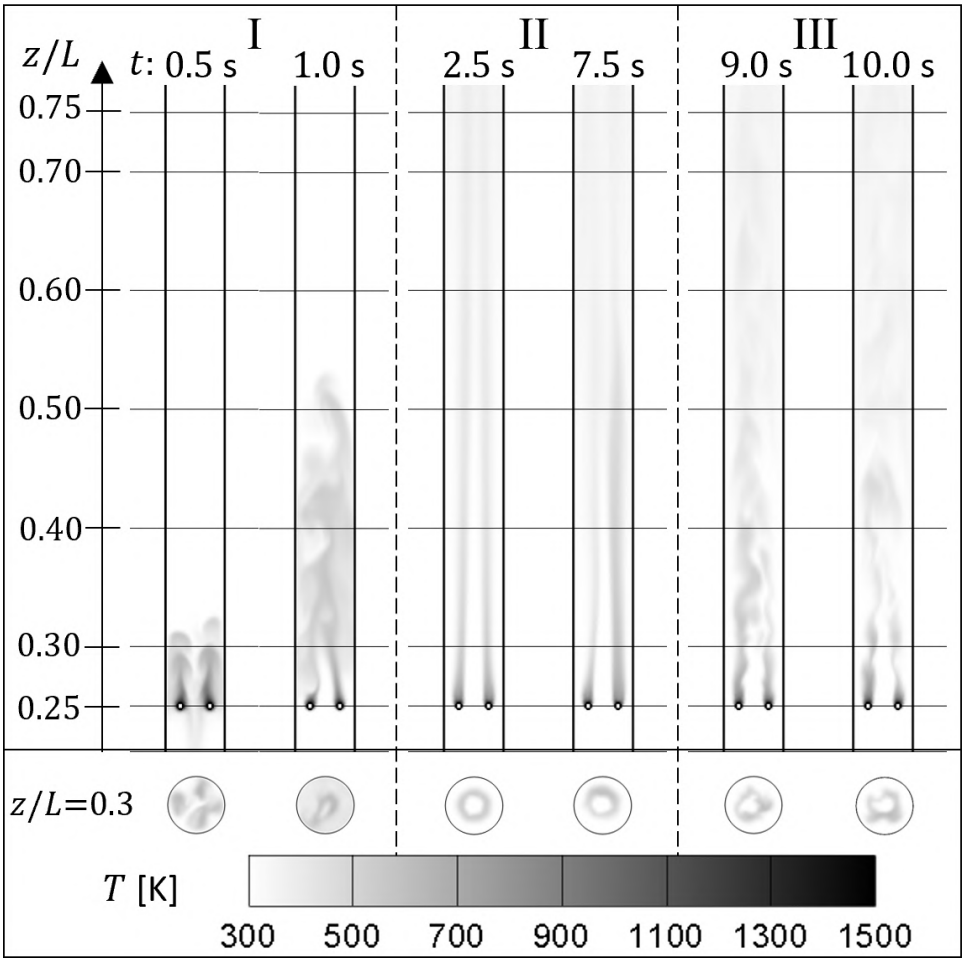

FIGURE 5.10: Temperature contours of a heater Rijke tube simulation in three different phases: (I) Transient; (II) Transition; and (III) Repetitive phases.

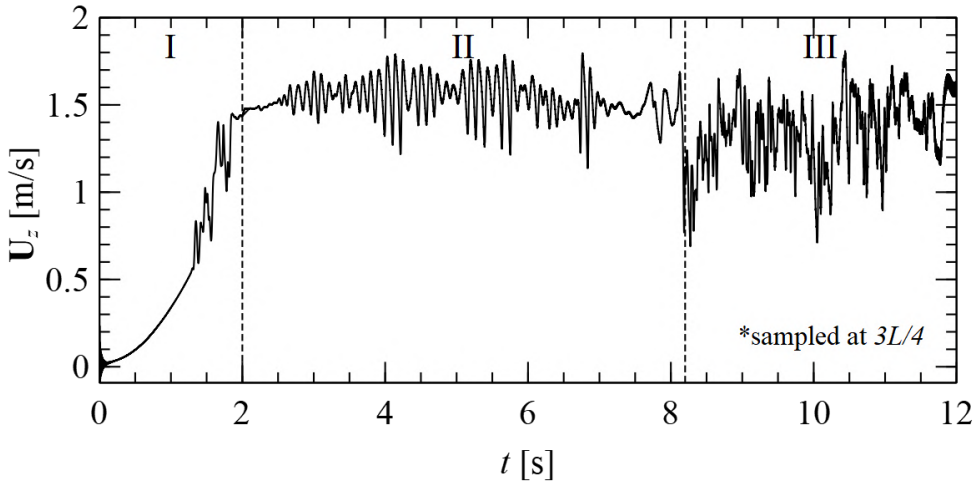

FIGURE 5.11: The axial velocity, $\mathbf{U}_z$, collected at $3L/4$ from the bottom end of tube. Three distinct phases are discernible, namely the (I) transient, (II) transition and (III) repetitive phases.

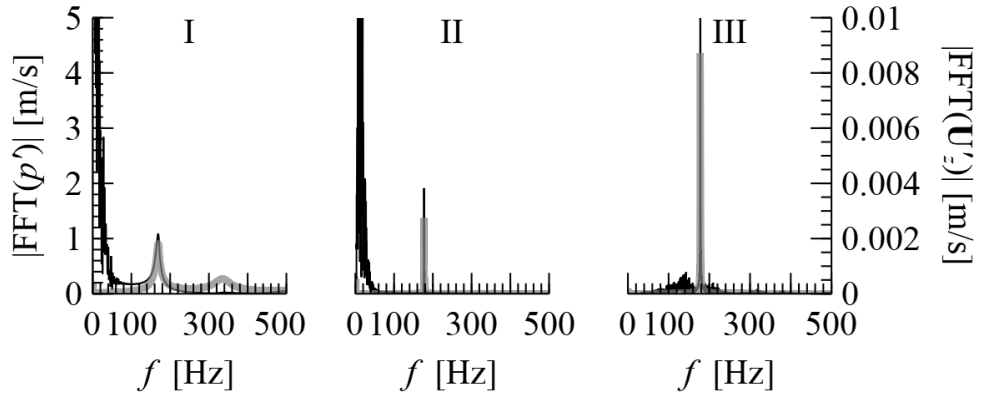

FIGURE 5.12: The frequency spectra of p' (thick grey line) and $\mathbf{U}'_z$ (thin black line) signals at $3L/4$ from the bottom end of the tube for the three distinct phases.

Likewise, similar trends are observed for the frequency spectra of p' in all phases. During phase I and II, the low frequency broadband is not detected in the pressure spectra as this is closely associated with the developing turbulence that has low acoustic pressure [93]. A higher frequency in the range of 300 Hz is observed in phase I, which is attenuated in the later phases. In phase III, the fundamental frequency is 177.75 Hz, which corresponds well with the theoretical fundamental first mode for a standing wave in a Rijke tube computed from [7],

$$f_0 = \frac{\sqrt{\gamma RT}}{2L} = 173.6 \text{ Hz} \, . \tag{5.14}$$

The standing wave can be obtained by modal decomposition of the pressure and velocity,

$$p'(\mathbf{x}, t) = \sum \hat{p}_\omega(\mathbf{x}) e^{i\omega t} \, , \tag{5.15a}$$

$$\mathbf{U}'(\mathbf{x}, t) = \sum \widehat{\mathbf{U}}_\omega(\mathbf{x}) e^{i\omega t} \, , \tag{5.15b}$$

where $\hat{p}_\omega(\mathbf{x})$ and $\widehat{\mathbf{U}}_\omega(\mathbf{x})$ are the modal complex decompositions. At the resonant frequency of 177.75 Hz, the acoustic pressure and velocity are obtained along the centerline and plotted in Figure 5.13. The plot shows that the fundamental wavelength is $2L$ as expected for an open-ended tube.

Investigation of the standard Rayleigh criterion is possible by plotting p', $\mathbf{U}'_z$, and $\dot{Q}'$ with time, as shown in Figure 5.14. The p' and $\mathbf{U}'_z$ are approximately 90° out of phase, while $\dot{Q}'$ and p' have a phase difference of 54.2°. According to these phase

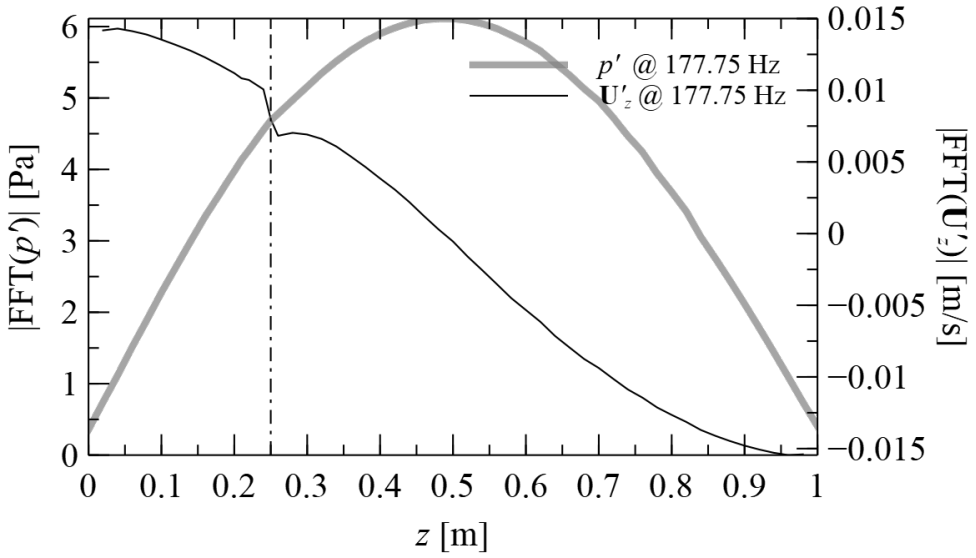

FIGURE 5.13: Pressure fluctuation (grey line) and axial velocity fluctuation (black line) amplitudes of the fundamental mode of standing acoustic wave established inside the Rijke tube. Frequency of the wave is 177.75 Hz, which corresponds to a wavelength of twice the tube length.

differences, the standard Rayleigh criterion for the generation of thermoacoustic instabilities has indirectly been satisfied.

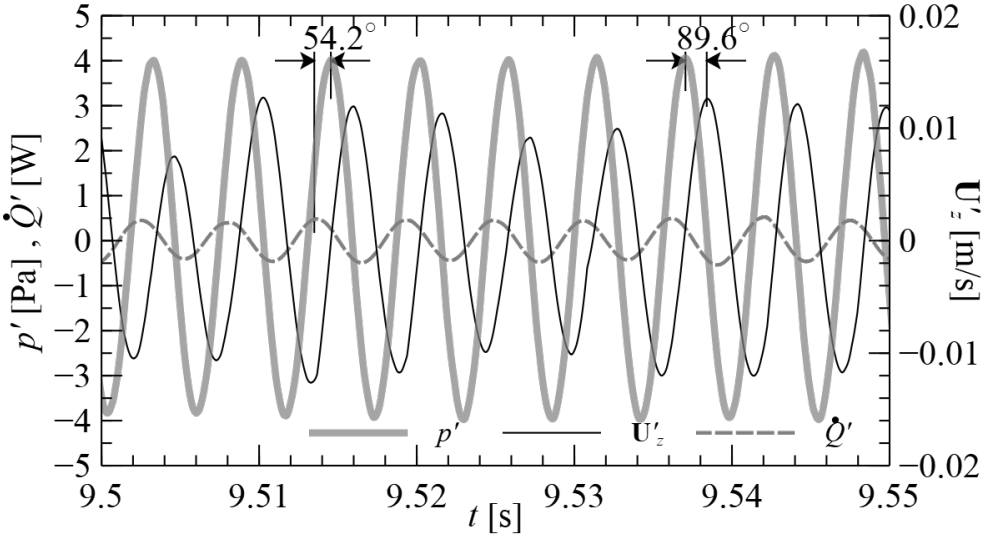

FIGURE 5.14: Time variation of the pressure fluctuation, p' (thick grey solid line), the axial velocity fluctuation, $\mathbf{U}'_z$ (thin black solid line), and the total heat release rate fluctuation, $\dot{Q}'$, (grey dashed line) at $3L/4$ from the bottom end of tube amid the repetitive phase III. Phase differences between p' and $\mathbf{U}'_z$ and between p' and $\dot{Q}'$ are 54.2° and 89.6°, respectively, indicating that p' and $\mathbf{U}'_z$ are out of phase to each other, while p' and $\dot{Q}'$ are in phase.

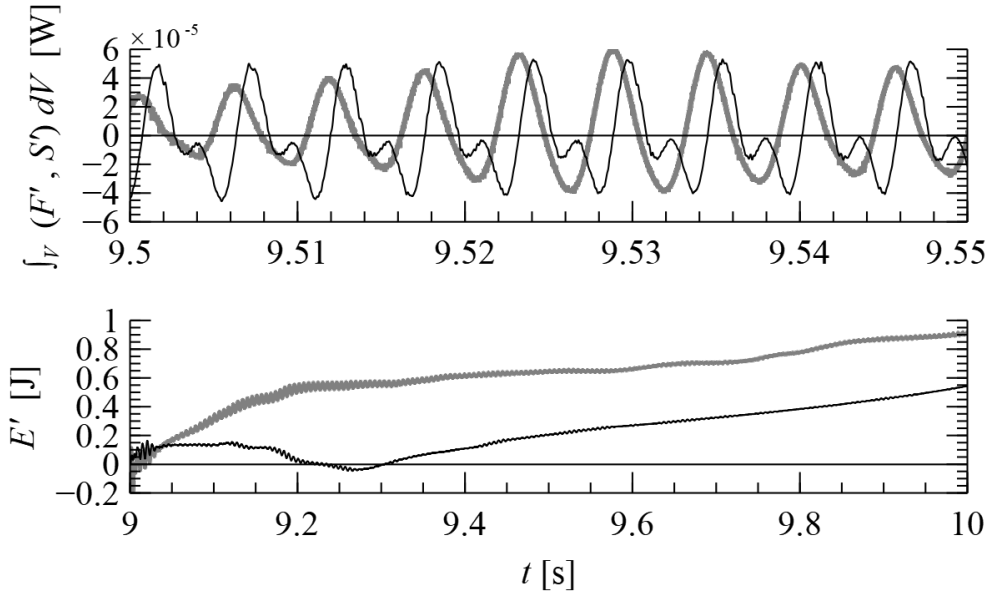

FIGURE 5.15: Evaluation of the standard and extended Rayleigh criteria for the non-combustion case with heater located at $L/4$ from the end of the tube. (Top) Acoustic loss term, F' (thin black line), and acoustic source term, S' (thick grey line), show a periodic nature of frequency of 177.75 Hz. (Bottom) Standard Rayleigh criterion, $\int E'_{std} dt$ (black line), and extended Rayleigh criterion, $\int E'_{exd} dt$ (grey line), increase to a positive value with time, indicating the generation of thermoacoustic instabilities.

This non-chemically reacting case was simulated to (i) validate the LES solver and (ii) assess the application of the standard and extended Rayleigh criteria. The acoustic loss, F' (thin black line), and acoustic source, S' (thick grey line), for 9.5 s $\leq t \leq$ 9.55 s are shown in Figure 5.15. The acoustic loss and source terms demonstrate a periodic nature with a frequency of 177 Hz. On average, the mean acoustic source term, $\overline{S'}$, and mean acoustic loss term, $\overline{F'}$ are 5.44×10^{-6} W and -3.78×10^{-6} W, respectively. Based on the bottom graph of Figure 5.15, the standard and extended Rayleigh criteria are both satisfied as $E'_{std} > 0$ and $E'_{exd} > 0$, respectively. This implies that both Rayleigh criteria accurately indicate the thermoacoustic phenomena. To further validate the numerical solver and assessment criteria, an additional case is conducted with the heater is placed at $3L/4$ from the bottom end of the tube. From [34], it is known that no thermoacoustic instability will occur for this configuration.

The assessment for thermoacoustic instability of this additional simulation is illustrated in Figure 5.16, for 5.5 s $\leq t \leq$ 5.55 s. The top plot shows $\overline{F'} = 4.79 \times 10^{-9}$ W and $\overline{S'} = -1.2 \times 10^{-10}$ W. Hence, for this configuration, $E'_{std} < 0$ and $E'_{exd} < 0$, confirming that no thermoacoustic resonance is possible. It also shows that both

the standard and extended Rayleigh criteria result in the same conclusion. As the LES solver and thermoacoustic processing tools have been validated, the cases for chemically reacting flow are presented as follows.

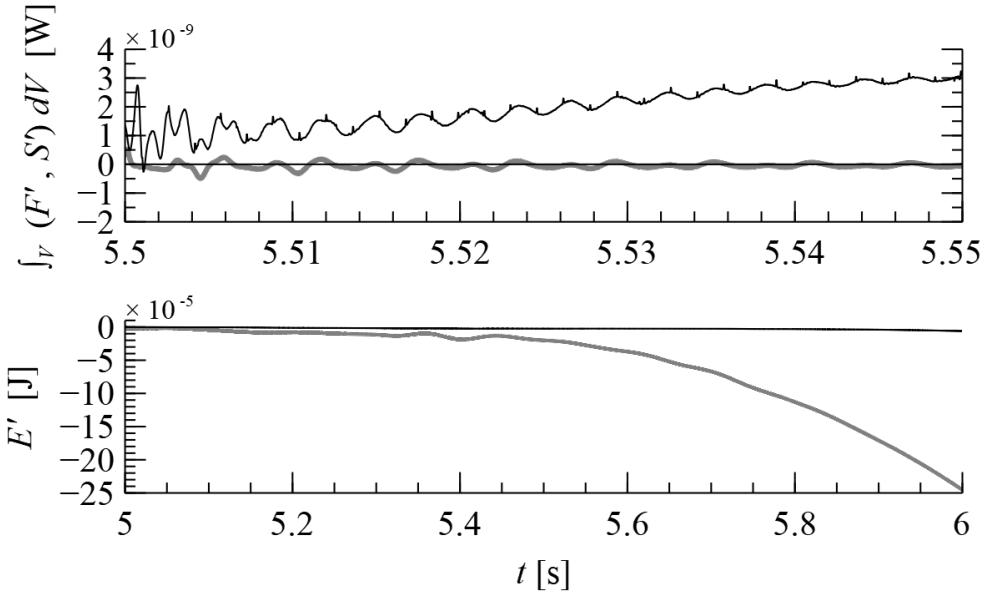

FIGURE 5.16: Evaluation of the standard and extended Rayleigh criteria for the non-combustion case with heater located at $3L/4$ from the end of the tube. (Top) Acoustic loss term, F' (thin black line), and acoustic source term, S' (thick grey line), barely show any periodic behavior. (Bottom) Standard Rayleigh criterion, $\int E'_{std} dt$ (black line), remains close to zero with time, whereas extended Rayleigh criterion, $\int E'_{exd} dt$ (grey line), decrease to a negative value with time, indicating no generation of thermoacoustic instabilities.

5.2.4 Combustion Rijke Tube Configuration

For the combustion Rijke tube simulations, a non-reacting jet was first injected from the Bunsen burner nozzle and ignited. The chemical reactions were incorporated by coupling either FPI or FPV combustion models with the LES flow solver for premixed and diffusion flame regimes, respectively, under the same fuel mass flow rate of 7.22×10^{-6} kg/s. The fuel composition used in the simulations is propane (C_3H_8), represented by a detailed mechanism [94] that contains 107 reactions and 31 species.

The instantaneous temperature contours for the three phases of combustion are illustrated in Figure 5.17 and Figure 5.18 for FPI and FPV cases, respectively. Qualitatively, both cases are similar. In transient phase I, a burst of high temperature formed instantly after ignition and was subsequently purged out of the

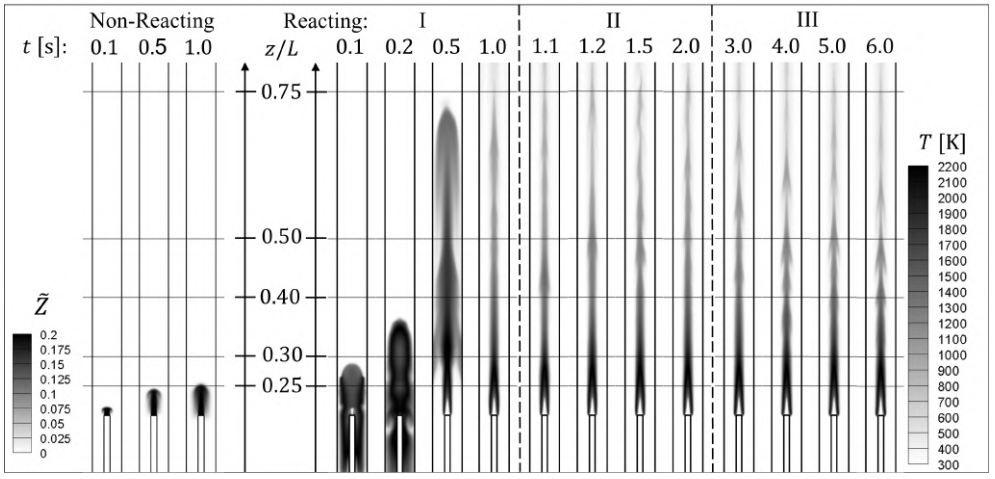

FIGURE 5.17: A series of snapshots from the FPI case shows two states: (i) the non-reacting state with the mixture fraction, $\tilde{Z}$ field and (ii) the reacting state with temperature field is categorized into three phases: (I) Ignition phase, (II) Transition phase, and (III) Repetitive phase.

Rijke tube in the form of a heat plume. In the transition phase II, the flame was more stable but had not yet developed a periodic pattern. Finally, in repetitive phase III , both premixed and diffusion flames reached a quasi-steady state. Some differences are noticeable between the two cases in terms of the flame length and temperature. The premixed flame initially extended to $z/L = 0.75$, and reduced to around $z/L = 0.5$ in phase III. The flame temperature at the Bunsen burner exit could exceed 2000 K. For the diffusion flame, the flame was short, almost indiscernible in phase II and III of Figure 5.18, with temperature as low as 700 K near the nozzle. Figure 5.19 presents the axial velocity, $\mathbf{U}_z$, at $z/L = 0.75$ along the centerline for both combustion cases. Specifically, the periodic velocity fluctuation is seen in phase III of the premixed flame only. In general, the premixed flame had a higher convective velocity, flame temperature, and longer, arrow-shaped flame with periodic response, while the diffusion flame was flat and had a lower flow velocity and temperature.

The statistical data from phase III such as mean heat release rate (HRR) and temperature are shown in Figure 5.20 for both FPI (left-half of contour) and FPV (right-half of contour) cases. Comparing both cases, two distinct mean HRR contours have been observed in the yz- and xy-planes. The convection is dominant in the FPI case, whereas diffusion is prevailing in the FPV case. These observations are expected as premixed combustion generally has a more concentrated local flame, whereas non-premixed combustion is driven by diffusion. The mean HRR

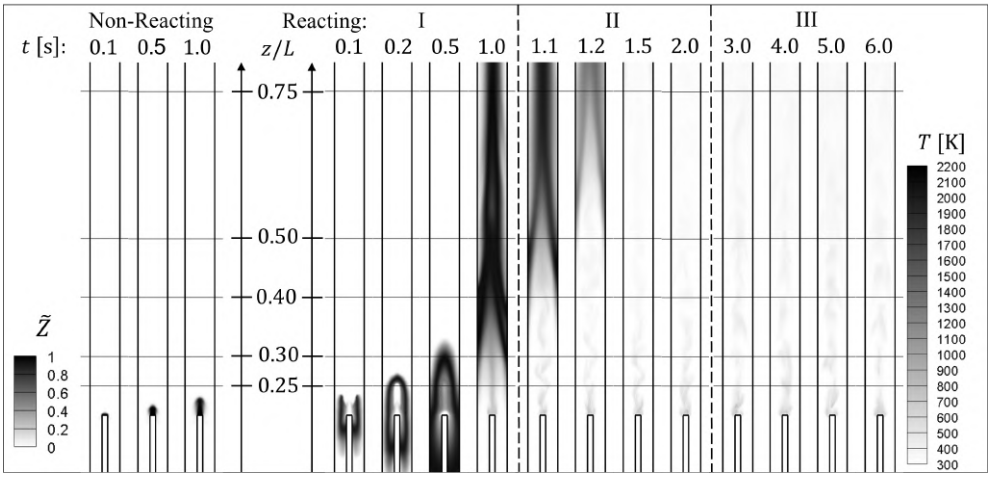

FIGURE 5.18: A series of snapshots from the FPV case shows two states: (i) the non-reacting state with the mixture fraction, $\tilde{Z}$ field and (ii) the reacting state with temperature field is categorized into three phases: (I) Ignition phase, (II) Transition phase, and (III) Repetitive phase

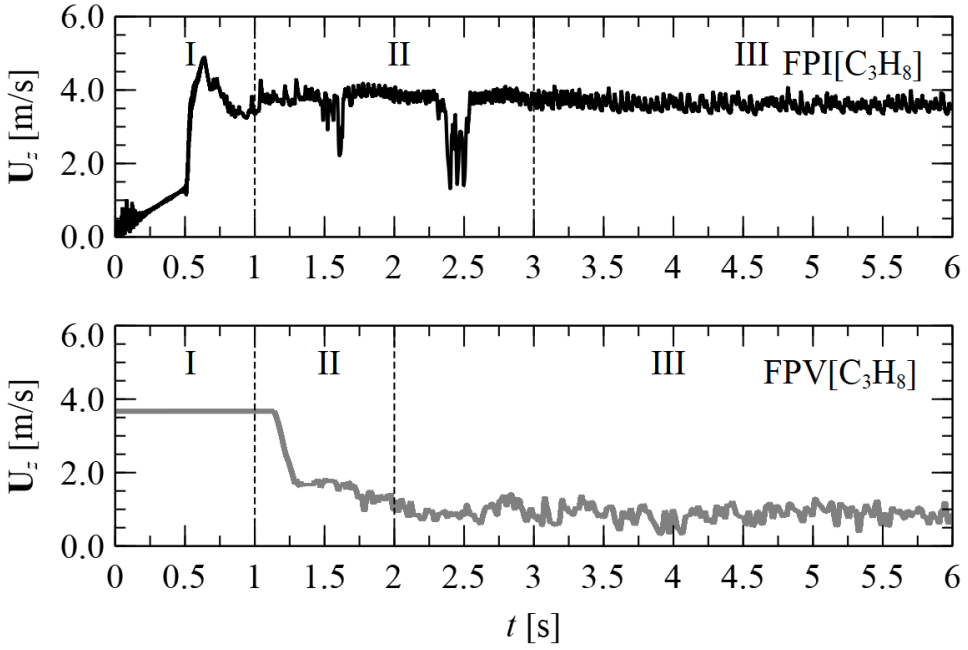

FIGURE 5.19: Comparison of the axial velocity, $\mathbf{U}_z$, at $3L/4$ from the end of the tube between both FPI and FPV cases. Three phases are observed, namely: (I) Ignition phase, (II)Transition phase, and (III) Repetitive phase.

of the FPI case shows two distinct reaction zones, forming two ring structures at $z/L = 0.21$ as illustrated in Figure 5.20. The outer reaction zone is attributed to the mixing process with the ambient air. The inner reaction zone has a conical shape and is responsible for most of the chemical reactions that will lead to a rapid depletion of reactants and generation of products. Compared to the FPI case, the

FPV is characterized by a low uniformly distributed mean HRR across the tube cross-section.

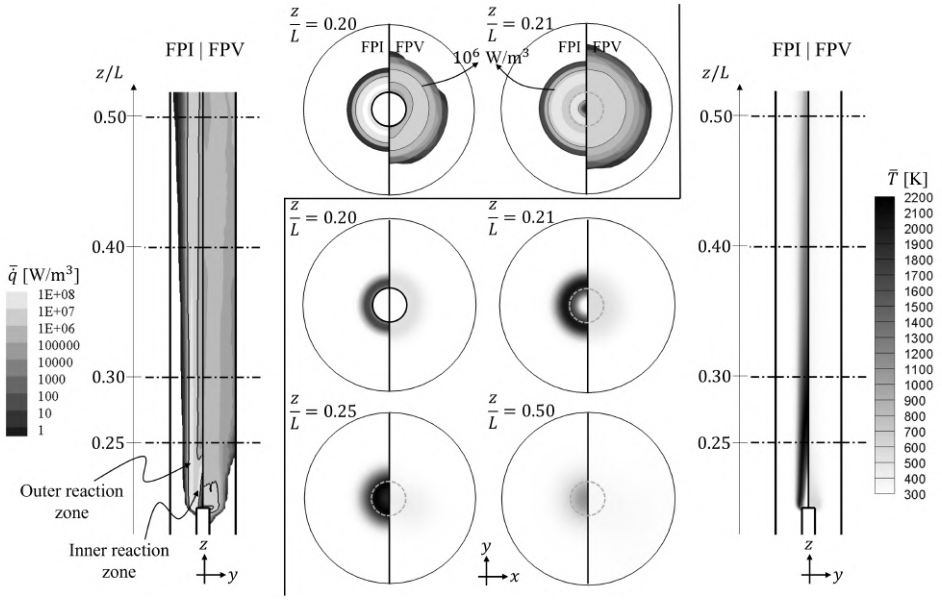

FIGURE 5.20: Illustration of the mean HRR, $\bar{\dot{q}}$, and mean temperature, $\overline{T}$, contours along the centerplane and various cross-sections along the tube. The mean HRR contour of FPI case shows a dominant convection effect and two reaction zones, while that of FPV case indicates the prevailing diffusive effect of non-premixed combustion. The mean temperature contours, $\overline{T}$, show that the FPI case has a lengthy and concentrated high temperature flame, while the FPV case has a distributed low temperature flame. The solid circle in the z/L planes indicates the location of the nozzle.

Figure 5.21 demonstrates the contour lines of the mass fraction of three species in the centerplane, namely propane, C_3H_8 (left), carbon dioxide, CO_2 (middle), and water vapor, H_2O (right). Note that the mass fraction of each species is normalized with its maximum value and the left and right side of the contours correspond to the FPI and FPV cases, respectively. For the fuel mass fraction, $Y_{C_3H_8}$, the FPI case shows a convection driven profile and thin reaction zone where the 0.1 and 0.9 contour lines are close to each other. These features indicate that the rate of fuel consumption is fast and takes place within a small region, which is consistent with the mean HRR contour in Figure 5.20. In contrast, the FPV case shows a uniformly flattened fuel profile, indicating that the diffusion of fuel is extremely dominant. For both cases, the Y_{CO_2} and Y_{H_2O} show high concentrations in the inner region of the flame where high mean temperature and HRR exist, which is expected.

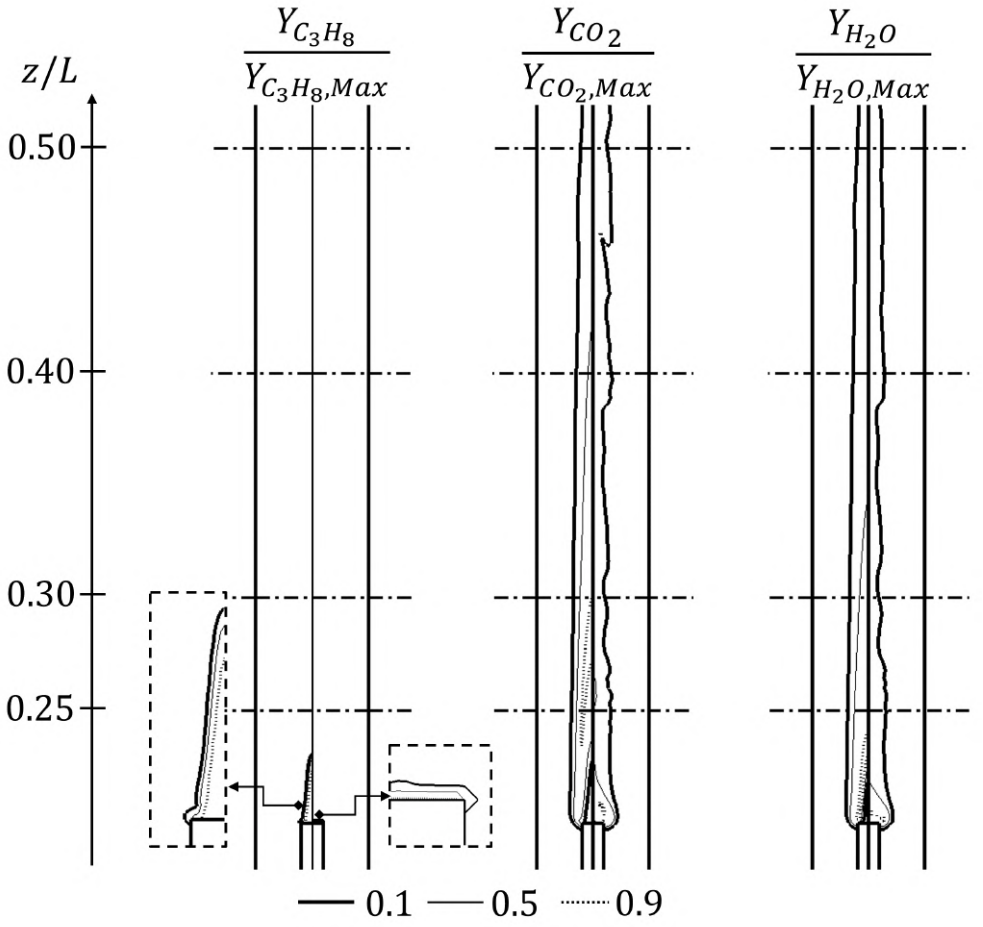

FIGURE 5.21: The normalized mass fractions of (left) C_3H_8, (middle) CO_2, and (right) H_2O, showing that the FPI case depletes fuel (C_3H_8) and generates products (CO_2 and H_2O) as the flow moves downstream, whereas the processes are mostly completed in the upstream region of the flow (near to the nozzle) for FPV case.

The radial distributions for both cases are plotted in Figure 5.22 in terms of the mean HRR, $\overline{\dot{q}}$, temperature, $\overline{T}$, mixture fraction, $\overline{Z}$, and progress variable, $\overline{C}$, for five axial locations at $z/L = 0.20, 0.21, 0.25, 0.50$, and 0.75. Black and grey lines represent FPI and FPV cases, respectively. The mean HRR of the FPI case is always in a higher order when compared to the FPV case at the same location. However, the FPI case tends to show a less diffused profile than the FPV case when moving downstream, which is consistent with the mean HRR contour plot illustrated in Figure 5.20.

Figure 5.22 also presents the mean temperature profile, $\overline{T}$, at different z/L locations. For the FPI case, the highest $\overline{T}$ is around quarter length from the bottom end of the tube (square marker), where $\overline{Z}$ is approximately at its stoichiometric

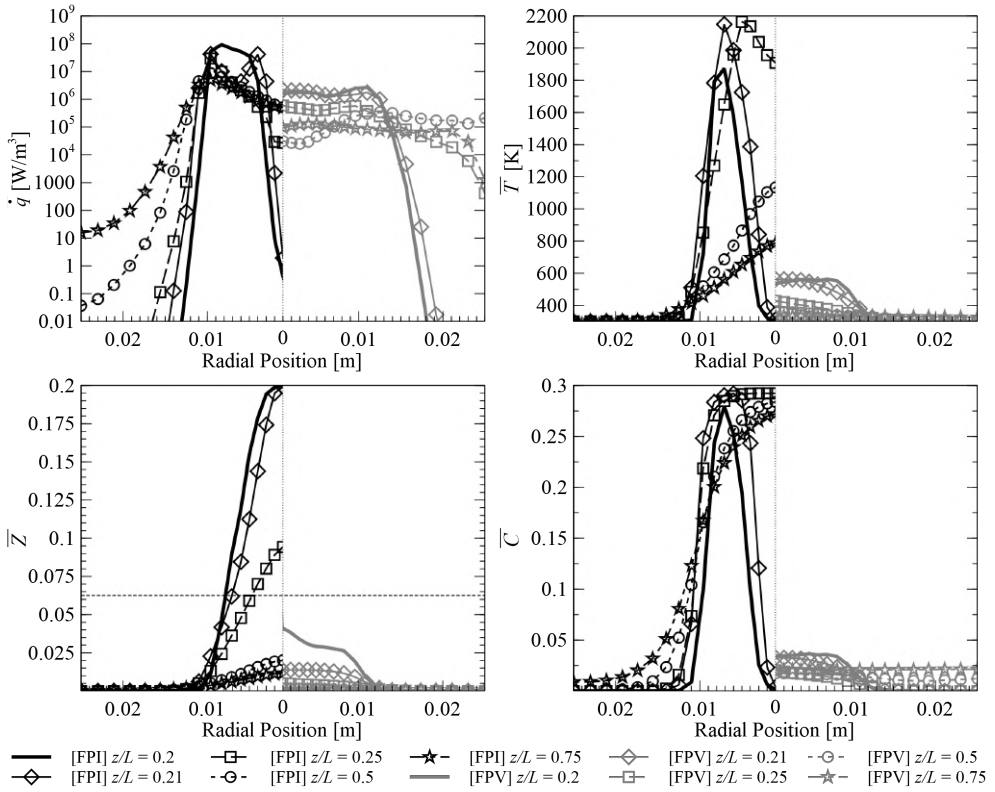

FIGURE 5.22: Illustration of the radial distribution of the (top-left) mean HRR, $\overline{\dot{q}}$, (top-right) mean temperature, $\overline{T}$, (bottom-left) mean mixture fraction, $\overline{Z}$, and (bottom-right) mean progress variable, $\overline{C}$, at different z/L. The dotted horizontal line in the $\overline{Z}$ plot indicates the stoichiometric mixture fraction of 0.065.

value of 0.0625 and $\overline{C}$ shows its maximum value. These $\overline{Z}$ and $\overline{C}$ values indicate that chemical equilibrium has been achieved. The FPV case shows its highest $\overline{T}$ is around 600 K near to the nozzle, together with a lean $\overline{Z}$ and low $\overline{C}$ due to the extremely diffusive flow.

The FFT spectra of p' and $\mathbf{U}'_z$ for both FPI and FPV cases are presented in Fig. 5.23 at $z/L = 0.75$ along the centerline. From the pressure data for the FPI case, the fundamental frequency is 148 Hz and the second mode at approximately 300 Hz is also present. The frequency response for $\mathbf{U}'_z$ also shows a dominant frequency of 148 Hz, as well as the presence of turbulence at lower frequencies (< 200 Hz). This lower frequency response is associated with the convected flow that has low acoustic pressure for non-uniform flows [93].

For the FPV case, the p' spectrum shows a wider frequency content compared to the FPI case. Specifically, the first three harmonic frequencies have comparable magnitude. There is also a discernible low amplitude broadband noise at higher

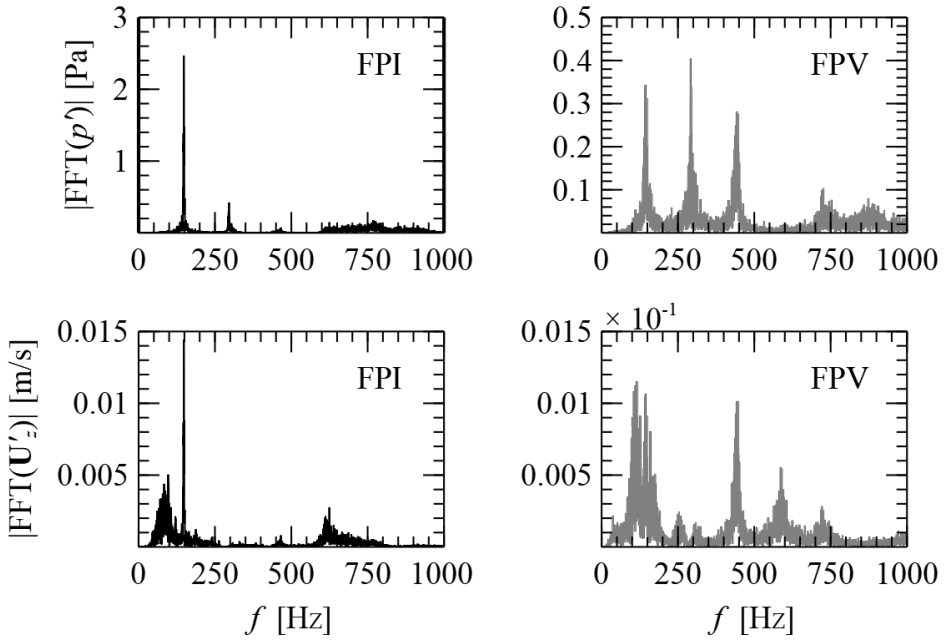

FIGURE 5.23: Comparison of the FFT spectra of the (left column) FPI and (right column) FPV cases. Both the pressure, p', and axial velocity, $\mathbf{U}'_z$, were sampled at $3L/4$ from the end of the tube with a sampling rate of 100 kHz. Note the different $y-$axis scales between the two cases.

frequency (> 600 Hz), which is a characteristic of diffusive flows. The $\mathbf{U}'_z$ spectrum has a similar trend as the p' spectrum where multiple harmonic frequencies are observed and the spectra indicate significant turbulence and diffusion.

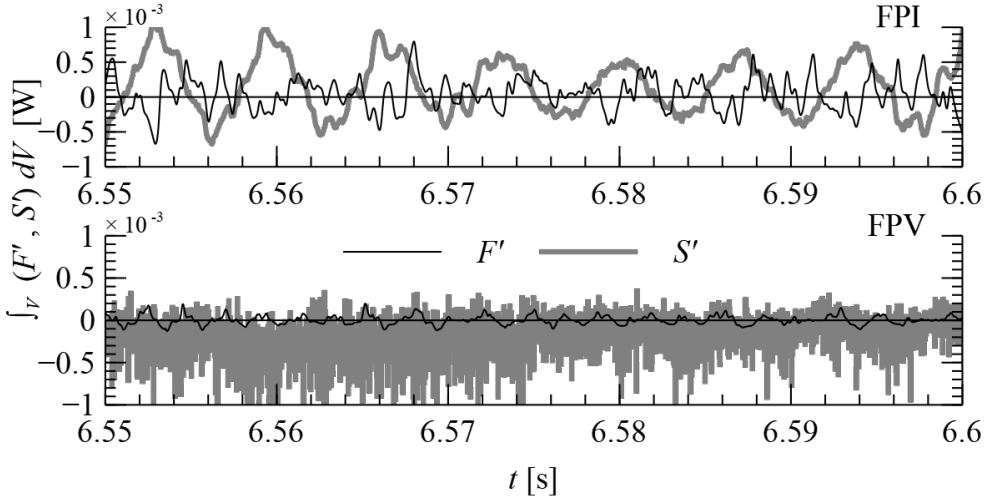

FIGURE 5.24: The acoustic loss, F', and acoustic source terms, S', of the (top) FPI and (bottom) FPV cases.

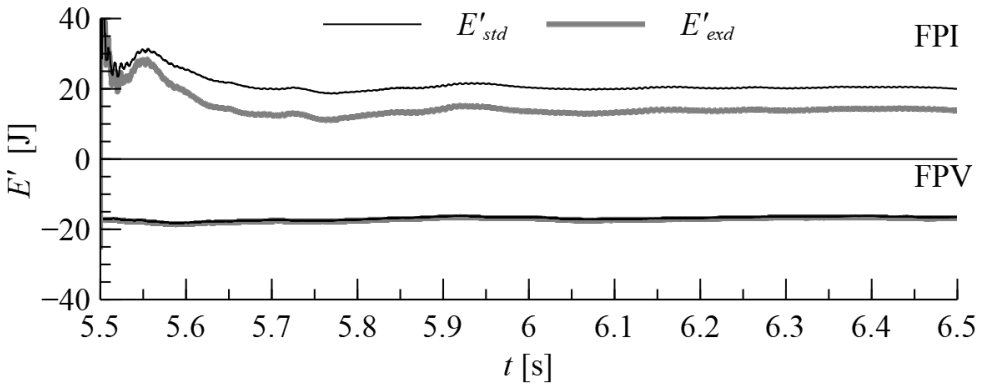

FIGURE 5.25: Acoustic energy budget, E', obtained from the repetitive phase of (upper half) FPI and (lower half) FPV cases.

As both FPI and FPV cases exhibit tonal fundamental frequencies, thermoacoustic instability must be assessed with the standard and extended Rayleigh criteria. Figure 5.24 presents the F' (thin black line) and S' (thick grey line) terms for 6.55 s $< t <$ 6.6 s. The FPI case, as illustrated at the top graph of Figure 5.24, shows that both F' and S' are in the same order. The FPV case (bottom graph of Figure 5.24) depicts a negative mean for S' and approximate zero mean for F'. The acoustic energy budget, E', is plotted in Figure 5.25 for both the standard and extended Rayleigh criteria. Clearly, both criteria predict that only the premixed combustion will result in thermoacoustic instability, whereas the diffusion flame does not. Hence, the standard Rayleigh criterion is sufficient to perform the assessment for thermoacoustic instability.

5.2.5 Comparison with Experiments

Two combustion Rijke tube experiments [95] were conducted using LPG to generate premixed and diffusion flames, which correspond to the FPI and FPV simulations discussed in Sec. 5.2.4, respectively. During the experiment, a resonating tone was recorded when a premixed flame was used, whereas no audible sound was observed for the diffusion flame. Therefore, for the premixed case, pressure fluctuations were collected by microphones and compared with the FPI results.

Figure 5.26 compares the normalized FFT spectra of the experiment and simulation of premixed flames. In terms of the fundamental frequency, the experiment and FPI simulation measure 154.7 Hz and 148 Hz, respectively, which is a difference of approximately 4.3%. The discrepancies between the two datasets could be

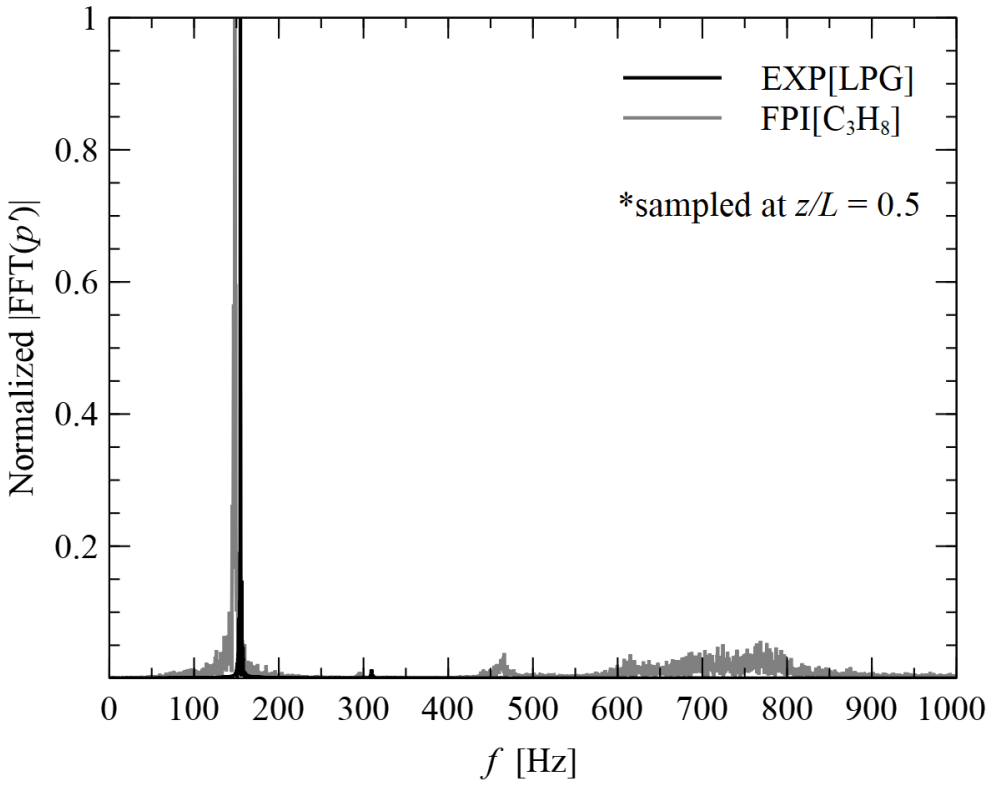

FIGURE 5.26: Comparison of the FFT spectra of normalized p' from experiment (black) and FPI (grey) simulation. Note that the fuel in the experiment is LPG while in the FPI simulation is propane, C_3H_8.

attributed to a lack of information about the mixture exit velocity and the net mass flow rates out of the Bunsen burner nozzle, as well as the different types of fuel used in the experiment and simulations. The qualitative agreement between the two datasets is encouraging, verifying that the LES solver implemented in this work has the potential to capture thermoacoustic effects.

Table 5.2 compares the experimental observations from reference experiments and the instability predictions results of all simulations from both assessment criteria. Clearly, both standard and extended Rayleigh criteria predictions are consistent with the measurements and cited literature. Table 5.2 also confirms that the standard Rayleigh criterion is sufficient to predict thermoacoustic instability for the Rijke tube configuration.

TABLE 5.2: The observations and assessments of thermoacoustic instability.

Types	Cases	Standard Rayleigh	Extended Rayleigh	Literature or Experiment
Non-combustion with heater	$L/4$	Yes	Yes	Yes [34]
	$3L/4$	No	No	No [34]
Combustion	FPI	Yes	Yes	Yes
	FPV	No	No	No

5.3 Summary

To sum up, the DDT has successfully extended to 3D with condition. A constant and high overlap ratio $R \geqslant 5$ is required for this isothermal turbulent jet DDT simulation to work well. Despite of that, 16% reduction of computational hours by DDT simulation has reported showing the computational advantage of DDT over fully nonlinear simulation. The thermoacoustic nonlinear LES solver has accurately predicted the theoretical resonance frequency of Rijke tube simulations. Implementation of standard and extended Rayleigh criteria, to evaluate the thermoacoustic instability in numerical results, is correctly done for heater and reacting flow as heating sources. Observations of experiment with flames suggest both combustion models are properly implemented, also further affirmed by Rayleigh criteria assessments. The standard Rayleigh criterion is found to be sufficient in examine the thermoacoustic instability, which suitable for physical experiments based evaluation. Overall, the developed LES solver coupled with combustion models has confirmed its capability in capturing the acoustic generation by thermoacoustic instabilities.

Chapter 6

Conclusion and Future Work

6.1 Conclusion

The aim of this dissertation is to develop a high-fidelity numerical method that is able to resolve acoustic waves effectively in terms of wave propagation over long distance, wave scattering and noise generation. The problem requires a nonlinear solver to solve for complex flow features, such as shock and turbulence, and linear solver for acoustic propagation. Therefore, the research works are divided into two parts: (i) extending domain decomposition technique (DDT) to higher dimensionality for solving more complex and engineering practical problems and (ii) developing high-fidelity nonlinear solver such that the acoustic generation process can be predicted accurately.

First, effort was placed to demonstrate the generality of DDT in higher dimension applications. Extension of DDT to 2D has been validated with 1D and theoretical solutions. The explicit filter scheme is implemented to eradicate the artificial spurious waves generated while acoustic waves crossing the overset boundary. 2D inviscid and time-invariant mean flow cases with different types of flow conditions are simulated using DDT to show its generality. Acoustic wave transport in converging-diverging nozzle, a typical internal flow case that emulate engine exit nozzle, was conducted since the flow regimes can be easily adjusted from subsonic to supersonic by modifying the pressure ratio. The simulation results have shown the effectiveness of DDT in preventing reflections from boundary and saving the

computational hours up to 84% and 51% for subsonic and supersonic flow regimes, respectively.

To mimic the propagation of engine noise over wing, the interaction of acoustic wave with solid body was examined. This external flow application is done by scattering the point and periodic acoustic waves over a supercritical airfoil under subsonic and transonic flow regimes. The simulation results proved that DDT can eradicate the numerical noise presented in nonlinear far-field region. Additionally, higher overlap ratio, $R \geqslant 4$, defined as the ratio between size of linear to nonlinear cells, is encouraged for all 2D DDT simulations. This is because both internal and external flow cases have demonstrated that higher R not only provides computational saving, but also helps in minimizing the reflection from the interface between linear and nonlinear regions as well as preserving acoustic wave in finer nonlinear domain due to lesser dissipation and dispersion errors.

For a preliminary study of thermoacoustic topic and gain insight of acoustic and entropy wave interactions, a convection driven thermal plume is studied. Point and periodic acoustic sources are introduced inside the linear region to study the interactions with the heater and vortex shedding downstream of the heater. The simulation results show the acoustic wave and density perturbation scattered around the cylindrical heater, as expected. The propagation of density perturbation is barely observed at the downstream of heater due to the dominance of vortex shedding. Nonetheless, for periodic acoustic source, the FFT analysis of heat release rate by the heater is found to have two dominant frequencies, the vortex shedding frequency and the periodic acoustic source frequency, indicating the successful coupling of two domains by DDT and the feasibility of DDT in thermoacoustic problem.

Extension of DDT to 3D application was attempted to study the acoustic wave generation from a turbulent jet. The inner nonlinear domain is conducted using large-eddy simulation (LES) such that high-fidelity solutions can be obtained. The converged fully nonlinear isothermal jet simulation describes the need of microsecond timestep to capture the turbulent jet noise accurately. The corresponding DDT simulation shows spurious oscillations at the linear/nonlinear interface which can be solved by using constant overlap ratio. In addition, the time-varying mean issue in DDT simulation can be solved by increasing the overlap ratio. Again approximately 16% reduction of computation time by DDT demonstrated its advantage over fully nonlinear simulation, but not without caveats.

In second part of this research, two combustion models of tabulation type have been successfully coupled with the high-fidelity multi-dimensional compressible LES solver. The simulation results on a subsonic Rijke tube configuration agree quantitatively with the experimental observation for both diffusion and premixed flames in terms of resonance frequency. This achievement confirms that LES coupled with flamelet-progress variable (FPV) or flame prolongation of intrinsic low-dimensional manifold (FPI) combustion models has the potential to predict the fundamental thermoacoustic effects, such as combustion instabilities. This approach, hence, can be utilized as a predictive tool for flame-generated thermoacoustic simulations. Thereafter, a deep study about the effectiveness of the standard and extended Rayleigh criteria to assess the generation of thermoacoustic instability have been evaluated. In essence, the standard Rayleigh criterion considers only the acoustic source term, while the extended Rayleigh criterion accounts also for an acoustic loss term and its balance with the source term for the definition of the acoustic energy term. If the accumulative integration of the acoustic energy term with time is positive, then thermoacoustic instability will be present, and vice versa.

To verify the two assessment criteria, they are applied in this work for a baseline non-combustion (heater) and combustion (premixed and diffusion flames) Rijke tube configurations. For the baseline case, two simulations, one with heater at the quarter tube length and the other at the third-quarter tube length, were conducted. As expected from literature and predicted by both assessment criteria, only the quarter length simulation generated thermoacoustic sound. Hence, the feasibility of the LES solver is verified and the applicability of the standard and extended Rayleigh criteria is demonstrated. The simulation results of the combustion cases demonstrate the suitability of the FPV and FPI combustion models to capture the different characteristics of the diffusion and premixed flame regimes, respectively. In addition, the study shows that only the premixed case will generate thermoacoustic instabilities, which is in agreement with the assessment by the two Rayleigh criteria and qualitatively aligned with experiment observation. The results suggest that both versions of Rayleigh criteria are able to assess thermoacoustic instability, regardless of the heat source. This finding is important because the standard Rayleigh criterion, despite being a simplified version of extended Rayleigh criterion by omitting the acoustic loss term, is the only assessment possible with physical experiments.

Overall, the 2D DDT applications have demonstrated the feasibility of DDT for acoustic wave scattering and propagation over a solid body and a wide range of inviscid flow regimes even with the existence of shock wave and non-isothermal viscous flow. The 3D DDT application was attempted and has shown potential for 3D, but not without caveats. High-fidelity acoustic generation simulations were performed and are able to correctly predict the acoustic or thermoacoustic instability formation by using the developed nonlinear solvers, integrated with the combustion models.

6.2 Future Work

To improve the DDT performance in 3D simulations, the time-varying mean and interface problems need to be resolved. Also, adopting DDT for the thermoacoustic or non-isothermal case is also one of the areas worth studying. Taking a Rijke tube configuration as one of the applications, as illustrated in Figure 6.1, DDT can be modified such that its inner nonlinear domain (labeled as 'INL') will coarsen to domain boundary (labeled as 'NL') and fully overset with linear domain (labeled as 'L'). By doing so, the nonlinear domain boundary can be taken care of to avoid any reflections as observed in turbulent jet DDT simulation. A interface boundary will be constructed between the inner nonlinear and linear domains where the primitive variables are coupled to propagate their corresponding small perturbations into the linear region.

To evaluate the method's feasibility, the studying should be to start simple, using 2D setups with non-reacting heaters as the main heating source for Rijke tube DDT simulations. Thereafter, the heater can be replaced with reacting flows, for which building the preliminary study of more complex problem.

By utilizing the dynamics mesh method in the nonlinear domain, DDT may extend its feasibility in studying of non-reacting/reacting flow case but with moving complex geometry that generates vortical waves and acoustic waves, such as the simulation of combustion noise/instabilities propagate into engine turbine section and further interact with turbine blades.

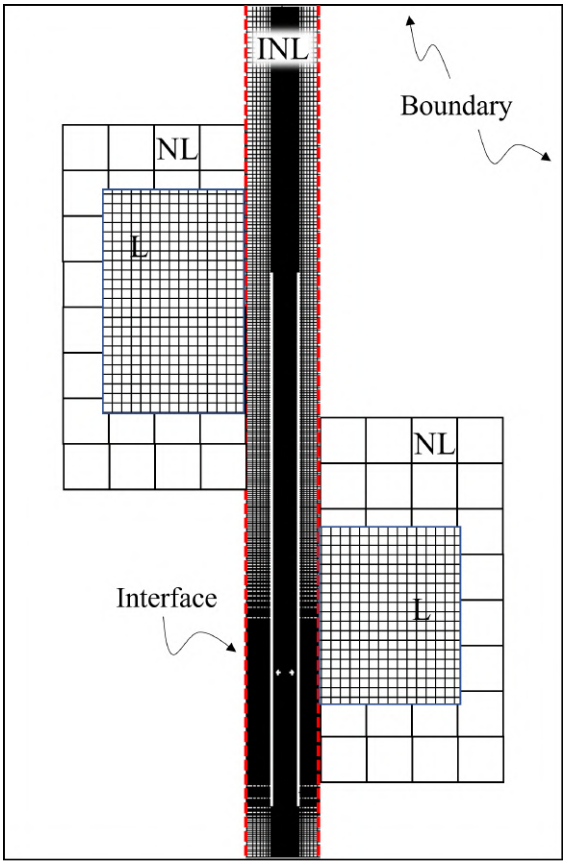

FIGURE 6.1: A schematic diagram of Rijke tube simulation using DDT method.

Appendix A

Experimental Measurement of Isothermal Turbulent Jet

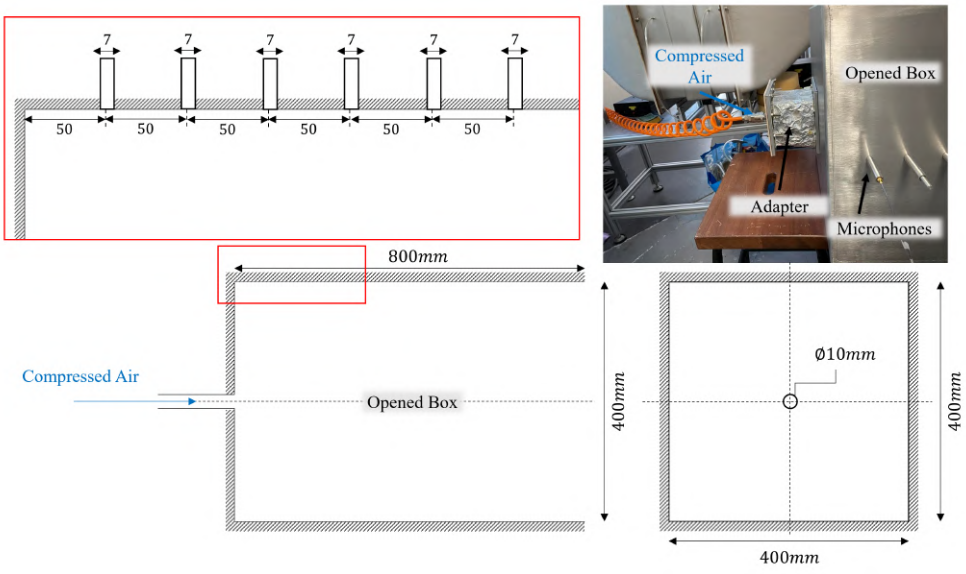

FIGURE A.1: Schematic drawing of the experimental setup.

This section discusses the isothermal turbulent jet noise experimental measurements and compares to its corresponding numerical simulation for validation and completing the research project related to turbojet engine. The experimental rig is shown in Figure A.1 together with its schematic drawing and dimensions. Adapter was used to connect the compressed air outlet and the aluminum box with one face opened (outlet) and jet inlet hole of 10 mm diameter. One of the four side walls was installed with 15 microphone holes, each 50 mm apart. At any time, only

five of these holes will be used simultaneously as there are only five microphones available, while the rest will be sealed. The pressure measurements were sampled at frequency of 20 kHz, using PXIe-1062Q data acquisition system equipped with a PXI sound and vibration module NI PXIe-4498 and B&K DeltaTron Pressure-field 1/4″ microphone type 4944B. Data were then collected and performed FFT to compare with numerical solution as shown in Figure A.2.

The corresponding fully nonlinear simulation was conducted to validate the solver. Although the current case has a different boundary condition (four surrounding walls) than the open turbulent jet in Section 5.1, same mesh resolution (cf. Figure 5.1) was used with smaller dimension which matching with the experimental setup. The turbulent jet profile was obtain and validated with theoretical solutions. Vary mean issue as reported in Section 5.1.2 was observed as well for pressure perturbation contour. This may be the reflection coming from the side walls. Besides, the pressure field at one side wall was sampled at frequency of 1 MHz for comparison with experimental measurements.

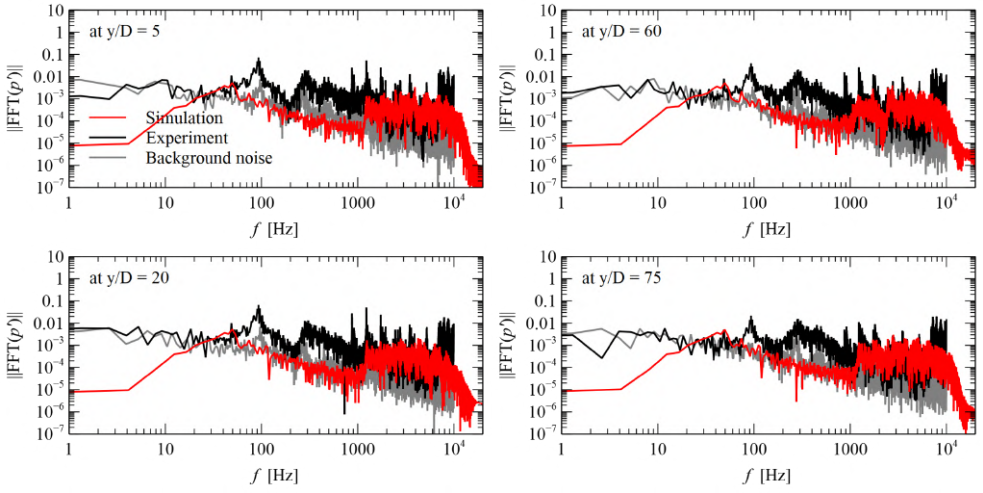

FIGURE A.2: Ensemble-averaged FFT spectra of p' of experiment and simulation.

The ensemble-averaged experimental and simulation FFT spectra are compared in Figure A.2. In low frequency range ($<$ 100 Hz), the experimental measurements show higher amplitude compared to simulation, which may be attributed to noise in the background considering the similarity between the measurements made with the jet on (black line) and jet off (grey line). A background tone of approximately 100 Hz is believed to be present during the experiments and get amplified by the

turbulent jet, though the reason is still unknown. In general, the broadband turbulence in the simulation is reasonably validated by the experimental measurements from their agreement in: (i) the slope of the spectrum and (ii) the amplitude range between 1 kHz to 10 kHz. Despite of that, comparing the high frequency range (10 kHz), the amplitude discrepancy indicates the excessive numerical diffusion incurred in simulation, that is not present in physical space. This discrepancy from the simulation highlights the value of domain decomposition technique, which has the characteristic to preserve acoustic waves over long distance by design.

Appendix B

Applications of OpenFOAM Solver Developed for PhD

B.1 Laminar Jet

Two-dimensional laminar free jet is done for preceding study of turbulent free jet. The computational domain for DDT simulation is presented in Figure B.1. Same configuration and mesh resolution were used for fully nonlinear simulation without the linear and sponge zones. A tube with diameter, $D = 0.04$ m, and length of 1 m is used to generate the laminar jet with average exist velocity of 0.01167 m/s at Reynolds number of $Re = 30$. No slip condition was applied to the tube wall. Isothermal jet ($T = 300$ K) was considered with ambient temperature, $T_\infty = 300$ K and pressure, $p_\infty = 1 \times 10^5$ Pa. Ideal gas law was assumed. For fully nonlinear simulation, CFL was maintained at 0.3 until the accomplishment of statistical mean collection. Since the mesh resolution is similar to the mesh used in Section 4.4, same time step, $\Delta t = 1 \times 10^{-6}$ s was considered for simulating propagation of wave in both fully nonlinear and DDT simulations.

Upon the collection of statistical mean fields, the normalized velocity field is shown in the left contour plot of Figure B.2. The laminar jet is ejected from the tube nozzle located at $y/D = 0$ and spreading downward. In top graph of Figure B.3, the jet velocity decaying profile along axis-symmetric line is plotted in log-scale at $x/D = 0$ and compared to analytical solution (B.1). The half-value width jet of simulated laminar jet (middle graph in Figure B.3), defined as the distance of

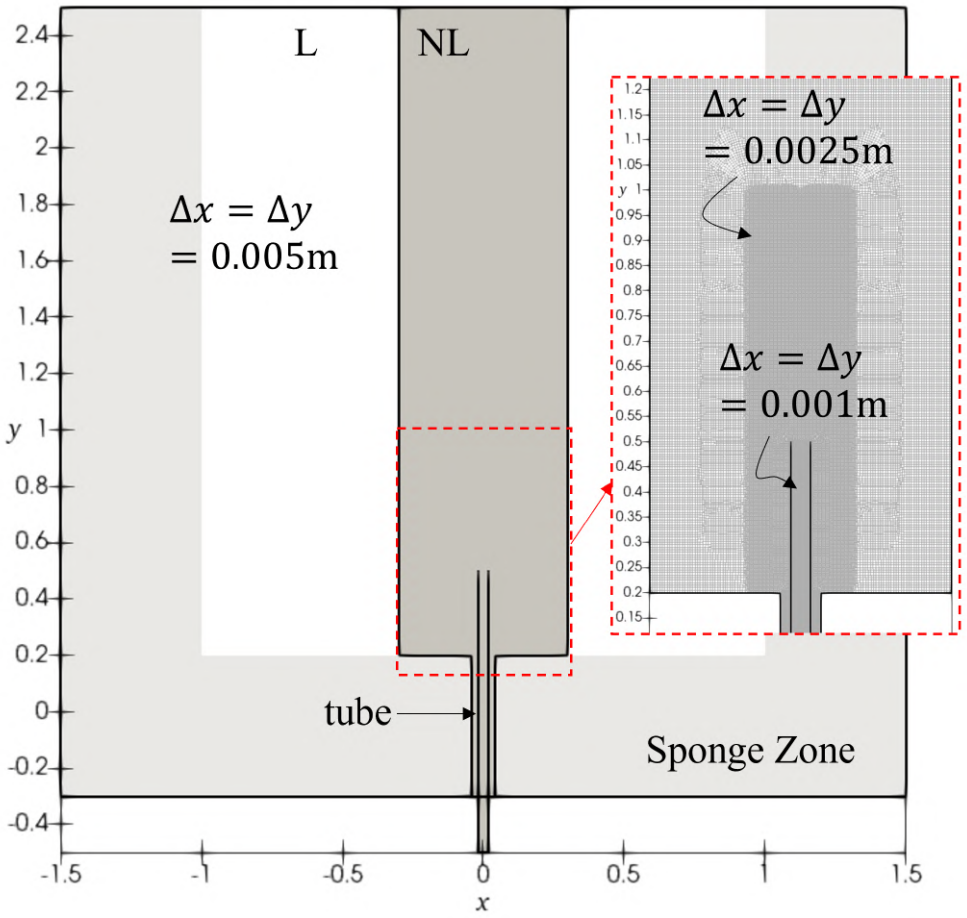

FIGURE B.1: Mesh resolution of the computational domain for 2D laminar jet simulation. Dark grey region represents nonlinear (NL) region, whereas, light grey region indicates the sponge zone.

the points with half the maximum jet velocity is compared with analytical solution (B.2) as well. Although the jet decaying profile was not quantitatively matching with the analytical result, but it follows the trend. In term of the jet width, the simulation result agreed well. Moreover, the bottom graph in Figure B.3 describes the laminar jet reached its self-similarity in the far-field ($y/D > 20$). All the analytical solutions [96] are defined as follow: (i) the jet decaying profile for jet with $Re < 30$,

$$v = 0.4543\left(\frac{K^2}{\nu y - 2D}\right)^{1/3}, \; V = \frac{K}{48\nu}, \tag{B.1}$$

where V and D are the reference velocity taken as the velocity at the tube nozzle and nozzle diameter, respectively; (ii) the half-value width of the laminar jet,

$$x_{0.5} = 3.2\left(\frac{\nu^2}{K}\right)^{1/3} y^{2/3}; \tag{B.2}$$

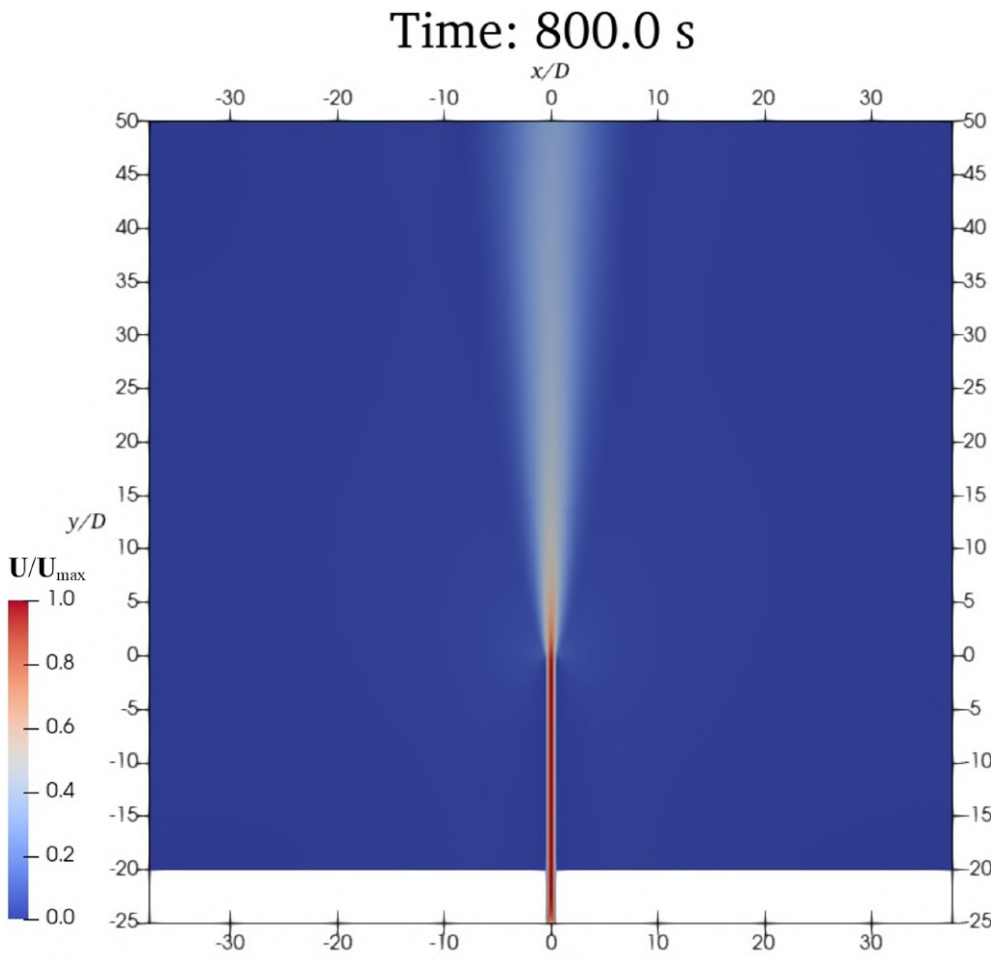

FIGURE B.2: Normalized velocity magnitude contour of laminar jet.

(iii) the self-similarly of the jet can be described as Gaussian profile,

$$v = e^{-\ln 2 y^2} \ . \tag{B.3}$$

A half sinusoidal pressure perturbation, p', was sent into the tube and propagating out. The perturbation is defined as,

$$p' = \epsilon sin(2\pi f t) \ , \ \text{for} t < \frac{1}{2f} \tag{B.4}$$

where frequency, $f = 1000$ Hz and $\epsilon = 100$ Pa. A sequence of p' contours for both (first column) fully nonlinear (NL) and (second column) domain decomposition (DD) simulations is illustrated in Figure B.4 for time of (a) $t = 0.004$s, (b) $t = 0.006$s, (c) $t = 0.008$ s, and (d) $t = 0.01$s. A reflecting wave (marked as **A** in Figure B.4) was observed in fully nonlinear simulation but not in DDT simulation.

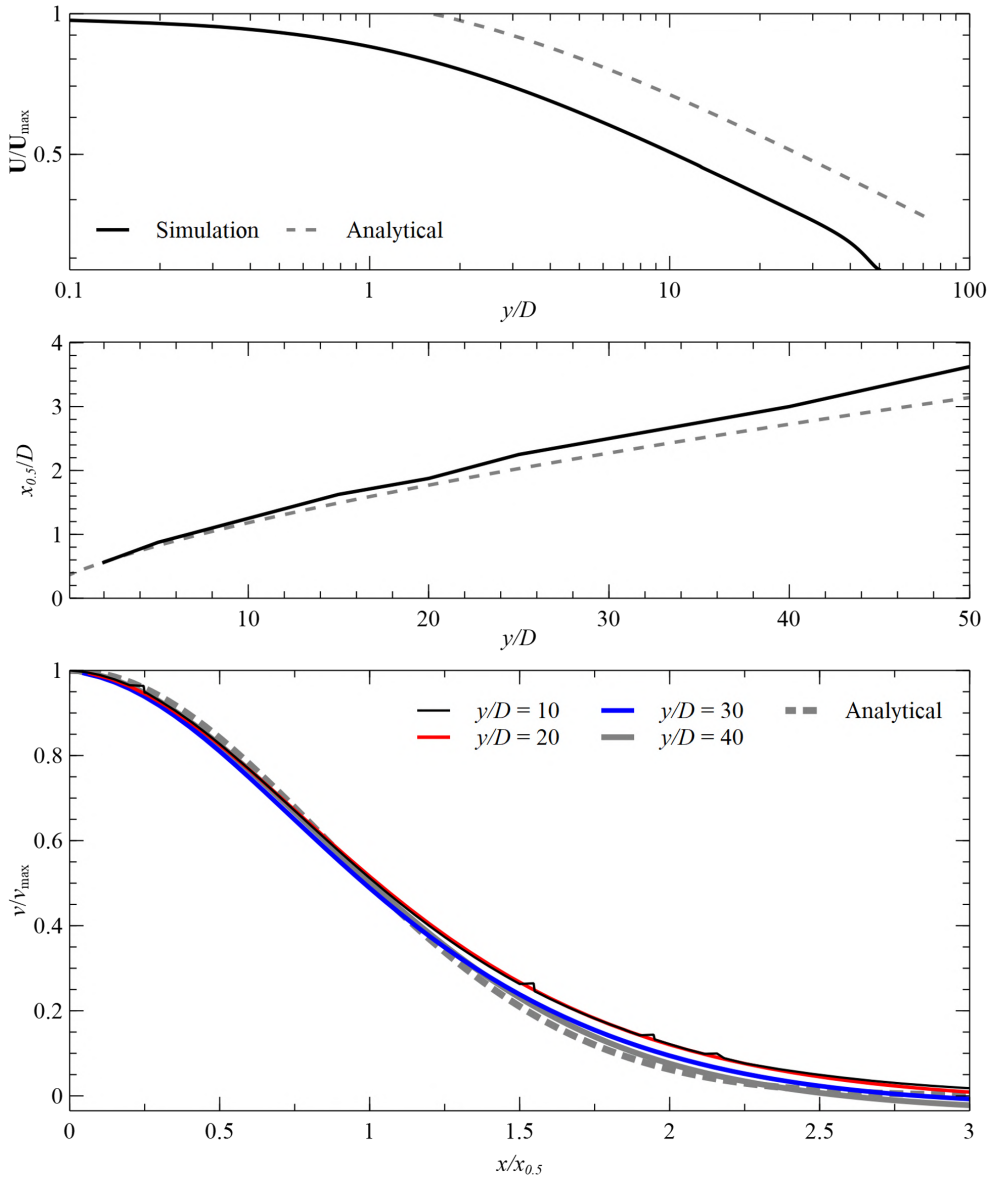

FIGURE B.3: Comparison between simulation (solid line) and analytical results (dashed line) for (top) centerline jet velocity profile, (middle) half-value width jet, and (bottom) self-similarity of the jet.

due to the existence of the sponge zone. Quantitatively, axisymmetric line is plotted to compare both simulations as presented in the right column of Figure B.4. Same observation is noticed. This has proven that the construction of the linear and nonlinear regions in DDT simulation is vital. A well segregated computational domain helps to eliminate the reflections and preserve the waves.

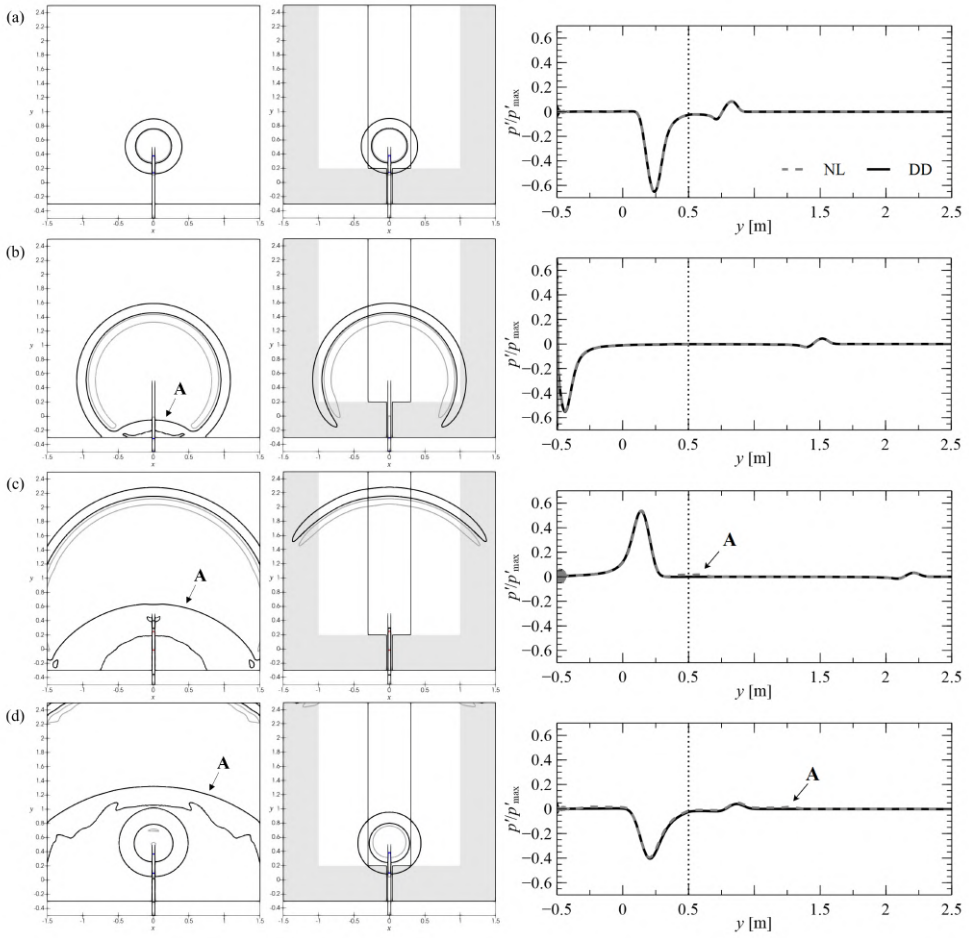

FIGURE B.4: Comparison of the plane wave propagation from tube between fully nonlinear (NL) and domain decomposition (DD) simulations. Shaded region is the sponge zone, dotted line in the plots represents the location of tube nozzle.

B.2 Non-Isothermal Turbulent Jet Noise

For the interest of acoustic, vortical and entropy wave interactions, additional two heated jet simulations were conducted at temperature of $T = 600$ K and $T = 900$ K which represent typical compressor exit range and turbine inlet range, respectively. Same computational domain that used in the isothermal jet simulation (see Section 5.1) was used in both heated jet simulations. Nonetheless, the inlet velocity of each simulations was defined such as the Reynolds number ($Re \approx 10^4$) is matching with the isothermal jet simulation. The inlet velocity values were then set as 53.0296 and 102.777 m/s for $T = 600$ K and 900 K, respectively. The initial conditions, however, were remain the same as the isothermal simulation, where the ambient pressure, p_∞, and temperature, T_∞, were 1 bar and 300 K, respectively. Since the air temperature is expected to change in wide range, JANAF

thermodynamic tables were used to calculate C_p, Sutherland model were applied to obtain the dynamics viscosity of air, μ, and lastly the ideal gas law was assumed for equation of state.

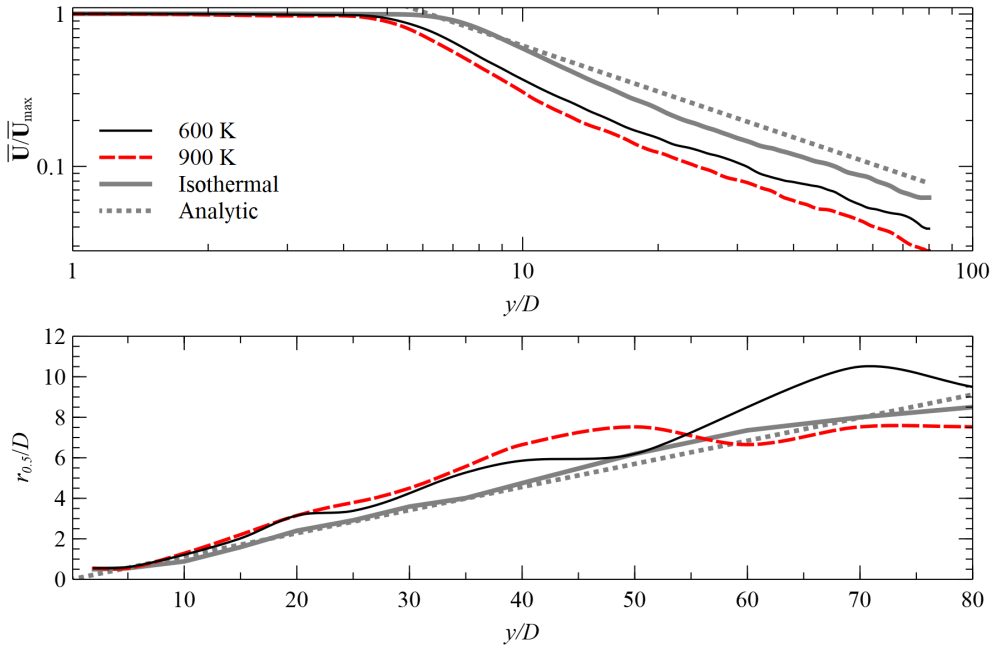

FIGURE B.5: The normalized centerline mean velocity (Top) and its jet width (bottom) profiles of the heated jets, $T = 600$ K (black solid line), $T = 900$ (red dashed line) K, are plotted and compared to isothermal jet (grey solid line) and analytical solutions (grey dotted line)

Both heated $T = 600$ K and 900 K cases were simulated at time step of $\Delta t = 7 \times 10^{-7}$ s and 5×10^{-7} s, respectively, so as to maintain the CFL at 0.15. Upon 20 flow through time (FTT) of the transient phase, the statistical mean states of both heated jets were collected for another 40 FTT. The normalized mean velocity and temperature of heated jets are then analyzed and compared in Figure B.5 and Figure B.6, respectively, in terms of velocity/temperature decaying profile and spreading width. According to the top graph in Figure B.5, the normalized velocity of heated jets showed deviation from the analytical solution. Shorter potential core for heated jets was observed as well when comparing to isothermal jet. The jet spreading width (bottom graph in Figure B.5) plot, however, shows both heated jets' half width profiles are agree well with both the isothermal case and analytical solution especially the near field region ($y/D < 15$). Recalculation of the statistical mean of the flows for more FTT will help to reduce the discrepancies in the far fields. Using finer grid resolution will improve the results as well. For current work, it is enough since the main acoustic sources is from the potential core of the jet

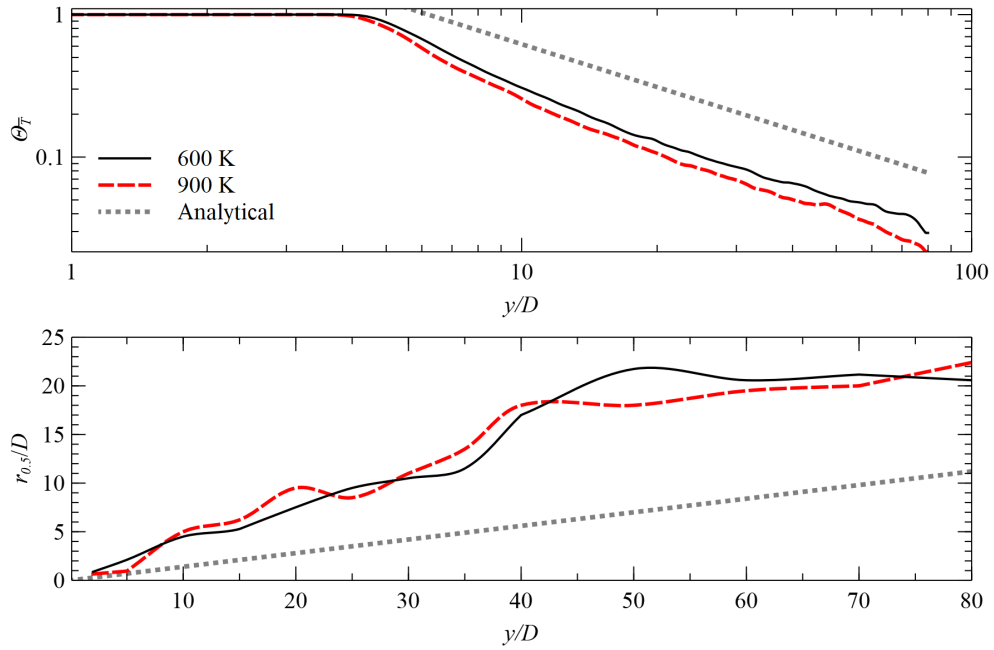

FIGURE B.6: The normalized centerline mean temperature (Top) and its jet width (bottom) profiles of the heated jets, $T = 600$ K (black solid line), $T = 900$ (red dashed line) K, are plotted and compared to analytical solutions (grey dotted line).

which is considered as near field region. The normalized temperature is defined as,

$$\Theta_{\overline{T}} = \frac{\overline{T} - \overline{T}_{\infty}}{\overline{T}_{\text{in}} - \overline{T}_{\infty}}. \tag{B.5}$$

where $\overline{T}_{\infty} = 300$ K is the ambient temperature and $\overline{T}_{\text{in}}$ is the inlet heated flow temperature. Figure B.6 top graph showed similar centerline mean temperature decaying profiles as compared to velocity counterpart as shown earlier, deviated from analytical solution. The half width of mean temperature graph, as shown in bottom graph of Figure B.6, indicates the stronger thermal diffusion than the molecular diffusion if compared to their corresponding mean velocity half-value width. Moreover, it shows large deviation from the analytical solution [96].

To further justify, the similarity plots of the normalized mean velocity, $\overline{\mathbf{U}}/\overline{\mathbf{U}}_{\text{max}}$, and mean temperature, $\Theta_{\overline{T}}$ are plotted in Figure B.7 at various axial locations from near- to far-fields. The graph (a) in Figure B.7 indicates the length of the velocity potential core is longer than the temperature potential core, whereas heated jet with higher temperature has longer temperature potential core length provided same *Re*. In terms of the normalized mean velocity (solid line), both heated cases

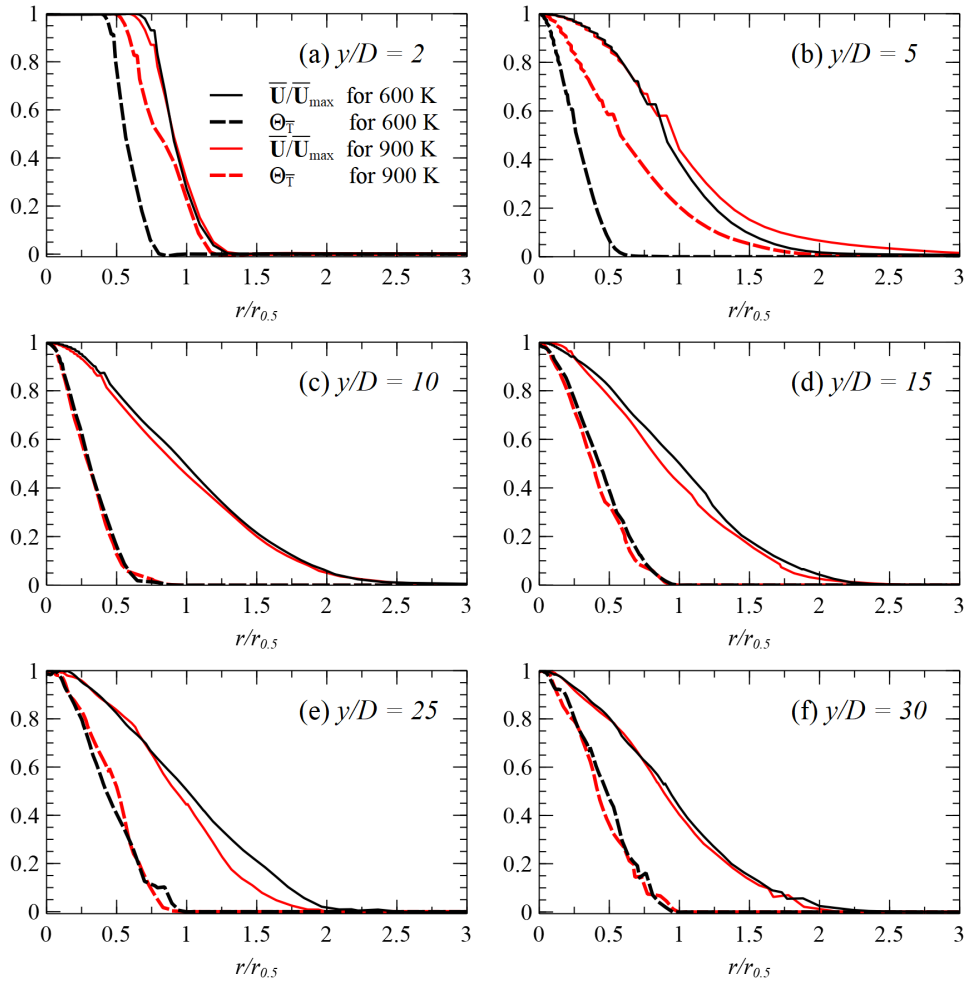

FIGURE B.7: The similarity plots of normalized mean velocity, $\overline{\mathbf{U}}/\overline{\mathbf{U}}_{\max}$ (solid line) and mean temperature, $\Theta_{\overline{T}}$ (dashed line) at different axial locations for both 600 K (black) and 900 K (red) heated jet simulations.

are comparable and achieve self-similarity for $y/D > 15$ since both have same Re. The similarity plots of $\Theta_{\overline{T}}$, however, show discrepancy between two heated jet simulations in near-field, where $y/D \leqslant 5$. The discrepancy in the near field can be attributed to the high amplitude of pressure and density perturbations induced by high speed flow and temperature difference as shown in Figure B.8 and Figure B.9. In the far-field, where the jets are fully developed, both heated jets achieve self-similarity since the thermal diffusion in radial and axial directions are not kin to maximum temperature and Re [97].

Figure B.8 compared the pressure perturbation, p' contours in same scale at 1×10^5 time steps among three different T_{in}. The strength of p' was observed to associate with the jet velocity. Based on Figure B.8, both the isothermal ($T_{in} = 300$ K) and $T_{in} = 600$ K heated jet cases show they shared similar p' contours despite higher

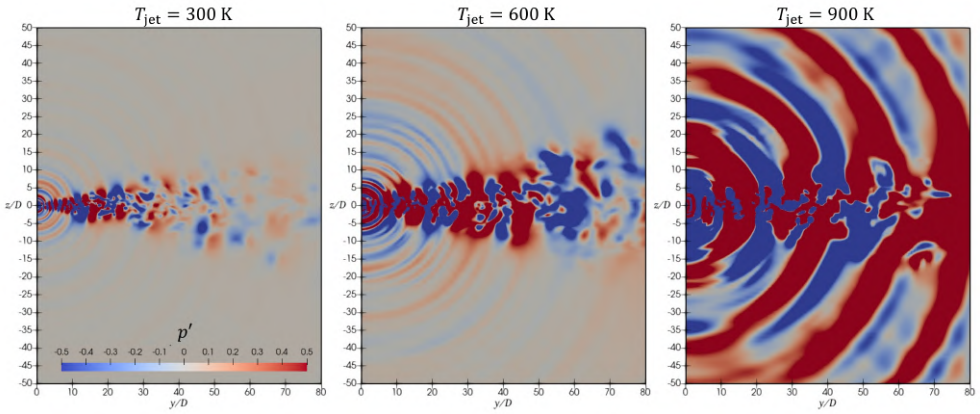

FIGURE B.8: Comparison of the pressure perturbation contour at same time steps of 1×10^5 for isothermal (left), 600 K (middle), and 900 K (right) heated jets simulations. The contour color ranges between ±0.5 Pa.

p' strength was observed for $T_{in} = 600$ K heated case due to higher inlet velocity. Further increment of the inlet velocity and temperature has changed the p' contour entirely. Much higher perturbation strength and distinct waves and wavelength are observed as illustrated in Figure B.8 for $T_{in} = 900$ K heated jet simulation.

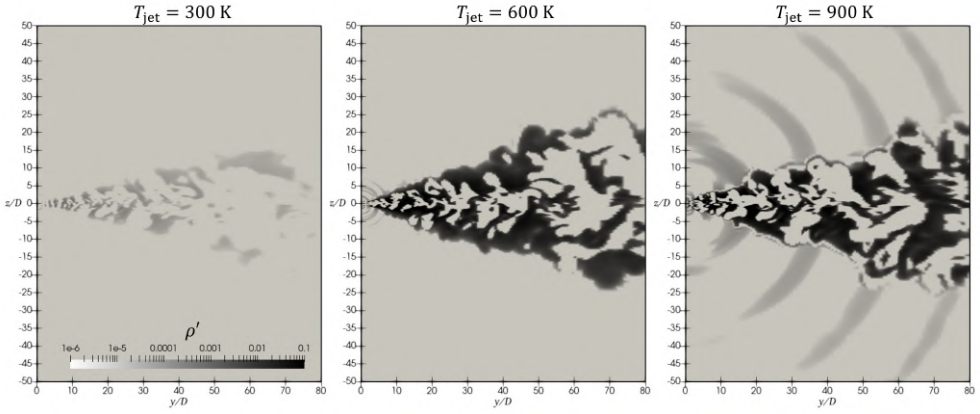

FIGURE B.9: Comparison of the pressure perturbation contour at same time steps of 1×10^5 for isothermal (left), 600 K (middle), and 900 K (right) heated jets simulations. The contour color is in log scale from 1×10^{-7}kg/m^3 to 0.1kg/m^3.

The density perturbation, ρ' contours (in log scale) were presented in Figure B.9 to study the thermal effect toward the acoustic wave. The results have showed the ρ' is negligible in relative low velocity jets, for instance, the isothermal and 600 K heated jet simulations. With the same Re, 900 K heated jet will has higher velocity which induces strong shearing layer and eventually generate intense jet noise. The pressure perturbation p' has also affected the density fluctuation, ρ' significantly as compared to other cases. The most noticeable difference is the

wavefront of ρ' which traveling outside the jet wake and propagating downstream of the jet. Likewise for the p' contour plot of $T_{in} = 900$ K heated jet case, the longer wavelength of acoustic wave can be observed and it associates with certain frequencies.

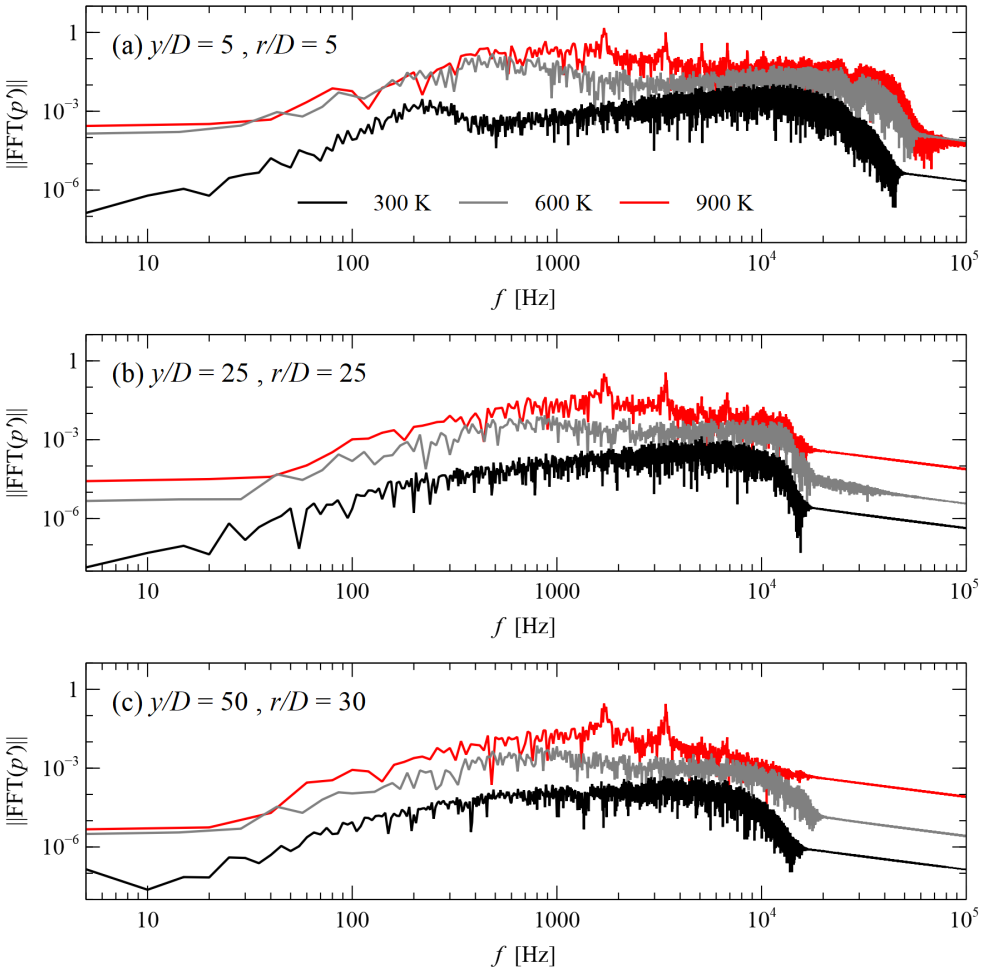

FIGURE B.10: p' FFT spectra of isothermal(black) , 600 K (grey), and 900 K (red) heated jets simulations at different locations are plotted and compared. Two high frequencies were observed for 900 K heated jet simulations.

With FFT of pressure perturbations, the frequency spectra of p' at selected locations outside of the jet are plotted for all three jet simulations as presented in Figure B.10. Generally, the near field region ($y/D = 5$) contains wider range of broadband noise as compared to far fields regions ($y/D = 25, 50$). Jets with higher temperature and velocity show larger FFT amplitude in several orders, consistent to p' contours shown in Figure B.8. Besides, two distinct frequencies are detected, 1700 and 3400 Hz, for $T_{in} = 900$ K heated jet simulation (red line) with at least one order higher of amplitudes. This explains the observations in both Figure B.8

and Figure B.9. To this end, the jet temperature shows its significant influence toward the jet noise in terms of noise amplitude provided same Reynolds number.

B.3 Combustion Models In OpenFOAM

B.3.1 Implementation of Combustion Models

For works involving reacting flow, chemistry closure model is required to properly represent the flow behavior. Two strategies are available for different types of flame regimes which are the diffusion and premixed flames. The diffusion flame can be modeled by incorporating the flamelet/progress-variable (FPV) model [81, 82], whereas the flame prolongation of intrinsic low-dimensional manifolds (FPI) model [83, 84] can be used to simulate the premixed flames. Despite being representative of the different flame regimes, both models share similarities in terms of the chemical tabulation method and the governing equations. In essence, both models assume that the multi-dimensional flame structure is the ensemble of one-dimensional laminar flames. The main advantage of having tabulated-chemistry combustion models is to reduce the total computational costs by solving the chemical reaction equations prior to the flow simulation and parameterizing the reactions by a few scalar variables. Coupling to the flow is achieved by transporting those scalars along with the flow variables. In general, both models are split into two stages: the pre-processing and the flow solving stages as depicted in Figure B.11.

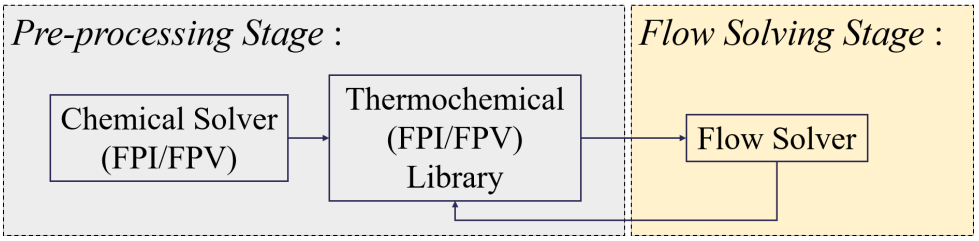

FIGURE B.11: The block diagram of two stages describes the feedback between the thermochemical libraries and flow solver.

B.3.1.1 Pre-processing stage

Figure B.12 illustrates two types of configurations in generating diffusion and premixed flamelets during the pre-processing stage. The mixture fraction, Z is commonly used in diffusion flame, due to the ease of describing the composition of the mixture. The mixture fraction is defined as the mass fraction of the fuel stream in mixture as indicated in (B.6).

$$Z = \frac{m_1}{m_1 + m_2} , \tag{B.6}$$

where m_1 and m_2 are mass flux from the fuel and oxidizer streams respectively. Thus, Z of the fuel stream will always be 1 whereas Z of the oxidizer stream will be 0. A counterflow diffusion flame configuration (Figure B.12 (a)) is used to generate the diffusion flamelets. The pure fuel and oxidizer streams are injected from opposed nozzles and form a diffusion flame sheet sitting in between the two nozzles. The distribution of thermodynamic properties and species mass fractions along the centerline are then tabulated into FPV flamelets library. These flame properties are depend on the boundary conditions of the configuration such as the injection velocity and ambient pressure. In other words, multiple flamelets can be obtained by changing the flow velocity, which directly changes the scalar dissipation rate, χ. Note that two-point continuation technique [98] has been adopted to ensure the continuity of the S-curve.

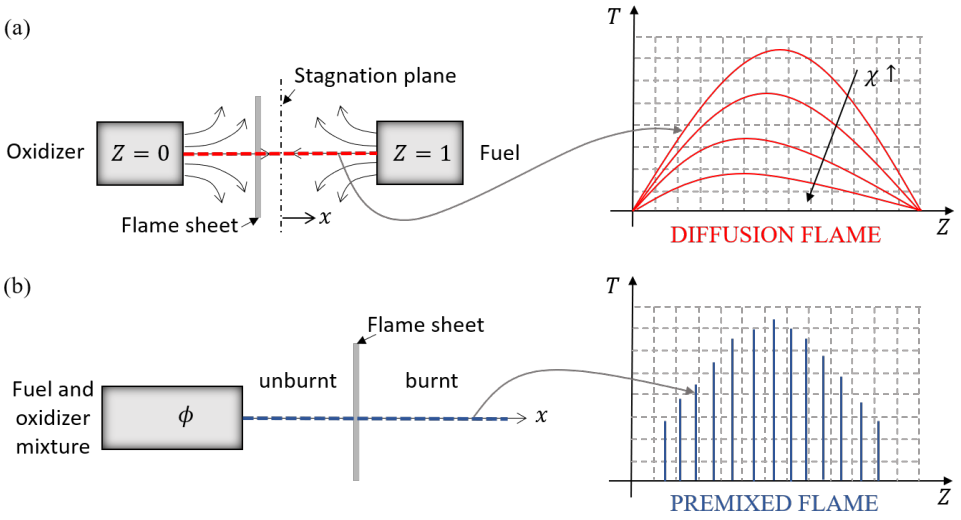

FIGURE B.12: The schematic diagrams of the pre-processing stage in constructing thermo-chemical libraries for both (a) diffusion flame and (b) premixed flame.

Figure B.12 (b) shows a free propagating laminar flame configuration by injecting a homogeneous mixture of fuel and oxidizer stream through a single nozzle and forming flame sheet along the flow path. Similar to the diffusion flame, the thermodynamic properties and species mass fractions along the stream are tabulated into FPI flamelets library. In premixed flame regime, the equivalence ratio, ϕ, is commonly used, which defines the ratio of the actual fuel/oxidizer ratio to the stoichiometric fuel/oxidizer ratio. A stoichiometric mixture occurs when $\phi = 1$, if $\phi > 1$, the mixture is rich with excess fuel. Otherwise the mixture is lean with excess oxidizer. By changing the equivalence ratio of the mixture injected through the nozzle, different premixed flames can be obtained, making up the lines shown at the bottom right graph of Figure B.12. Due to the lean and rich flammability limits of premixed flame, the FPI flamelets library is tabulated within a specific range of equivalence ratio in contrast to the FPV library. For convenience in use of the diffusion flame, one may express the equivalence ratio, ϕ in term of mixture fraction, Z, as described in (B.7).

$$Z(\phi) = \frac{\phi(1 - Y_{N_2,2})}{s + (1 - Y_{N_2,2})} \ , \tag{B.7}$$

where s is the air/fuel stoichiometric mass ratio and $Y_{N_2,2}$ is the nitrogen mass fraction in oxidizer. For both models, since the mixture fraction does not contain any intrinsic information about the chemical reactions, at least one additional scalar variable is required. Therefore, a reaction progress variable, C, is introduced to act as an additional reactive scalar in order to be independent from the mixture fraction [81]. When the progress variable is zero, it indicates the flame has extinguished and zero combustion efficiency, whereas its maximum value indicates chemical equilibrium [98]. Typically, the mass fractions of the hydrocarbon combustion products are linearly combined to give a progress variable that varies monotonically with the reaction progress [99] as in (B.8).

$$C = \sum_{n=1}^{N_{Spec}} w_n Y_n \ , \tag{B.8}$$

where N_{Spec} is defined as the total number of the selected species, and the w_n and the Y_n represent the weightage and the mass fraction of the corresponding n species, respectively. For FPI library, each solution lines is parameterized by merely C and Z due to its bijective relation with the equivalence ratio, ϕ. The progress variable,

C, in the FPV library, however, cannot be used directly as it is no bijective relation with strain rate, ϑ. Instead, a flamelet parameter, Λ is used which is defined as the stoichiometric value of the progress variable of each flamelet solutions [82] as stated in (B.9). In fact, there is no a fixed rule to define the flamelet parameter as long as it is able to differentiate between each flamelet solutions, i.e. it must be bijective function.

$$\Lambda = C|Z_{st} \ . \tag{B.9}$$

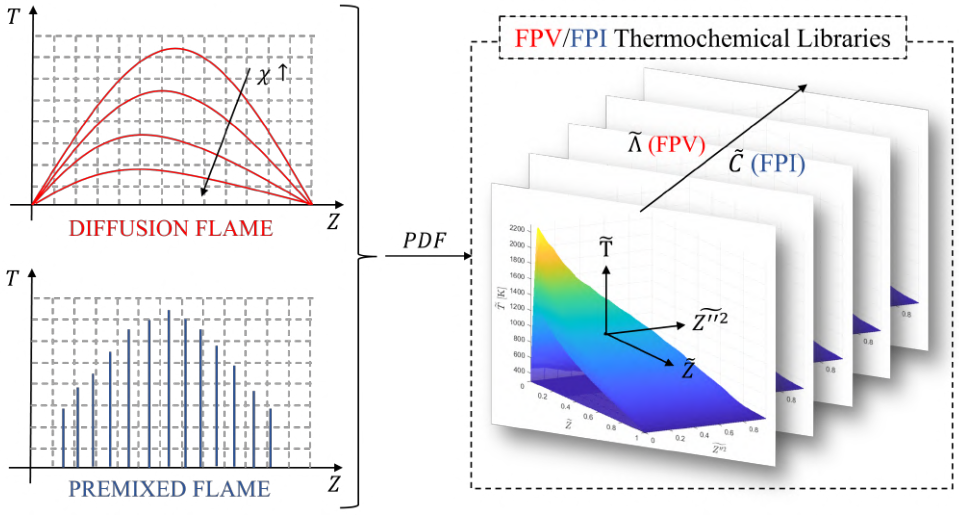

FIGURE B.13: The schematic diagram of filtering process over the flamelet solutions and construction of the thermochemical libraries.

Upon the tabulations of flamelet solutions, the filtered values of the thermochemical data are then integrated by using the Favre presumed probability density function (PDF) methods. By assuming the statistical independence between Z and Λ for FPV model as well as Z and C for FPI model, the joint PDFs of $P(Z,\Lambda)$ and $P(Z,C)$ can be calculated as the multiplication of PDF of Z and PDF of $\Lambda|Z$ or PDF of $C|Z$. A simple Dirac function is used to evaluate the $\widetilde{P}(\Lambda|Z)$ for FPV or $\widetilde{P}(C|Z)$ for FPI model, whereas, a presumed β-PDF is implemented to approximate the PDF of Z, $P(Z)$ with the mean mixture fraction, $\widetilde{Z}$ and its variance, $\widetilde{Z''^2}$. After the PDF integration, all the mean thermochemical data are tabulated as function of $\widetilde{Z}$, $\widetilde{Z''^2}$ and $\widetilde{\Lambda}$ for FPV model or $\widetilde{C}$ for FPI model as indicated in Figure B.13.

$$\widetilde{h_s} = \int_0^\infty \int_0^1 h_s(Z,\Lambda/C)\widetilde{P}(Z,\Lambda/C)dZd\Lambda/C \ , \tag{B.10}$$

$$\widetilde{Y_n} = \int_0^\infty \int_0^1 Y_n(Z,\Lambda/C)\widetilde{P}(Z,\Lambda/C)dZd\Lambda/C \ , \tag{B.11}$$

$$\widetilde{\dot{\omega}_n} = \int_0^\infty \int_0^1 \dot{\omega}_n(Z, \Lambda/C)\widetilde{P}(Z, \Lambda/C)dZd\Lambda/C \,, \tag{B.12}$$

$$\widetilde{\dot{\omega}_C} = \sum_{n=1}^{N_{Spec}} \widetilde{\dot{\omega}_n} \,, \tag{B.13}$$

$$\widetilde{C} = \sum_{n=1}^{N_{Spec}} w_n \widetilde{Y_n} \,. \tag{B.14}$$

After convolution with PDF, these two-dimensional flamelet tables are extended to three-dimensional flamelet libraries in order to account for the turbulent flow during the flow solving stage.

B.3.1.2 Flow solving stage

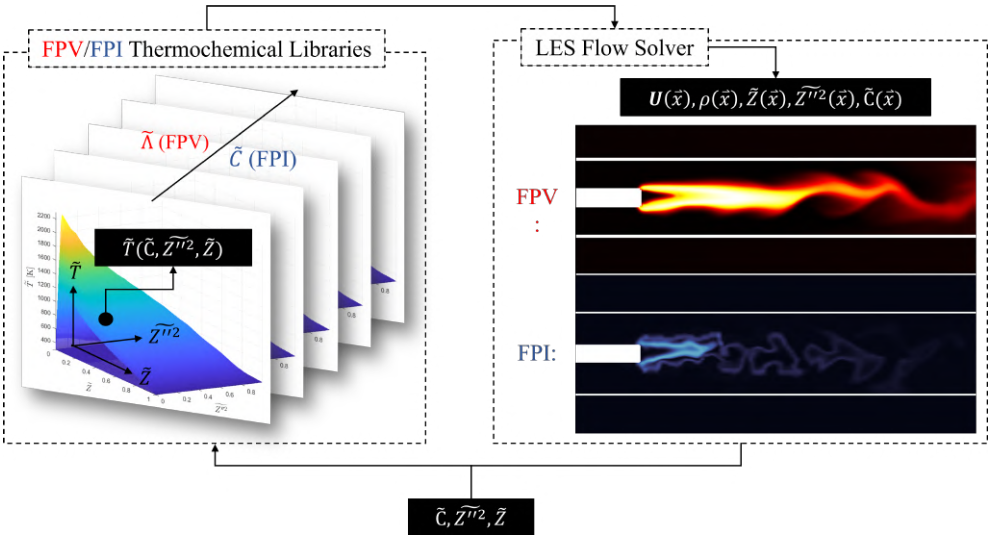

FIGURE B.14: The coupling of pre-processing and flow solving stages.

Figure B.14 illustrates the established thermochemical libraries are coupled to the LES flow solver to solve the three additional scalar transport equations as well as the NS equations. The three additional scalar transport equations are the filtered mixture fraction, $\widetilde{Z}$, its variance, $\widetilde{Z''^2}$, and the filtered progress variable, $\widetilde{C}$, as shown in (B.15) to (B.17).

$$\partial_t(\rho\widetilde{Z}) + \nabla \cdot (\rho \mathbf{U}\widetilde{Z}) = \nabla \cdot \left[\left(\frac{\mu}{Sc} + D_t \right) \nabla \widetilde{Z} \right] \,, \tag{B.15}$$

$$\partial_t\left(\rho\widetilde{Z''^2}\right) + \nabla\cdot\left(\rho\mathbf{U}\widetilde{Z''^2}\right) = \nabla\cdot\left[\left(\frac{\mu}{Sc} + D_t\right)\nabla\widetilde{Z''^2}\right] - \rho\widetilde{\chi} + 2D_t\left(\nabla\widetilde{Z}\right)^2 , \quad \text{(B.16)}$$

$$\partial_t\left(\rho\widetilde{C}\right) + \nabla\cdot\left(\rho\mathbf{U}\widetilde{C}\right) = \nabla\cdot\left[\left(\frac{\mu}{Sc} + D_t\right)\nabla\widetilde{C}\right] + \rho\widetilde{\dot{\omega}} . \quad \text{(B.17)}$$

In the context of LES, the eddy viscosity, D_t, in the diffusion terms and the scalar dissipation rate, $\rho\widetilde{\chi}$, in the destruction term of (B.16) have to be modeled to ensure the closure of the equations [81, 82].

$$D_t = \frac{\mu_t}{Sc_t} , \quad \text{(B.18)}$$

$$\rho\widetilde{\chi} = 2.0D_t\frac{\widetilde{Z''^2}}{\Delta^2} . \quad \text{(B.19)}$$

where the Schmidt number, Sc, is set to be unity whereas the turbulent Schmidt number, Sc_t, can be set within the range of 0.9 to 1.0 [92, 98, 100]. In the framework of *flameletFoam* [92], which used scalar dissipation as one of the parameters and the pressure-based flow solver,*rhoReactingFoam*, two new modified solvers are constructed in this work to account for buoyancy effect. These two solvers are *FPVBuoyantFoam* (diffusion flame) and *FPIBuoyantFoam* (premixed flame).

B.3.2 Validation of Combustion Model

The flamelet/progress-variable (FPV) combustion model was first implemented into OpenFOAM framework, and thereafter carrying out a few test cases to validate the model. For example, a free jet flow was simulated under two conditions: turbulent non-reacting and reacting flows. The non-reacting free jet flow simulation showed good agreement with the analytical solutions in terms of the decaying of jet axial velocity and jet spreading, as depicted in Figure B.15.

In reacting flow simulation, the results were then compared to the experimental works by Sandia National Laboratory [101]. The simulation results are hardly validated with existing experimental measurements as the so-so agreement above. Figure B.16 describes the temperature contours of a reacting jet flow and Figure B.17 compares temperature distribution qualitatively with experimental measurements. The discrepancies can be attributed to the lack of information about the nozzle

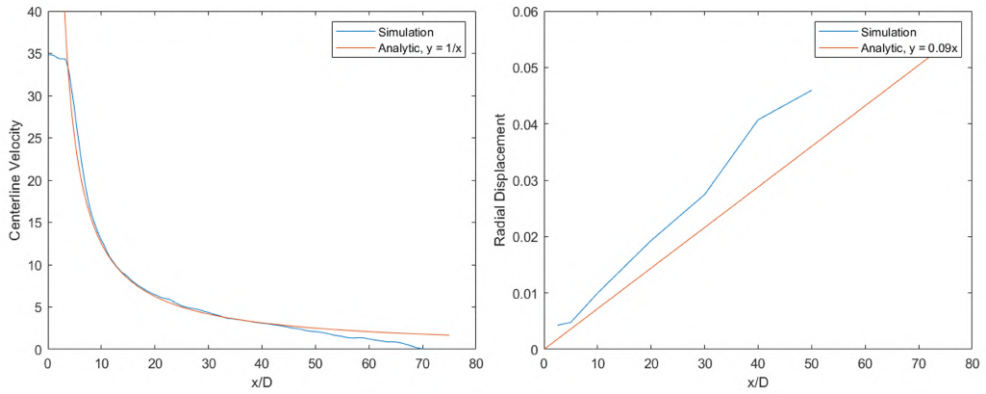

FIGURE B.15: (left) Axial velocity of free jet flow. (right) Free jet flow width.

exit velocity and mass flow rate of the experiment. However, the coupling between the chemical library and flow solver is successfully incorporated, therefor there is no need to further debugging. Next, few thermoacoustic related topics have been explored, they are generally divided into supersonic and subsonic fields. For the supersonic topic, a reacting supersonic jet-in-crossflow (SJICF) had been investigated to evaluate any combustion noise. After that, the subsonic topic is studied with Rijke tube configuration in order to evaluate the combustion instabilities which made up the second year of works.

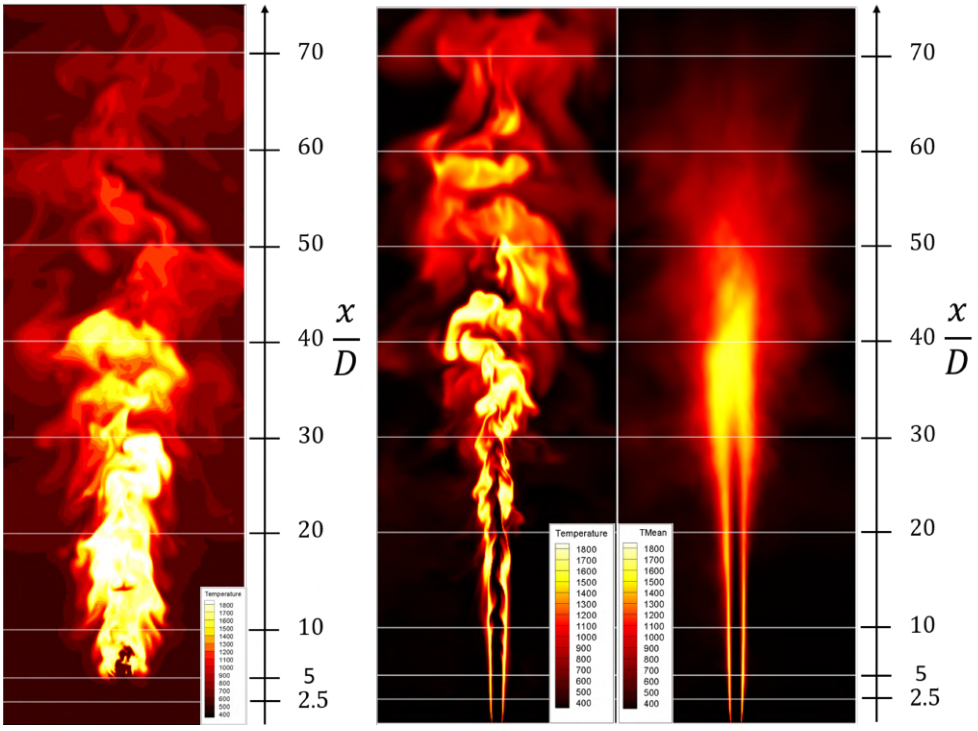

FIGURE B.16: The temperature profile at middle plane with (a) full and (b) upper branch of flamelet library.

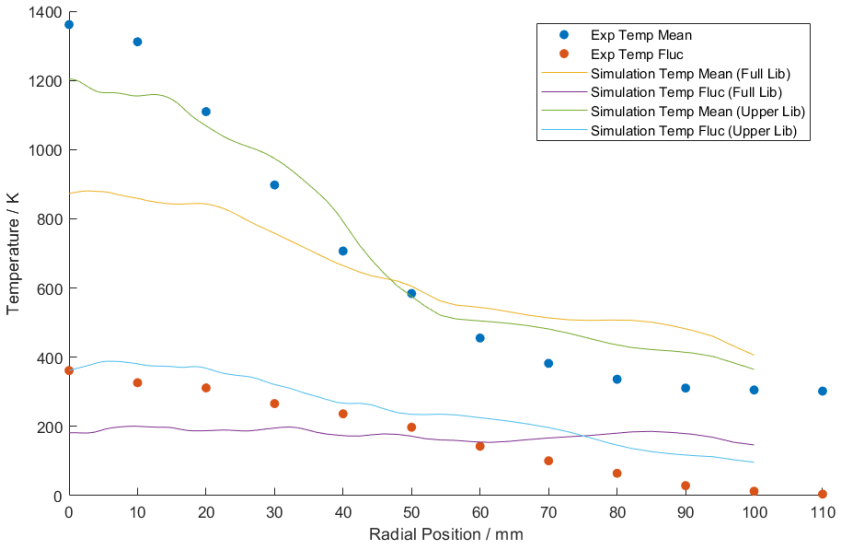

FIGURE B.17: Temperature comparison at $\frac{x}{D} = 50$.

B.4 Combustion Chamber Application

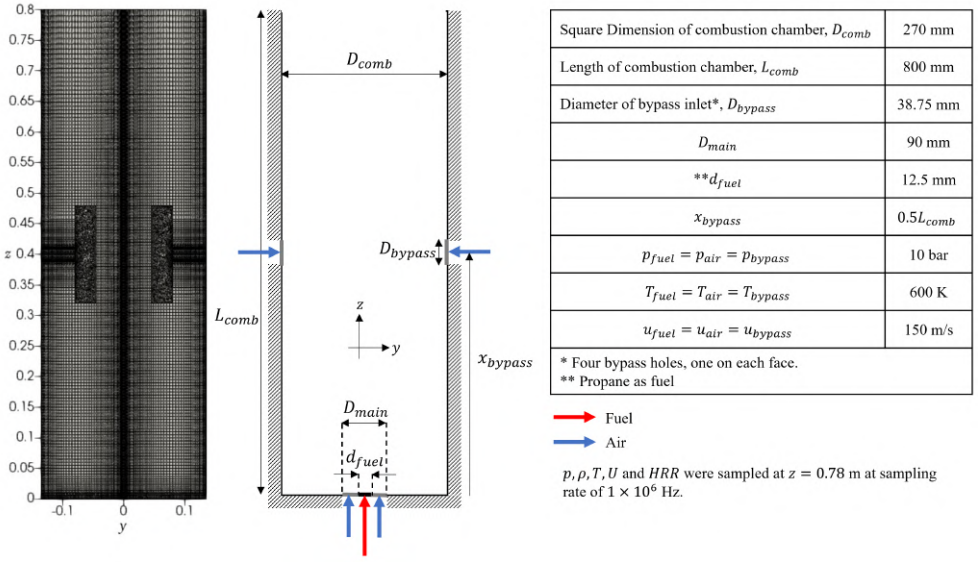

Square Dimension of combustion chamber, D_{comb}	270 mm
Length of combustion chamber, L_{comb}	800 mm
Diameter of bypass inlet*, D_{bypass}	38.75 mm
D_{main}	90 mm
$^{**}d_{fuel}$	12.5 mm
x_{bypass}	$0.5L_{comb}$
$p_{fuel} = p_{air} = p_{bypass}$	10 bar
$T_{fuel} = T_{air} = T_{bypass}$	600 K
$u_{fuel} = u_{air} = u_{bypass}$	150 m/s
* Four bypass holes, one on each face. ** Propane as fuel	

FIGURE B.18: A schematic drawing of the combustion chamber computational domain. Table explains the symbols used in the drawing together with both ambient and boundary conditions.

An engineering application study case was conducted using FPV combustion model (*FPVBuoyantFoam*) under a Seed project, 'Measuring and Simulating the Combustion Noise Generation and Transport in Simplified Turbojet Combustor Models' by TL@NUS. A 3D rectangular combustion chamber was constructed as depicted

in Figure B.18, which shows the dimensions of the computational domain and simulation settings. There are a total of 2.6M cells consisted of structured and unstructured grids. Propane, C_3H_8, was considered to build the thermochemical library, based on boundary conditions of $p_\infty = 10$ bar and $T_\infty = 600$ K.

A piloted diffusion flame was introduced by considering fuel and pure air coflow inlets. Top-hat velocity profile was used for by-pass and fuel inlet, whereas the swirling flow was used for coflow condition to stabilize the flames. For swirling flow setting, the axial, radial and tangential velocities were 110 m/s, 10 m/s and 100 m/s, respectively. No-slip and adiabatic conditions were applied to the chamber wall. The thermodynamic properties were interpolated from the library based on the transported scalars, Z, Z''^2, and C.

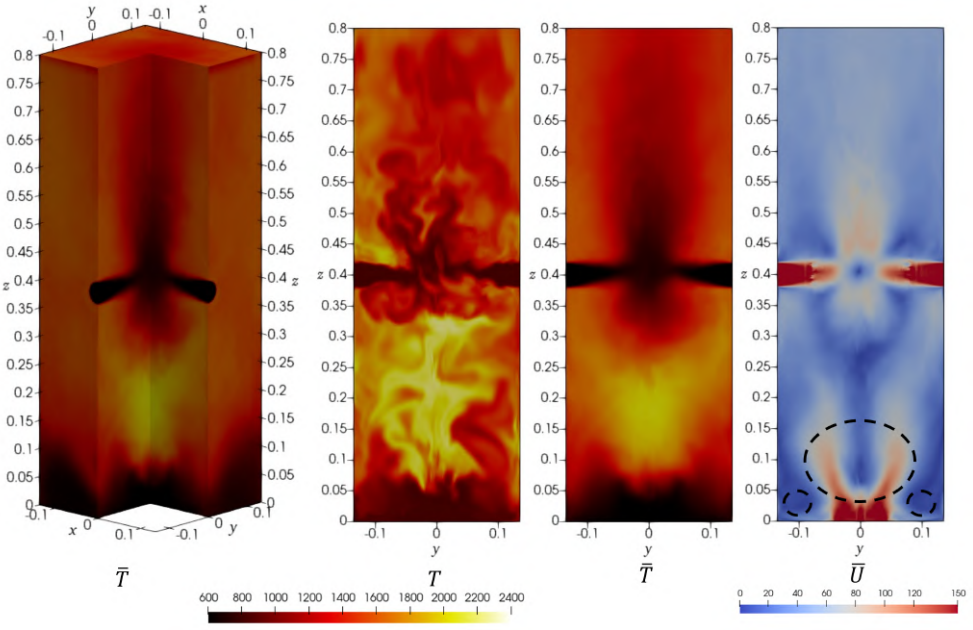

FIGURE B.19: Instantaneous and mean temperature contours for isometric view (left) and $x = 0$ plane. (Most right) The mean velocity contour shows recirculation zones (circled) not only at the corners but also the inner region of the swirling coflow.

Figure B.19 illustrates the isometric view of the mean temperature, $\overline{T}$, and the $x-$planar view of instantaneous T, statistical mean states of temperature, $\overline{T}$ and velocity, $\overline{\mathbf{U}}$. From the $\overline{T}$ contours, the flames are generated and stabilized at $z = 0.05$ m while the flame average temperature can reaches up to 2200 K. The swirling coflow has stabilized the flame by creating a flow recirculation zone which enhances the mixing between fuel and air. This explains the correlation between the flows having high temperature and low velocity, especially in the flame stabilizing

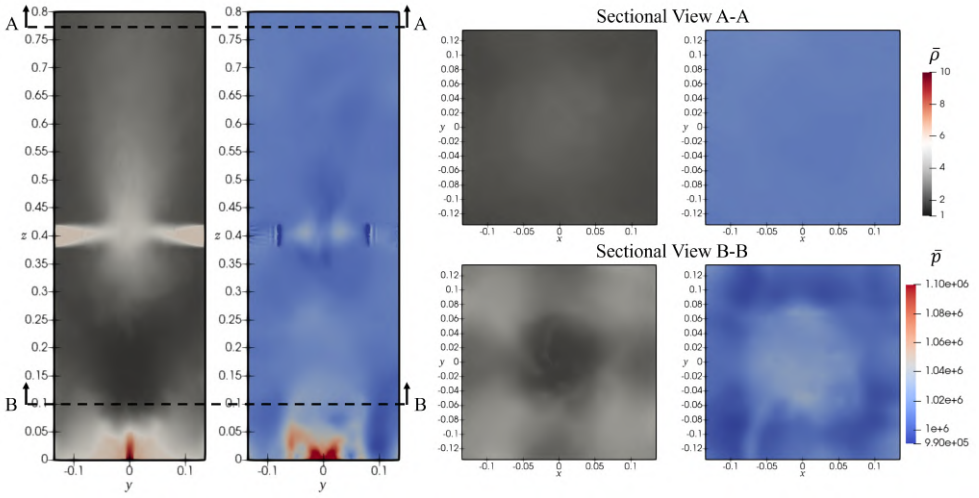

FIGURE B.20: The mean density, $\bar{\rho}$, and pressure, $\bar{p}$, contours at (left) $x = 0$ plane and (right) selected cross-sectional views.

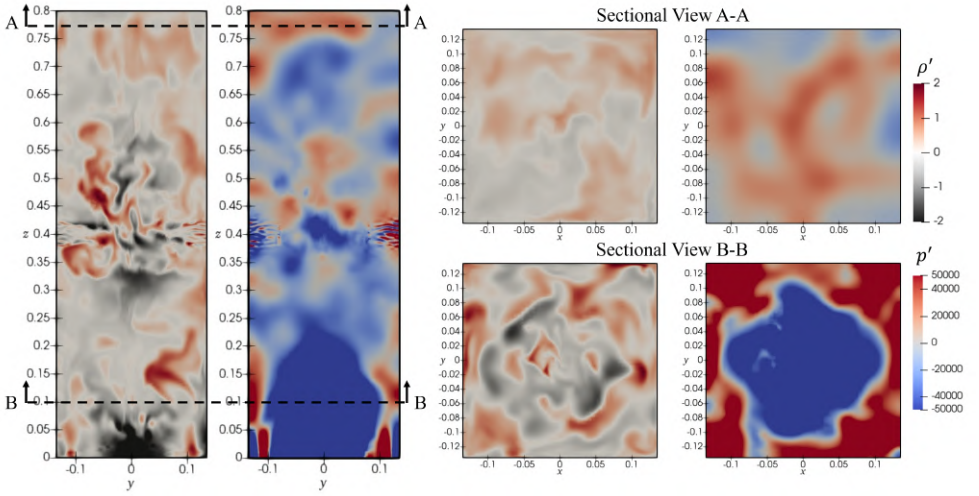

FIGURE B.21: The density, ρ', and pressure, p', perturbation contours at timestamp of 3.75×10^5.

region. At the downstream with the bypass flows, the mean temperature air near the outlet of the combustion chamber has cooled down to about 1500 K, typical air temperature before entering turbine section. Statistical mean states of density, $\bar{\rho}$ and pressure, $\bar{p}$ contours are presented in Figure B.20 at $x = 0$ plane and cross-sectional views of up- (B-B) and downstream (A-A) of the flames. At upstream of the flame (B-B), the $\bar{\rho}$ and $\bar{p}$ clearly show the distinct zones of low/high values. This is because the effective mixing and burning zone happened at around $z = 0.05$ m, where the density value changes abruptly, meanwhile the pressure also reduces. In sectional view A-A, the $\bar{\rho}$ and $\bar{p}$ values are more evenly distributed and diluted

with bypass flows. This is expected since it is away from the combustion active area.

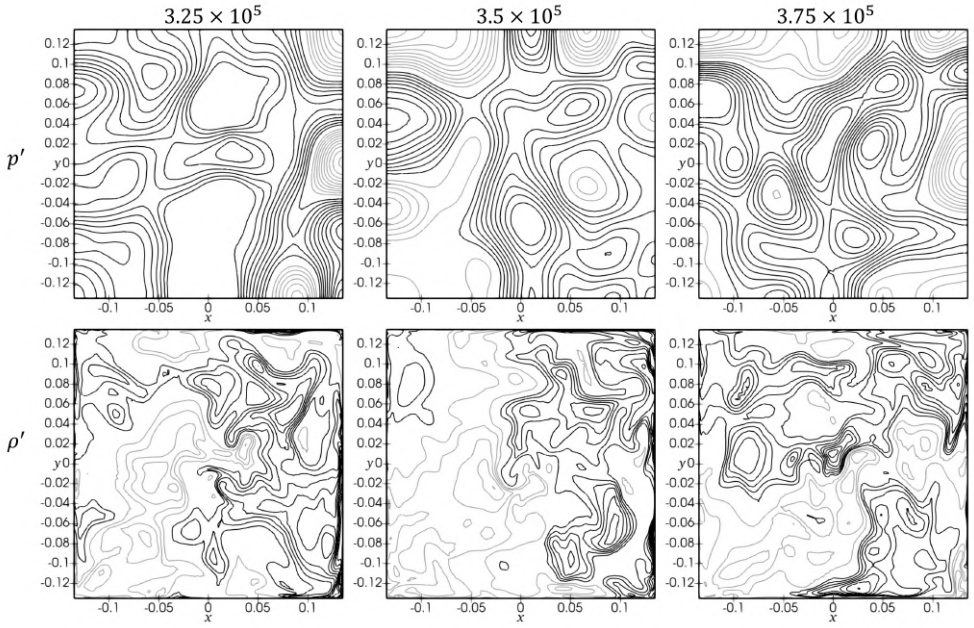

FIGURE B.22: (top row) p' and (bottom row) ρ' contour lines are shown in three timestamps. The p' contour lines range between $\pm(3 \sim 30)$ kPa linearly, whereas ρ' contour lines range between $\pm(0.1 \sim 1)$ kg/m^3. Note that, black and grey colors each represent the positive and negative perturbations, respectively.

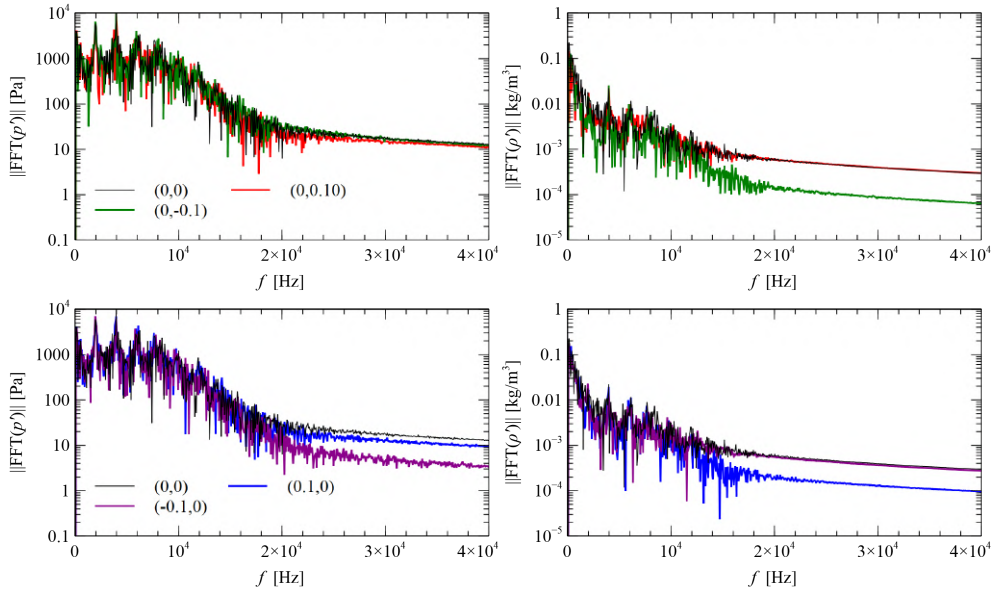

FIGURE B.23: The FFT spectra of (left) p' and (right) ρ' along (top row) $x-$ and (bottom row) $y-$axes at $z = 0.78$ m plane. Note that, the y-axis is in log-scale.

Upon the collection of statistical mean states, the combustion noise and acoustic studies were carried out. The selected primitive fields' pertubations, ρ' and p' contours are presented in Figure B.21 at iteration of 3.75×10^5. Form the B-B cross-sectional view in Figure B.21, the strong perturbations happen at around the mixing and burning areas, but mild fluctuations near to the outlet. Thereafter, three instants of p' and ρ' contour line plots near to the outlet at $z = 0.78$ m plane are shown in Figure B.22. Multiple acoustic pockets were observed but no trend can be detected, likewise for the density perturbation.

Since limited information can be obtained from contour line plots, the FFT of p' and ρ' are performed at locations along $x-$ and $y-$axes as shown in Figure B.23 to extract the thermoacoustic information. The sampling rate was at 1×10^6 Hz for both FFT of p' and ρ'. The FFT of p' (left column) at all selected locations unveil the fundamental frequency of 1951 Hz, together with multiple harmonic tones. The first harmonic frequency, 3967 Hz has highest amplitude. Broadband combustion noise is observed in much higher frequency range ($f > 1.5 \times 10^4$ Hz). Similar resonance frequencies are reported in ρ' FFT spectra (right column). Compared at different locations, all the FFT results share similar spectra despite the difference of amplitude in higher frequency range. In short, the combustion noise and resonance are successfully generated and identified with FPV combustion model.

B.5 Supersonic Jet in Crossflow

Efficient mixing process not only can be achieved in flows but also the supersonic flows with appropriate configurations. One of the evidences is the successfully launched scramjet-engine-powered aircraft in 2004 [102]. The aircraft has flight Mach number not more than 15, and its inlet flow inside the scramjet engine inlet to the combustor is normally one-third of the flight Mach number, the flow inside the combustion chamber is then supersonic [102]. Past work done on the jet in crossflow are summarised in the review paper by Mahesh [103].

The actual flow features of this transverse jet in supersonic crossflow have been examined by both experimentally [104, 105] and numerically [106, 107]. In experimental studies, the detail flow measurements are a big challenge back then, however, a few techniques are still capable to visualise the flow such as the Schlieron

photography [104]. When considering reacting transverse jet in supersonic crossflow, likes the flows inside the scramjet combustor, short flow residence time, rapid mixing and flame stability has imposed difficulty to researchers. Nonetheless, different imaging techniques could be used to investigate the system according to the types of flow visualisations [108]. For instances, Schlieren imaging is used to visualise the flow and shock structure, OH^* chemiluminescence imaging is chosen to investigate the overall reacting jet characteristics, whereas the instantaneous reaction zone is examined by OH planar laser-induced fluorescence (PLIF) imaging [108]. Due to the advancement in computational power in past few decades, the experimental results can be successfully reproduced numerically [107] and it helps people to understand the mechanism and physics behind the system.

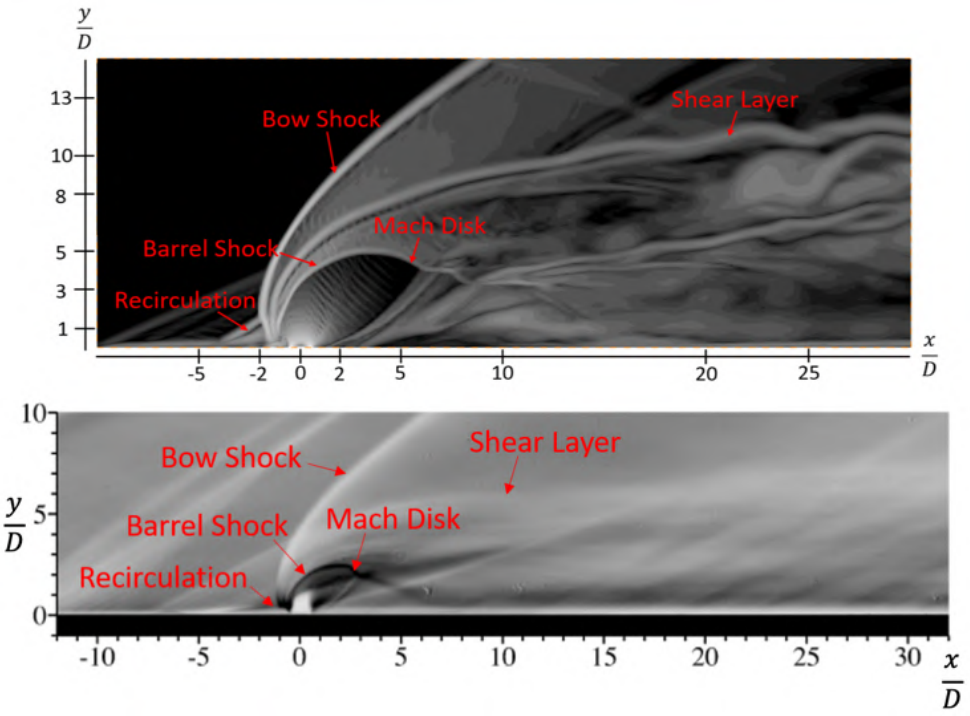

FIGURE B.24: The comparison between (top) density gradient distribution of the reacting SJICF simulation result with (bottom) Schlieren image, is used to demonstrate the flow of fluids of varying density, taken from the experiment conducted by Gamba et.al. Both have shared the common flow and shock features as labelled in red.

To fulfill the aim of research project with title 'Development of Predictive Numerical Tools for Acoustic in Compressible Reaching Flows', a reacting supersonic jet-in-crossflow (SJICF) simulation was conducted to analyze the generation of combustion noise. Briefly, the reacting SJICF configuration consists of one supersonic jet penetrating perpendicularly into a supersonic crossflow, resulting a

complex vortical structures [109–111]. The SJICF configuration by Gamba et.al [108, 112] was chosen for fair comparison. The pressure-based FPV combustion model, *FPVBuoyantFoam*, is modified and adapted for supersonic flow regime, which becomes a density-based solver, known as *FPVCentralFoam* in order to take care of the discontinuities of the flows such as the bow shocks.

Validation (illustrated in Figure B.24) of reacting SJICF simulation has been done by comparing its density gradient contour with Schlieren image [108] which often used to describe the change of the flow density virtually in high speed flow experiments. The comparison shows the main flow and shock features presented in experiment were able to be captured in the simulation of reacting SJICF by *FPVCentralFoam*. For example, both have shown the bow shocks curving around the jet due to the compressibility effects of the traverse jet with cross-flow. In addition, the barrel shocks were deformed and terminated in a tilted Mach disk, at the downstream, the shear layers of the jet were clearly be seen in both simulation and experiment results. Hence, the simulation results of the reacting SJICF are said to qualitatively match with the experiment works done by Gamba et. al [108, 112] based on the common flow and shock features.

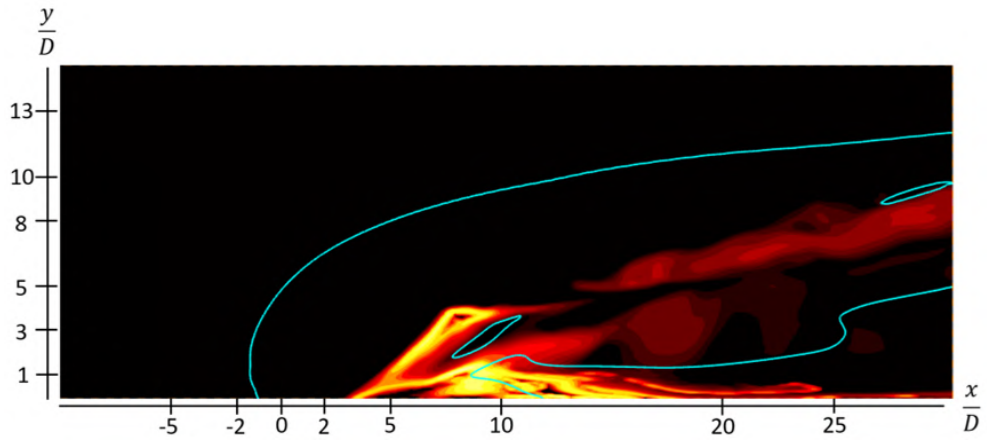

FIGURE B.25: The heat-release rate profile from the reacting SJICF simulations. The stoichiometric mixture fraction is indicated by the solid contour line.

Furthermore, Figure B.25 illustrates the mean heat-release rate profile from a reacting SJICF, clearly marking the flame location and indicating a sustained and stable flame. This relatively stable flame suggests that the SJICF involves only combustion noise, as expected, but not combustion instability, because the flame and acoustic wave has just a one-way coupling.

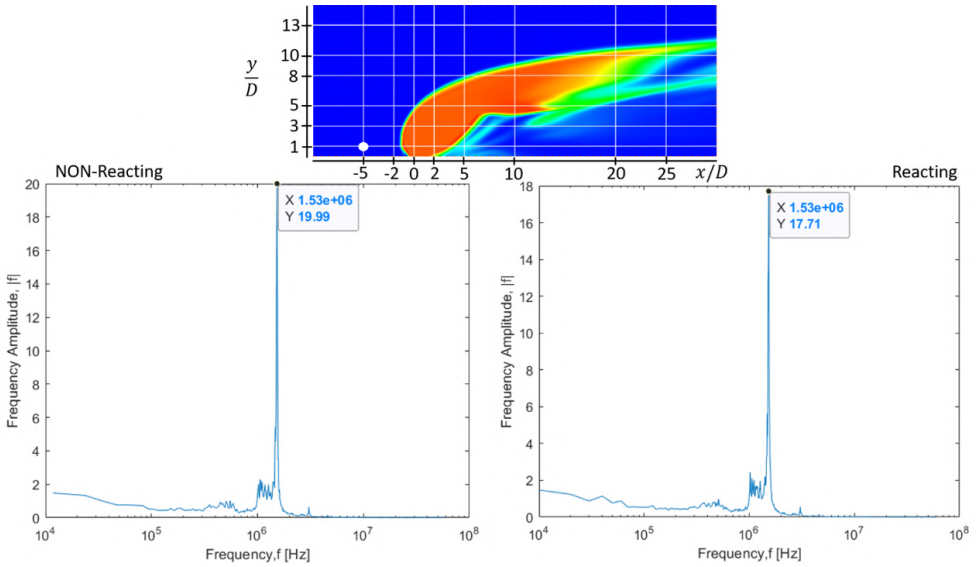

FIGURE B.26: The FFT results of the (left) non-reacting and (right) reacting SJICF configuration at an upstream location of the jet, which is indicated by the white dot in the contour plot. Both cases exhibit similar frequency responses.

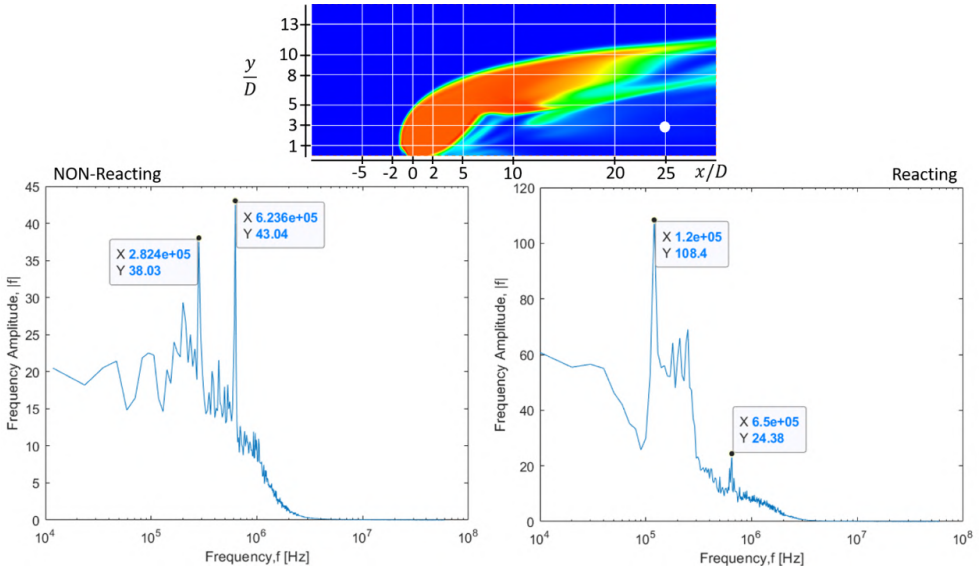

FIGURE B.27: The FFT results of the (left) non-reacting and (right) reacting SJICF configuration at a downstream of the jet, which is indicated by the white dot in the contour plot. The frequency response of the two cases differs, indicating the presence of combustion noise in the reacting SJICF case.

To prove the existence of the combustion noise, the temporal pressure fluctuation profile in both non-reacting and reacting SJICF simulations were collected at two different locations, one upstream and the other downstream of the jet. No combustion at the upstream of the jet, hence, the frequency responses are expected to be the same as shown in Figure B.26. At the downstream of the jet, however, the

reacting SJICF (right plot of Figure B.27) exhibits a totally different frequency response from the non-reacting SJICF (left plot of Figure B.27). This variation in the frequency response is likely attributed to the phenomenon of combustion noise as a result of the existence of flame.

This supersonic topic study had come to end due to more interesting facts on subsonic topic have found. Also, experimental facilities are available and more tractable to run and set up at NTUsg. Therefore, the following research direction will be focusing more on the subsonic thermoacoustic related topic such as the heated and combusting Rijke tube cases. Lastly, it is worth to mention that this work was done in support of our team involvement in a TL@NUS grant, which focuses on developing numerical tools for prediction of combustion instabilities (Rijke tube) and noise (SJICF).

Bibliography

[1] N. Peake and A. B. Parry. Modern challenges facing turbomachinery aeroacoustics. *Annu. Rev. Fluid Mech.*, 44:227–248, 2012.

[2] C. M. Arndt, M. Severin, C. Dem, M. Stöhr, A. M. Steinberg, and W. Meier. Experimental analysis of thermo-acoustic instabilities in a generic gas turbine combustor by phase-correlated piv, chemiluminescence, and laser raman scattering measurements. *Experiments in Fluids*, 56(4):1–23, 2015.

[3] K. R. McManus, T. Poinsot, and S. M. Candel. A review of active control of combustion instabilities. *Prog. Energ. Combust.*, 19:1–29, 1993.

[4] L. S. Kovasznay. Turbulence in supersonic flow. *Journal of the Aeronautical Sciences*, 20(10):657–674, 1953.

[5] A. A. Hemeda and B. Elhadidi. Domain decomposition technique for solution of acoustic wave scattering. *AIAA J.*, 52(2):408–418, 2014.

[6] US Vevek, B. Elhadidi, and W. L. Chan. A domain decomposition technique for small amplitude wave interactions with shock waves. *J. Comp. Phys.*, 437:110326, 2021.

[7] J. W. S. B. Rayleigh. *The theory of sound*, volume 1. Macmillan, 1894.

[8] T. Poinsot and D. Veynante. *Theoretical and numerical combustion*. R. T. Edwards, Inc., 2005.

[9] ESI-OpenCFD. OpenCFD release OpenFOAM®v1912. `https://www.openfoam.com/news/main-news/openfoam-v1912`, Last accessed: Jun 20 2021, 2019.

[10] M. J. Lighthill. On sound generated aerodynamically i. general theory. *Proceedings of the Royal Society of London. Series A. Mathematical and Physical Sciences*, 211(1107):564–587, 1952.

[11] M. J. Lighthill. On sound generated aerodynamically ii. turbulence as a source of sound. *Proceedings of the Royal Society of London. Series A. Mathematical and Physical Sciences*, 222(1148):1–32, 1954.

[12] A. Powell. Theory of vortex sound. *J. Acoust. Soc. Am.*, 36(1):177–195, 1964.

[13] D. Violato, P. Moore, K. Bryon, and F. Scarano. Application of powell's analogy for the prediction of vortex-pairing sound in a low-Mach number jet based on time-resolved planar and tomographic piv. In *16th AIAA/CEAS Aeroacoustics Conference*, page 3959, 2010.

[14] J. F. Williams and D. L. Hawkings. Sound generation by turbulence and surfaces in arbitrary motion. *Philosophical Transactions for the Royal Society of London. Series A, Mathematical and Physical Sciences*, pages 321–342, 1969.

[15] F. Farassat and M. K. Myers. Extension of Kirchhoff's formula to radiation from moving surfaces. *J. Sound Vib.*, 123(3):451–460, 1988.

[16] H. H. Hubbard. Aeroacoustics of flight vehicles: Theory and practice. volume 1. noise sources. Technical report, National Aeronautics and Space Admin Langley Research Center Hampton VA, 1991.

[17] J. Bridges and F. Hussain. Direct evaluation of aeroacoustic theory in a jet. *J. Fluid Mech.*, 240:469–501, 1992.

[18] A. T. Fedorchenko. On some fundamental flaws in present aeroacoustic theory. *J. Sound Vib.*, 232(4):719–782, 2000.

[19] Y. Sathyanarayana and M. L. Munjal. A hybrid approach for aeroacoustic analysis of the engine exhaust system. *Applied Acoustics*, 60(4):425–450, 2000.

[20] M. Bauerheim, M. Cazalens, and T. Poinsot. A theoretical study of mean azimuthal flow and asymmetry effects on thermo-acoustic modes in annular combustors. *Proc. Combust. Inst.*, 35(3):3219–3227, 2015.

[21] P. Jordan and Y. Gervais. Subsonic jet aeroacoustics: associating experiment, modelling and simulation. *Experiments in Fluids*, 44(1):1–21, 2008.

[22] J. Bridges and M. P. Wernet. Measurements of the aeroacoustic sound source in hot jets. aiaa paper 2003-3130. In *9th AIAA/CEAS Aeroacoustics Conference and Exhibit, Hilton Head Island, SC, May*, pages 12–14, 2003.

[23] F. Kerhervé and J. Fitzpatrick. Spatio-temporal correlations for turbulent jet flows using the point reference global correlation (prgc) technique. In *Proceedings of the 13th International Symposium on Applications of Laser Techniques to Fluid Mechanics, Lisbon*, 2006.

[24] E. Mollo-Christensen. Jet noise and shear flow instability seen from an experimenter's viewpoint. 1967.

[25] C. E. Tinney, P. Jordan, A. M. Hall, J. Delville, and M. N. Glauser. A time-resolved estimate of the turbulence and sound source mechanisms in a subsonic jet flow. *Journal of Turbulence*, (8):N7, 2007.

[26] C. E. Tinney and P. Jordan. The near pressure field of co-axial subsonic jets. *J. Fluid Mech.*, 611:175–204, 2008.

[27] M. M. Choudhari, D. P. Lockard, M. G. Macag, B. A. Singer, C. L. Streett, G. R. Neubert, R. W. Stoker, J. R. Underbrink, M. E. Berkman, and M. R. Khorrami. Aeroacoustic experiments in the nasa langley low-turbulence pressure tunnel. Technical report, 2002.

[28] E. Manoha, J. Bulté, and B. Caruelle. Lagoon: an experimental database for the validation of CFD/CAA methods for landing gear noise prediction. In *14th AIAA/CEAS aeroacoustics conference (29th AIAA aeroacoustics conference)*, page 2816, 2008.

[29] L. Li, P. Q. Liu, H. Guo, X. Geng, Y. J. Hou, and J. J. Wang. Aerodynamic and aeroacoustic experimental investigation of 30p30n high-lift configuration. *Applied Acoustics*, 132:43–48, 2018.

[30] Z. Ning and H. Hu. An experimental study on the aerodynamics and aeroacoustic characteristics of small propellers. In *54th AIAA Aerospace Sciences Meeting*, page 1785, 2016.

[31] C. F. Wisniewski, A. R. Byerley, W. Heiser, Kenneth W. Van T., T. Liller, and N. Wisniewski. Experimental evaluation of open propeller aerodynamic performance and aero-acoustic behavior. In *33rd AIAA Applied Aerodynamics Conference*, page 2264, 2015.

[32] M. Leyko, F. Nicoud, and T. Poinsot. Comparison of direct and indirect combustion noise mechanisms in a model combustor. *AIAA J.*, 47(11):2709–2716, 2009.

[33] F. E. Culick and P. Kuentzmann. Unsteady motions in combustion chambers for propulsion systems. Technical report, NATO Research and Technology Organization Neuilly-Sur-Seine (France), 2006.

[34] R. L. Raun, M. W. Beckstead, J. C. Finlinson, and K. P. Brooks. A review of Rijke tubes, Rijke burners and related devices. *Prog. Energ. Combust.*, 19: 313–364, 1993.

[35] G. Kirchhoff. On the influence of heat conduction in a gas on sound propagation. *Ann. Phys. Chem*, 134:177–193, 1868.

[36] H. A. Kramers. Vibrations of a gas column. *Physica*, 15(11-12):971–984, 1949.

[37] N. Rott. Damped and thermally driven acoustic oscillations in wide and narrow tubes. *Zeitschrift für angewandte Mathematik und Physik ZAMP*, 20 (2):230–243, 1969.

[38] G. W. Swift. Analysis and performance of a large thermoacoustic engine. *J. Acoust. Soc. Am.*, 92(3):1551–1563, 1992.

[39] G. Y. Yu, X. T. Wang, W. Dai, and E. C. Luo. Study on energy conversion characteristics of a high frequency standing-wave thermoacoustic heat engine. *Applied energy*, 111:1147–1151, 2013.

[40] E. C. Nsofor and A. Ali. Experimental study on the performance of the thermoacoustic refrigerating system. *Applied Thermal Engineering*, 29(13): 2672–2679, 2009.

[41] N. M. Hariharan, P. Sivashanmugam, and S. Kasthurirengan. Experimental investigation of a thermoacoustic refrigerator driven by a standing wave twin thermoacoustic prime mover. *International journal of refrigeration*, 36(8): 2420–2425, 2013.

[42] J. J. Keller. Thermoacoustic oscillations in combustion chambers of gas turbines. *AIAA journal*, 33(12):2280–2287, 1995.

[43] S. M. Sarpotdar, N. Ananthkrishnan, and S. D. Sharma. The rijke tube–a thermo-acoustic device. *Resonance*, 8(1):59–71, 2003.

[44] A. P. Dowling and S. R. Stow. Acoustic analysis of gas turbine combustors. *J. Propul. Power*, 19(5):751–764, 2003.

[45] T. C. Lieuwen and V. Yang. *Combustion instabilities in gas turbine engines: operational experience, fundamental mechanisms, and modeling*. American Institute of Aeronautics and Astronautics, 2005.

[46] R. J. Zhu, D. Pan, C. Z. Ji, T. Zhu, P. P. Lu, and H. Gao. Combustion instability analysis on a partially premixed swirl combustor by thermoacoustic experiments and modeling. *Energy*, 211:118884, 2020.

[47] B. Entezam, W. K. Van Moorhem, and J. Majdalani. Modeling of a Rijke tube pulse combustor using computational fluid dynamics. In *33rd AIAA/ASME/SAE/ASEE Joint Propulsion Conference and Exhibit*. AIAA, 1997. Paper AIAA 97-2718.

[48] C. C. Hantschk and D. Vortmeyer. Numerical simulation of self-excited thermoacoustic instabilities in a Rijke tube. *J. Sound Vib.*, 227:511–522, 1999.

[49] E. Gonzalez. CFD simulations of acoustic and thermoacoustic phenomena in internal flows. In *46th AIAA Fluid Dynamics Conference*, page 3960, 2016.

[50] D. Laera, G. Campa, S. M. Camporeale, E. Bertolotto, S. Rizzo, F. Bonzani, A. Ferrante, and A. Saponaro. Modelling of thermoacoustic combustion instabilities phenomena: Application to an experimental test rig. *Energy Procedia*, 45:1392–1401, 2014.

[51] A. P. Dowling and Y. Mahmoudi. Combustion noise. *Proc. Combust. Inst.*, 35(1):65–100, 2015.

[52] C. Wagner, T. Hüttl, and P. Sagaut. *Large-eddy simulation for acoustics*, volume 20. Cambridge University Press, 2007.

[53] D. B. Hanson. Near-field frequency-domain theory for propeller noise. *AIAA J.*, 23(4):499–504, 1985.

[54] B. Magliozzi, D. B. Hanson, and R. K. Amiet. Propeller and propfan noise. *Aeroacoustics of flight vehicles: theory and practice*, 1:1–64, 1991.

[55] M. Carley. Propeller noise fields. *J. Sound Vib.*, 233(2):255–277, 2000.

[56] S. Oerlemans and J. G. Schepers. Prediction of wind turbine noise and validation against experiment. *Inter. J. Aeroacoustics*, 8(6):555–584, 2009.

[57] A. Tadamasa and M. Zangeneh. Numerical prediction of wind turbine noise. *Renewable energy*, 36(7):1902–1912, 2011.

[58] C. K. W. Tam. Computational aeroacoustics-issues and methods. *AIAA J.*, 33(10):1788–1796, 1995.

[59] C. K. W. Tam and J. C. Webb. Dispersion-relation-preserving finite difference schemes for computational acoustics. *J. Comp. Phys.*, 107(2):262–281, 1993.

[60] B. Elhadidi and A. Hemeda. Efficient domain decomposition technique for solution of high amplitude acoustic wave scattering in nonuniform flows. In *17th AIAA/CEAS Aeroacoustics Conference (32nd AIAA Aeroacoustics Conference)*, page 2840, 2011.

[61] M. Y. Hsi and F. Périé. Computational aeroacoustics for prediction of acoustic scattering. In *NASA Conference Publication*, pages 111–118. NASA, 1997.

[62] C. K. W. Tam. Recent advances in computational aeroacoustics. *Fluid dynamics research*, 38(9):591, 2006.

[63] E. Manoha, C. Herrero, S. B. Khelil, P. Guillen, P. Sagaut, and I. Mary. Numerical prediction of airfoil aerodynamic noise. In *8th AIAA/CEAS Aeroacoustics Conference & Exhibit*, page 2573, 2002.

[64] R. Guenanff, P. Sagaut, E. Manoha, M. Terracol, and R. Lewandowsky. Theoretical aspects of a multidomain high-order method for CAA. In *9th AIAA/CEAS Aeroacoustics Conference and Exhibit*, page 3117, 2003.

[65] G. Desquesnes, M. Terracol, E. Manoha, and P. Sagaut. On the use of a high order overlapping grid method for coupling in CFD/CAA. *J. Comp. Phys.*, 220(1):355–382, 2006.

[66] G. Cunha and S. Redonnet. Towards a robust and accurate CFD/CAA coupling procedure for hybrid methods in aeroacoustics-part 1: On the optimization of CFD/CAA coupled calculations. In *18th AIAA/CEAS Aeroacoustics Conference (33rd AIAA Aeroacoustics Conference)*, page 2063, 2012.

[67] O. Labbe, C. Peyret, G. Rahier, and M. Huet. A CFD/CAA coupling method applied to jet noise prediction. *Computers & Fluids*, 86:1–13, 2013.

[68] S. Redonnet and G. Cunha. An advanced hybrid method for the acoustic prediction. *Advances in Engineering Software*, 88:30–52, 2015.

[69] A. Langenais, F. Vuillot, J. Troyes, and C. Bailly. Numerical investigation of the noise generated by a rocket engine at lift-off conditions using a two-way coupled CFD-CAA method. In *23rd AIAA/CEAS Aeroacoustics Conference*, page 3212, 2017.

[70] A. Langenais, F. Vuillot, C. Peyret, G. Chaineray, and C. Bailly. Assessment of a two-way coupling methodology between a flow and a high-order nonlinear acoustic unstructured solvers. *Flow, Turbulence and Combustion*, 101(3): 681–703, 2018.

[71] F. Q. Hu, M. Y. Hussaini, and P. Rasetarinera. An analysis of the discontinuous Galerkin method for wave propagation problems. *J. Comp. Phys.*

[72] H. K. Versteeg and W. Malalasekera. *An introduction to computational fluid dynamics: The finite volume method*. Longman Group Ltd., 2007.

[73] M. Popescu, W. Shyy, and M. Garbey. Finite volume treatment of dispersion-relation-preserving and optimized prefactored compact schemes for wave propagation. 210(2):705–729, 2005.

[74] F. Q. Hu, M. Y. Hussaini, and J. L. Manthey. Low-dissipation and low-dispersion Runge–Kutta schemes for computational acoustics. *J. Comp. Phys.*, 124(1):177–191, 1996.

[75] J. B. Freund. Proposed inflow/outflow boundary condition for direct computation of aerodynamic sound. *AIAA J.*, 35(4):740–742, 1997.

[76] C. Bogey and C. Bailly. A family of low dispersive and low dissipative explicit schemes for flow and noise computations. *J. Comp. Phys.*, 194(1):194–214, 2004.

[77] C. K. W. Tam, J. C. Webb, and Z. Dong. A study of the short wave components in computational acoustics. *J. Comp. Acoustics*, 1(1):1–130, 1993.

[78] J. Smagorinsky. General circulation experiments with the primitive equations: I. The basic experiment. *Monthly weather review*, 91(3):99–164, 1963.

[79] F. Nicoud and F. Ducros. Subgrid-scale stress modelling based on the square of the velocity gradient tensor. *Flow, turbulence and Combustion*, 62(3): 183–200, 1999.

[80] A. Yoshizawa. Statistical theory for compressible turbulent shear flows, with the application to subgrid modeling. *Phys. Fluids*, 29:2152–2164, 1986.

[81] C. Pierce and P. Moin. Progress-variable approach for large-eddy simulation of non-premixed turbulent combustion. *J. Fluid Mech.*, 504:73–97, 2004.

[82] M. Ihme, M. C. Chong, and H. Pitsch. Prediction of local extinction and re-ignition effects in non-premixed turbulent combustion using a flamelet/progress variable approach. In *Proc. Combust. Inst.*, volume 30, pages 793–800. Combustion Institute, 2005.

[83] O. Gicquel, N. Darabiha, and D. Thévenin. Laminar premixed hydrogen/air counterflow flame simulations using flame prolongation of ILDM with differential diffusion. In *Proc. Combust. Inst.*, volume 28, pages 1901–1908. Combustion Institute, 2000.

[84] B. Fiorina, O. Gicquel, L. Vervisch, S. Carpentier, and N. Darabiha. Premixed turbulent combustion modeling using tabulated detailed chemistry and PDF. *Proc. Combust. Inst.*, 30(1):867–874, 2005.

[85] P. Kryštůfek and K. Kozel. Numerical solution of inviscid compressible steady flows around the RAE 2822 airfoil. In *EPJ Web of Conferences*, volume 92, page 2041. EDP Sciences, 2015.

[86] J. H. Lee, V. Chu, and V. H. Chu. *Turbulent jets and plumes: a Lagrangian approach*, volume 1. Springer Science & Business Media, 2003.

[87] R. Garby, L. Selle, and T. Poinsot. Large-eddy simulation of combustion instabilities in a variable-length combustor. *C. R. Mécanique*, 341:220–229, 2013.

[88] M. E. Harvazinski, C. Huang, V. Sankaran, T. W. Feldman, W. E. Anderson, C. L. Merkle, and D. G. Talley. Coupling between hydrodynamics, acoustics, and heat release in a self-excited unstable combustor. *Phys. Fluids*, 27, 2015. 045102.

[89] S. Taamallah, K. Vogiatzaki, F. Alzahrani, E. Mokheimer, M. A. Habib, and A. Ghoniem. Fuel flexibility, stability and emissions in premixed hydrogen-rich gas turbine combustion: Technology, fundamentals, and numerical simulations. *Appl. Energ.*, 154:1020–1047, 2015.

[90] F. Nicoud and T. Poinsot. Thermoacoustic instabilities: Should the Rayleigh criterion be extended to include entropy changes? *Combust. Flame*, 142:153–159, 2005.

[91] W. Sutherland. The viscosity of gases and molecular force. *Philos. Mag. Series 5*, 36:507–531, 1893.

[92] H. Müller, F. Ferraro, and M. Pfitzner. Implementation of a steady laminar flamelet model for non-premixed combustion in LES and RANS simulations. In *8th International OpenFOAM® Workshop*, pages 1–12. Korean Society for Computational Fluid Engineering, 2013.

[93] V. V. Golubev and H. M. Atassi. Acoustic-vorticity waves in swirling flows. *J. Sound Vib.*, 209:203–222, 1998.

[94] CERFACS. CANTERA user's guide: Propane/air combustion. `https://www.cerfacs.fr/cantera/mechanisms/prop.php`, Last accessed: Jun 20 2021, 2017.

[95] T. D. Thanapal. Personal communication, 2019.

[96] H. Schlichting and K. Gersten. *Boundary-layer theory*. Springer Science & Business Media, 2003.

[97] F. Satta and G. Tanda. Aerodynamic and thermal characteristics of a hot jet in parallel flow. *Journal of Applied Fluid Mechanics*, 9(5), 2016.

[98] A. M. Briones, R. Olding, J. P. Sykes, B. Rankin, K. McDevitt, and J. Heyne. Combustion modeling software development, verification and validation. page V001T01A012, 06 2018.

[99] M. Ihme, L. Shunn, and J. Zhang. Regularization of reaction progress variable for application to flamelet-based combustion models. *J. Comp. Phys.*, 231: 7715–7721, 10 2012.

[100] A. Coclite, L. Cutrone, M. Gurtner, P. De Palma, O. Haidn, and G. Pascazio. Computing supersonic non-premixed turbulent combustion by an SMLD flamelet progress variable model. *International Journal of Hydrogen Energy*, 41, 09 2015.

[101] W. Meier, S. Prucker, M.-H. Cao, and W. Stricker. Characterization of turbulent hytVAir jet diffusion flames by single-pulse spontaneous Raman scattering. *Combust. Sci. Tech.*, 118(4-6):293–312, 1996.

[102] C. McClinton. X-43-scramjet power breaks the hypersonic barrier: Dryden lectureship in research for 2006. In *44th AIAA aerospace sciences meeting and exhibit*, page 1, 2006.

[103] K. Mahesh. The interaction of jets with crossflow. *Annu. Rev. Fluid Mech.*, 45:379–407, 2013.

[104] J. G. Santiago and J. C. Dutton. Velocity measurements of a jet injected into a supersonic crossflow. *J. Propul. Power*, 13(2):264–273, 1997.

[105] M. Gamba, V. A. Miller, and M. G. Mungal. Density ratio and velocity ratio effects on the structure of transverse jets in supersonic crossflow. In *Eighth International Symposium on Turbulence and Shear Flow Phenomena*. Begel House Inc., 2013.

[106] S. Kawai and S. K. Lele. Dynamics and mixing of a sonic jet in a supersonic turbulent crossflow. 12(1):285–298, 2009.

[107] X. C. Chai, P. S. Iyer, and K. Mahesh. Numerical study of high speed jets in crossflow. *J. Fluid Mech.*, 785:152–188, 2015.

[108] M. Gamba, V. A. Miller, and G. Mungal. The reacting transverse jet in supersonic crossflow: physics and properties. In *19th AIAA International Space Planes and Hypersonic Systems and Technologies Conference*, page 3107, 2014.

[109] T. F. Fric and A. Roshko. Vortical structure in the wake of a transverse jet. *J. Fluid Mech.*, 279:1–47, 1994.

[110] R. M. Kelso and A. J. Smits. Horseshoe vortex systems resulting from the interaction between a laminar boundary layer and a transverse jet. *Phys. Fluids*, 7(1):153–158, 1995.

[111] E. F. Hasselbrink and M. G. Mungal. Transverse jets and jet flames. part 1. scaling laws for strong transverse jets. *J. Fluid Mech.*, 443:1–25, 2001.

[112] M. Gamba and M. G. Mungal. Ignition, flame structure and near-wall burning in transverse hydrogen jets in supersonic crossflow. *J. Fluid Mech.*, 780: 226–273, 2015.